Echantillonnage optique à base sur l'interféromètre Mach-Zehnder avec amplificateurs optiques à semi-conducteurs (SOA-MZI) pour applications analogiques

Dimitrios Kastritsis

THÈSE DE DOCTORAT DE

l'ÉCOLE NATIONALE D'INGÉNIEURS DE BREST
COMUE UNIVERSITÉ BRETAGNE LOIRE

ÉCOLE DOCTORALE N° 601
Mathématiques et Sciences et Technologies de l'Information et de la Communication
Spécialité : *Électronique*

préparée en co-tutelle avec

l'UNIVERSITÉ DÉMOCRITE DE THRACE

Par
Dimitrios KASTRITSIS

Optical sampling based on Mach-Zehnder Interferometer with Semiconductor Optical Amplifiers (SOA-MZI) for analog applications

Thèse présentée et soutenue à Brest, le 20/01/2022
Unité de recherche : Lab-STICC, CNRS UMR 6285
Thèse N° : 12

Composition du Jury :

Présidente :	Catherine ALGANI	Professeure des Universités, Conservatoire National des Arts et Métiers (LE CNAM), France
Rapporteur :	Frédéric GRILLOT	Professeur, Télécom - Paris, France
Rapporteur :	Michael CONNELLY	Associate Professor, Université de Limerick, Irlande
Examinateur :	Emmanouil KRIEZIS	Professor, Université Aristote de Thessalonique (AUTH), Grèce
Dir. de thèse :	Ammar SHARAIHA	Professeur des Universités, École Nationale d'Ingénieurs de Brest (ENIB), France
Dir. de thèse :	Kyriakos ZOIROS	Associate Professor, Université Démocrite de Thrace (DUTH), Grèce
Co-encadrant :	Thierry RAMPONE	Maître de Conférences, École Nationale d'Ingénieurs de Brest (ENIB), France
Co-encadrant :	George KYRIACOU	Professor, Université Démocrite de Thrace (DUTH), Grèce

Invité :

Emmanuel MICHAUT	Ingénieur, Directeur adjoint de DETI microwave, Brest, France

This work was conducted with the financial support of Brest Métropole in the frame of ARED ‘Choraal’ project “ÉChantillonnage optique ultra rapide à base d’un SOA-MZI pour applications analogiques large bande”.

ACKNOWLEDGEMENTS

This dissertation is the result of five years of hard and persistent work that could not have been completed without the support of several people.

I would like to thank my supervisor, Ammar SHARAIHA, Professor at ENIB, for guiding me throughout this work. His valuable advice and his deep scientific expertise contributed to a great amount in this work. His unlimited enthusiasm and fascination for research as well as his openness was a constant source of motivation during difficult times.

I wish to show my appreciation to my supervisor Kyriakos ZOIROS, Associate Professor at Democritus University of Thrace (DUTH). He has constantly guided and supported me since he was my diploma thesis supervisor and it is thanks to him that I considered pursuing this thesis. I'm grateful for his supervision and the valuable scientific assistance he provided all these years.

I would like to thank Thierry RAMPONE, Associate Professor at ENIB, for sharing with me his paramount technical expertise and for his guidance during laboratory experiments. His attention to detail and his productive scepticism are undoubtedly essential in the complicated project of a thesis.

Special thanks to George KYRIACOU, Professor at DUTH, for participating in the Greek PhD advisory committee. Moreover, I thank him for his tutoring in two post-graduate courses that I attended and his tireless zeal in communicating knowledge.

I sincerely thank Frederic GRILLOT, Professor at Telecom-Paris, and Michael CONNELLY, Associate Professor at University of Limerick, who accepted to be the reviewers of the thesis. I also express my sincere gratitude to Catherine ALGANI, Professor at Conservatoire National des Arts et Métiers - Paris (CNAM-Paris) and Emmanouil KRIEZIS, Professor at Aristotle University of Thessaloniki (AUTH), for accepting to be the examiners of this work.

I would like to thank my research mates Noor HAMDASH, Jacqueline SIME, Abdelouahid BENTAMOU, Ramez HAMIE for creating a fun work environment and for their willing help and advice.

I wish to expand my special thanks to the entire ENIB team: the professors, the technicians, and the administration, especially Viviane LARDEUR and Jean-Luc BERTHEVAS, for their help during the five years of the thesis.

I would like to thank my late mother Marina, my father Theofilos and my brother Aristidis, for their love, understanding, encouragement and full support throughout the years of my studies.

Last but not least, I wish to thank my beloved partner Maria for her trust, understanding, care and support, without which it would not be possible to complete this thesis.

Abstract

This thesis aims at investigating and showing the feasibility of using the SOA-MZI module as a photonic sampler in place of other technological solutions of electro-optic nature (EOM, MZM, etc.) which have been adopted so far. In this manner, we obtain the additional benefit of rendering the photonic sampler an all-optical as opposed to electro-optic, module. The SOA-MZI photonic sampler can eventually be incorporated as a building module in more advanced systems such as in photonic Analog to Digital Converters (ADCs) to perform the process of sampling or in a complete Radio over Fiber (RoF) application as a frequency mixer. In the aforementioned applications, the proposed module enjoys the benefit of low temporal jitter, high flexibility and adaptability while it facilitates the transformation of the corresponding electro-optic systems to all-optical ones.

Two architectures are possible with the SOA-MZI photonic sampler, the Switching and Modulation architectures. Modulation architecture is novel and is presented for the first time during this thesis work. Employing the Modulation architecture, a post-distortion linearization method is formulated theoretically and validated experimentally by applying it to sinusoidal signals at frequencies between 0.25 GHz and 2 GHz with modulation indices (MI) between 20% and 80%, which are sampled at a 10 giga samples per second (GSa/s) rate. The potential improvement by the use of the linearization technique in terms of Total Harmonic Distortion (THD) is estimated at 19.6 dB. Experimentally, this improvement is verified for a sinusoidal signal to be sampled at 250 MHz with MI equal to 80% while significant improvement in terms of THD is observed for sinusoidal signals to be sampled up to 2 GHz. Specifically, for the highest frequencies measured, a THD improvement equal to 10 dB and equal to 7 dB is reached for a sinusoidal signal to be sampled with MI equal to 60 % at 1 GHz and 2 GHz, respectively.

The SOA-MZI photonic sampler employed as a photonic up-converter is theoretically examined by developing a small-signal analysis model, and experimentally evaluated and validated using Switching and Modulation architectures in terms of Conversion Gain (CG). An expression in closed-form is derived for the CG, which provides qualitative insight into this metric of the two architectures. Using this closed-form expression, the performance in terms of CG for a known set of parameters can be predicted, or the scheme's critical parameters can be selected in order to optimize the up-converter's performance. A CG equal to 16 dB is achieved for the 1 GHz to 9 GHz conversion when employing the Switching architecture, whereas a CG equal to 9 dB for the 1 GHz to 39 GHz conversion when employing the Modulation architecture. A sufficiently low Error Vector Magnitude (EVM) for Quadrature Phase-Shift Keying (QPSK)

and Quadrature Amplitude Modulation of 16 states (16-QAM) is obtained when employing the Modulation architecture, which allows to support a data bit rate equal to 1 Gbps and 512 Mbps for QPSK and 16-QAM, respectively.

The most important outcome is that the SOA-MZI photonic sampler is a viable technological alternative to the most main electro-optic modules employed into the photonic ADC systems and for the photonic mixing operations in RoF systems. Especially, the Modulation architecture is more efficient than the Switching architecture and not just complementary, as it supports very high sampling frequencies up to 100 GHz or even higher.

Keywords: Optical Sampling, Ultrashort Pulses, Semiconductor Optical Amplifier (SOA), Mach-Zehnder Interferometer (MZI), SOA-MZI, All-optical Mixer, Frequency Conversion, Switching Architecture, Modulation Architecture, Radio over Fiber (RoF), Photonic Analog to Digital Converter (PADC), MicroWave Photonics (MWP), Post-Distortion Linearization Technique.

Table of Contents

List of acronyms

ADC	Analog to Digital Converter
AMP	Electrical Amplifier
APE	Absolute Error in Percentage
ARoF	Analog Radio over Fiber
ASE	Amplified Spontaneous Emission
Att	Optical Attenuator
AWG	Arbitrary Waveform Generator
BER	Bit Error Ratio
BW	BandWidth
CC	Contitioning Circuit
CG	Conversion Gain
CWDM	Coarse Wavelength Division Multiplexing
CW	Continuous Wave
DCA	Digital Communication Analyzer
DCF	Dispersion Compensating Fiber
DSB-FC	Double Sideband Full Carrier
DSO	Digital Sampling Oscilloscope
DSP	Digital Signal Processor
DWDM	Dense Wavelength Division Multiplexing
EAM	Electro-Absorption Modulator
EMI	Electromagnetic Interference
ENOB	Effective Number of Bits
EOM	Electro-Optic Modulator
ER	Extinction Ratio
ESA	Electical Spectrum Analyzer
EVM	Error Vector Magnitude
E/O	Electro-Optic conversion
FEC	Forward Error Correction
FFT	Fast Fourier Transformation
FIR	Finite Impulse Response
FWHM	Full Width at Half Maximum
FWM	Four Wave Mixing

HD	Harmonic Distortion
HNL-DSF	Highly Nonlinear Dispersion Shifted Fibers
IoT	Internet of Things
LD	Laser Diode
LSB	Least Significant Bit
MI	Modulation Index
MLL	Mode-Locked Laser
MWP	Microwave Photonics
MZM	Mach-Zehnder Modulator
NF	Noise Figure
OBPF	Optical Band-Pass Filter
OMP	Optical Modulation Power
OPC	Optical Pulse Clock
OSA	Optical Spectrum Analyzer
O/E	Opto-Electronic conversion
PC	Polarization Controller
PDG	Polarization Dependant saturated Gain
PM	Optical Power meter
PM-EDFA	Polarization Maintaining-Erbium Doped Fiber Amplifier
PM-to-AM	Phase to Amplitude Modulation
PZT	Piezoelectric Transducer
HFC	Higher Frequency components
QAM	Quadrature Amplitude Modulation
QPSK	Quadrature Phase-Shift Keying
RF	Radio Frequency
RF1, RF2	Radio Frequency generator
RMS	Root Mean Squared
RoF	Radio over Fiber
RRC	Root Raised Cosine
SD	Second Derivative
SNR	Signal to Noise Ratio
SOA	Semiconductor Optical Amplifier
SOA-MZI	Semiconductor Optical Amplifier - Mach-Zehnder Interferometer
SR	Symbol Rate
THD	Total Harmonic Distortion
TS	Time Stretching
TWA	Travelling-Wave Amplifier
UTC-PD	UniTravelling Carrier PhotoDiodes

VNA	Vector Network Analyzer
VSA	Vector Signal Analyzer
XAM	Cross-Absorption Modulation
XGM	Cross Gain Modulation
XPM	Cross Phase Modulation

List of Figures

List of Tables

Chapter 1

Introduction

1.1 Research Context

Over the last decades, the research area of microwave photonics (MWP) has attracted great interest and has substantially evolved. MWP is defined as the interdisciplinary field that combines opto-electronic devices, modules and systems with microwave technology. Due to its dual nature, MWP permits certain functionalities to be performed either in the electrical or in the optical domain. The choice between the two domains depends on the assessment of the advantages and the constraints of the specific electronic or optical module available for this purpose. The motivation to utilize optical modules into microwave systems, replacing the corresponding electronic ones, is that the optical modules can take directly advantage of the large bandwidth, low losses and high immunity to electromagnetic interference (EMI) of optical fibers. In the past few years, there has been an increasing effort in researching new MWP techniques for different applications. In general, the topics covered by MWP include photonic generation of microwave and millimeter-wave signals, up and down frequency mixing, optically controlled phased array antennas, radio-over-fiber systems, and photonic analog to digital conversion (ADC) devices [1–13]. MWP can be used for applications such as broadband wireless access networks, sensor networks, satellite communications, instrumentation, 5G, radar, Internet of Things (IoT) and electronic warfare [14–22].

A basic block diagram of an MWP system is depicted in Figure 1.1. A Radio Frequency (RF) input signal, which is conditioned properly by an electrical drive circuit, is converted to the optical domain by an Electro-Optic Modulator (EOM). The signal is then transmitted through an optical fiber and subsequently processed by photonic devices. The processed signal is again transmitted through an optical fiber and then converted back to the electrical domain and processed by a photo-receiver. The RF Output signal is received after proper electrical processing by an RF circuit. Either the RF input or the RF output or both could be received or transmitted by an antenna, which is the case in RoF systems.

In this framework, in order to expand the potentiality and flexibility of such an MWP system, the development of a subsystem in the optical layer to perform the function of sampling is crucial.

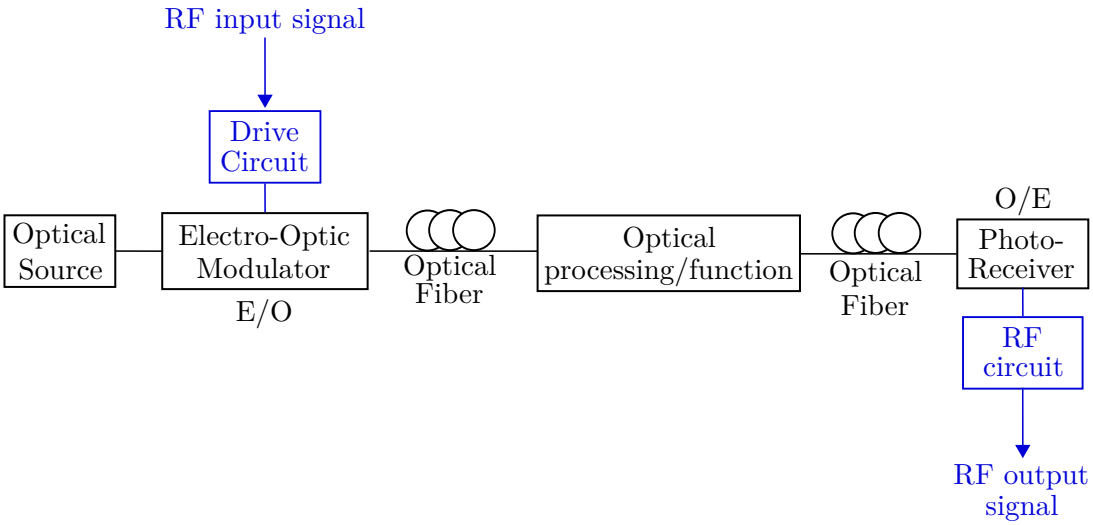

Figure 1.1: Basic scheme of a microwave photonics (MWP) system. RF electrical wiring and the outline of electrical devices are in blue color, whereas the fiber connections and the outline of photonic devices and modules are in black color. Also, the outlines of the Electro-Optic Modulator, which converts the signal from the electrical to optical layer (E/O), and of the Photo-receiver, which performs the inverse (O/E), are in black color.

1.1.1 Optical Sampling

Optical sampling refers to a class of techniques where optical signals, usually in the form of ultra-short pulses, are used to sample electrical or optical signals.

Initially, the sampling process was realized in the electrical domain, which impeded the exploitation of its full potential due to the limited electronic bandwidth and the timing jitter of electronic oscillators [7, 10]. Lately, however, sampling in the optical domain has become an attractive technological alternative owing to its ability to combine the advantages of optical fiber links with the possibility of using a low jitter Mode-Locked Laser (MLL) [23, 24] as the sampling signal [10, 25, 26]. The sampling function is fundamental and it is used in a wide number of applications.

Some typical applications of optical sampling are:

- ADCs with sampling rates of tens of gigahertz; applications in wide-band radars, optical fiber communications, and ultra-fast oscilloscopes
- Characterizing trains of ultra-short pulses at extremely high pulse repetition rates, which occur e.g. in time-multiplexed optical fiber communications systems
- Generating microwave or millimeter wave signals

1.1.1.1 Photonics in ADC architectures

The use of photonic technology in ADC architectures can be divided in 4 categories:

- Photonics-assisted ADCs, an electronic ADC that is responsible for both the sampling and quantization functions and photonic components are employed to boost its capabilities
- Photonic sampling with electronic quantization
- Electronic sampling with photonic quantization
- Photonic sampling and quantization

From the above categories, the most developed one is photonic sampling with electronic quantization, and it is the one that will be explained in detail, in the following.

A basic photonic link, using a simple design for optically sampled and electronically quantized ADCs, is shown in Figure 1.2. In this, an MLL playing the role of an optical clock provides a stream of ultra-short optical pulses of high temporal stability. This stream, which acts as the sampling signal, enters into the optical port of the EOM which in most cases is a Mach-Zehnder Modulator (MZM) at the same time as the RF signal to be sampled is applied to the RF port of the EOM. The EOM is the device which performs the optical sampling. Finally, the sampled signal at the EOM output is converted from the optical domain to the electrical domain by the use of a high-speed photodiode and then digitized by the electronic ADC. The main advantage of

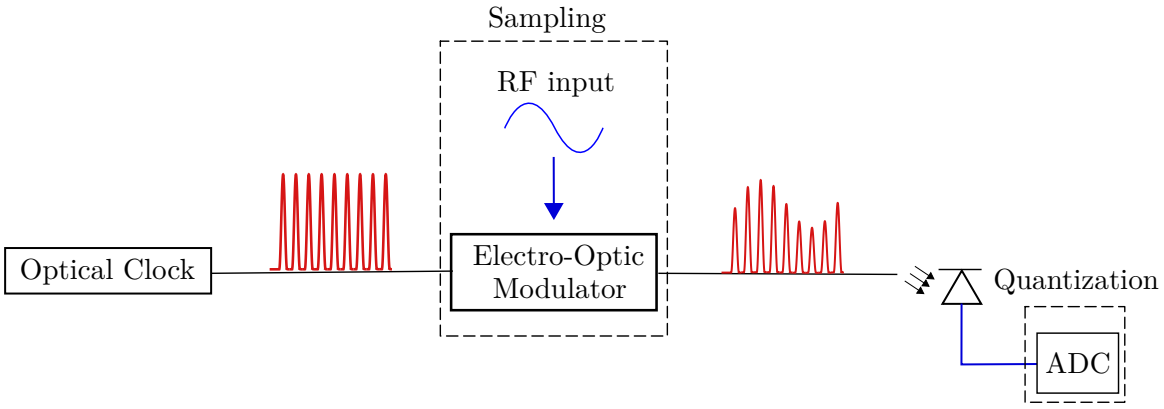

Figure 1.2: Basic photonic link of optically sampled and electrically quantized ADCs. Reproduced from [27].

photonic sampling system with electronic quantization, such as the one in Figure 1.2 is that the temporal jitter is controlled by the ultra stable optical clock and is significantly lower than the temporal jitter of electronic clocks. However, the main inconvenience of such a system is that the rate at which the unique electronic ADC and subsequently the incorporated quantizer operates

is equal to the sampling rate. In case of broadband communications, the sampling rate must be high enough to prevent aliasing, meaning that the system in Figure 1.2 requires a high speed and consequently a high cost electronic ADC. This inconvenience can be overcome by substituting the unique high-speed ADC with multiple lower-speed ADCs in two possible architectures, namely time division demultiplexing and time-to-wavelength mapping. Both architectures are presented in the following.

A simple design for optically sampled and electronically quantized ADCs is presented in Figure 1.3. An MLL, playing the role of an optical clock, provides a stable stream of ultra-short optical pulses. This stream, which acts as the sampling signal, arrives into the optical port of the EOM while the RF signal to be sampled is applied to the RF port of the EOM. Essentially, the EOM is the device which performs the optical sampling. The sampled optical signal is time-demultiplexed by an optical switch in n channels (8 in the figure), converted to the electronic domain by photodetectors. Subsequently, the electric signal is conditioned properly either by the use of an appropriate low-pass filter or of an integrate-and-reset circuit [28], and finally, it is digitized by the electronic ADCs and assembled by the processing unit that follows. This implementation, utilizing multiple channels, reduces the bandwidth requirements for photodetectors and the sampling rate requirements for individual electronic ADCs [27]. Additionally, because of the reduced bandwidth at the input of electronic ADCs, the comparator ambiguity is significantly reduced [10]. However, it should be noted that the time division demultiplexing architecture is demanding in terms of the synchronization between the parallel channels and except for the multiple ADCs, there is also the need for multiple photodiodes, an optical switch and some processing at the last stage in order to convert the parallel quantization channels to a serial digital output. The time-demultiplexed architecture with 8 channels has been implemented in [29], sampling a 733 MHz signal at 505 MSa/s with 9.8 ENOB.

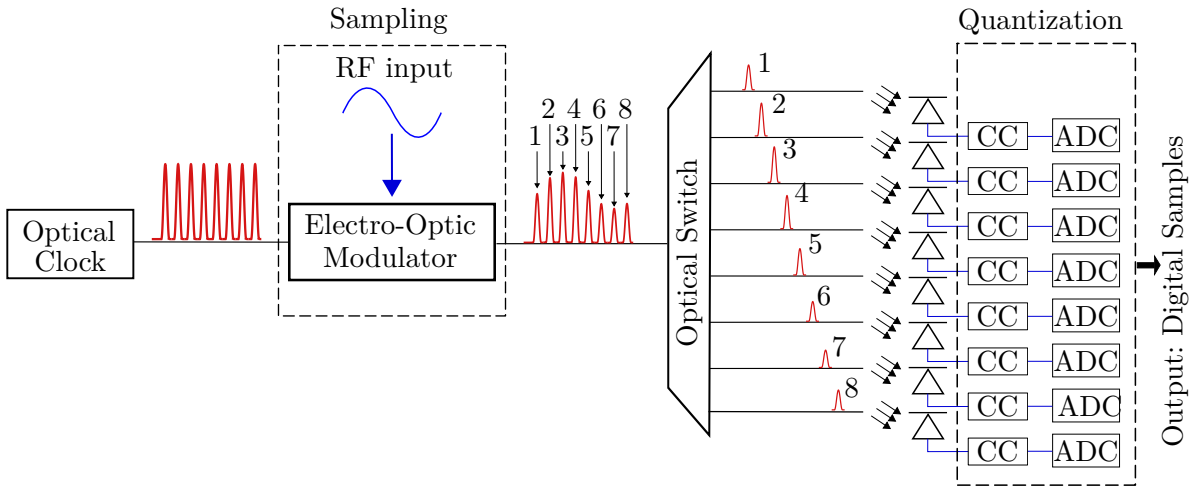

Figure 1.3: Layout for Optically Sampled Analog to Digital Converters using time-demultiplexing. CC: Conditioning circuit. Reproduced from [27].

There are also many variants of this architecture which manage to achieve high performance. One of these alternative architectures is the wavelength-demultiplexing based on discrete time-to-wavelength mapping. This architecture is presented in Figure 1.4.

In this architecture, the MLL, which has a repetition period T_{ck}, is followed by a wavelength demultiplexer, which splits the multi-wavelength MLL signal into 4 channels. Each of these channels is delayed by a different amount of time, ensuring that at the output of the wavelength multiplexer (MUX) that follows, a pulse-train of four periodically repeated wavelengths with a repetition period $T_{ck}/4$ is formed. The amplitude of the pulse train is modulated by the input RF signal with the use of a Mach-Zehnder Modulator (MZM). This operation creates a time-to-wavelength mapping within the pulse train, meaning that neighboring pulses at the optical input of the MZM differ in wavelength [30], as shown in Figure 1.4. Wavelength demultiplexers as the one after the MLL, split each one of the two complementary outputs of MZM to 4 channels. Finally, photodetectors in each channel are used for the conversion to the electronic domain, and ADCs are employed for the quantization and the digitization of the input RF signal. The gain and offset mismatch between the different channels can be addressed by appropriate calibration and compensation algorithms which are successfully applied in modern electronic multichannel ADCs as well. The architecture of wavelength demultiplexing ADCs based on time-to-wavelength mapping was proposed in [30] and [31], and was successfully implemented in [10] sampling a 41 GHz signal at 2.1 GSa/s achieving 7 ENOB. Another interesting modification of the time-to-wavelength mapping scheme is time-stretching (TS) and it is used for the implementation of ADCs, as well as for the study of very high frequency phenomena, such as semiconductor charge carrier dynamics. This configuration (TS-ADCs) was implemented in [32], achieving 5.17 ENOB

for a 26 GHz signal and bandwidth over 9.6 GHz. The combined use of multiple channels and multi-stretching, can be used to achieve exceptionally high sampling rates. Such a configuration with 50 channels is employed in [33] to achieve 1 TSa/s sampling rate. The ENOB for this study was 3.5 for a 48 GHz RF signal, and the bandwidth was over 10 GHz. Also, a spectacular sampling rate of 10 TSa/s has been reached with the same technique (distributed Raman optical amplification is realized inside the dispersive element that performs the time stretch), sampling a 95.3 GHz signal with 4.5 ENOB and bandwidth over 50 GHz [34].

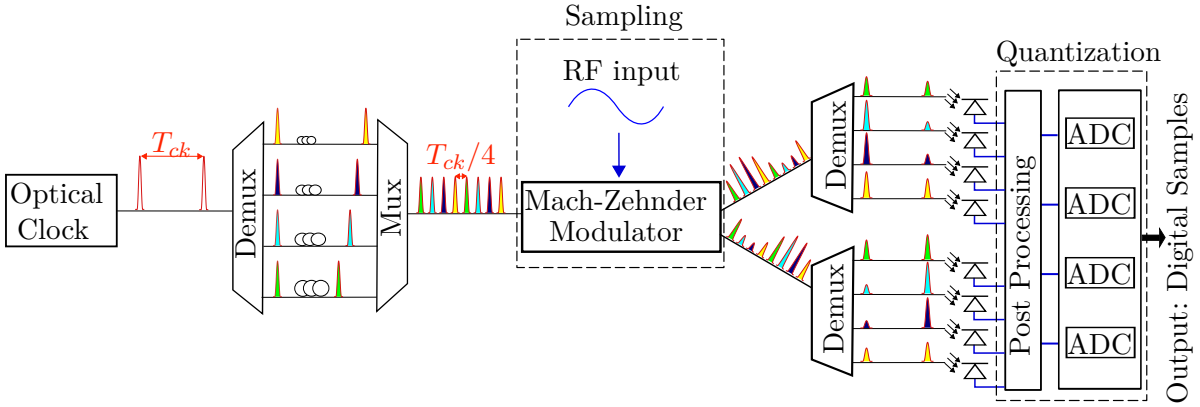

Figure 1.4: Layout of the photonic ADC based on discrete time-to-wavelength mapping. Reproduced from [10].

1.1.1.2 Photonic Mixers

Photonic microwave mixers have been proposed and implemented as a substitute of electronic microwave mixers due to two significant advantages: their relative simplicity and the ease of distribution of the microwave signal through the optical fiber without the need of unnecessary conversions from the electrical to the optical domain, and vice-versa [9].

Many devices exploiting various non-linear electro-optic and optical phenomena has been used as photonic mixers. The fused silica in a Highly Nonlinear Dispersion Shifted Fibers (HNL-DSF) can be used for optical mixing exploiting either Cross-Phase Modulation (XPM) or Four-Wave Mixing (FWM) [35]. The main restriction of HNL is the need of a large fiber length and a high power. High performance Mach-Zehnder modulators (MZM) with Lithium-Niobate material ($LiNbO_3$) that exploit Pockels electro-optic effect have been extensively used for the purpose of frequency conversion [35]. Another possibility is the Electro-Absorption Modulator (EAM) utilizing Cross-Absorption Modulation (XAM) in a semiconductor material [36, 37]. Finally, photodiodes and lately UniTravelling Carrier PhotoDiodes (UTC-PD) have also been employed by exploiting the nonlinear current response when the incident power is high enough and the reverse bias of photodiode is low enough [38]. Originally, Semiconductor Optical Amplifiers (SOA)

Table 1.1: Comparison of Frequency Conversion Techniques

Device/Effect	**Advantages**	**Disadvantages**
Fiber based	Very simple configuration	Large fiber length, high pump power
UTC-PD	Simple configuration	Low CG
EAM/XAM	Simple configuration, large bandwidth	Low CG, high pump power
MZM	Simple configuration	Low CG, polarization sensitive
SOA/XGM	Simple configuration	Low ER, high distortion
SOA/FWM	Large conversion bandwidth	Low CG, polarization dependant
SOA/XPM	Low pump power, high ER	Requires PM-to-AM conversion

exploiting the nonlinear phenomena of XGM (Cross-Gain Modulation) have been proposed and investigated in [39], presenting a photonic mixer for down-conversion and up-conversion of a 6 GHz signal to 1 GHz and 11 GHz, achieving a Conversion Gain (CG) up to 6 dB for down-conversion and up to 2 dB for up-conversion. Another group of researchers in [40], succeeded in up-converting a 1 GHz signal to 24 GHz and 26 GHz. CG was 10 dB and there was a negligible phase noise degradation in the process. A comprehensive study of frequency mixing employing an SOA has been conducted in [41]. In this work, a small-signal theoretical analysis and an experimental performance analysis of the device were presented. The implemented mixer managed to obtain 11.5 dB and 11 dB for down-conversion (from 1 GHz to 0.1 GHz) and up-conversion (from 1 GHz to 1.9 GHz), respectively.

SOAs exploiting XPM [42–46] can be used for mixing embedded in an interferometric arrangement, such as the Mach-Zehnder Interferometer (SOA-MZI). SOA and SOA-MZI exhibit all the advantages mentioned in the previous paragraph while being an all-optical solution. In addition, because they both are active modules, they also provide a CG as opposed to the conversion loss suffered by the previously reported passive photonic mixers. The main disadvantage of XGM-based mixing techniques is the limited Extinction Ratio (ER) of the converted signal. By comparison, a SOA-MZI provides large ER while lowering the required optical input power due to its interferometric structure [44, 45]. A comprehensive comparative analysis of alternative up-conversion configurations employed in RoF systems is made in [35]. The most crucial advantages and disadvantages of the presented conversion techniques are listed in Table 1.1. All-optical mixing using a SOA-MZI has been experimentally achieved in [42], where frequency up-conversion from 2.5 GHz to 32.5 GHz was demonstrated with a high CG of 6 dB. Lately, SOA-MZI-based frequency mixer was successfully used to generate a 100 GHz signal through up-conversion of 1 GHz signal [47]. A SOA-MZI combined with an MLL's pulse train of repetition frequency f_{ck}, instead of a two-tone signal produced either by an EOM, as in [42], or an MZM, as in [44], provides increased flexibility as it can be used to up- or down-convert a signal

at f_{dat} , to multiple target frequencies at $|if_{ck} \pm f_{dat}|$, $n \in \mathbb{N}$, simultaneously [45, 46]. A possible integration of such a photonic sampler mixer in a basic RoF system is illustrated in Figure 1.5.

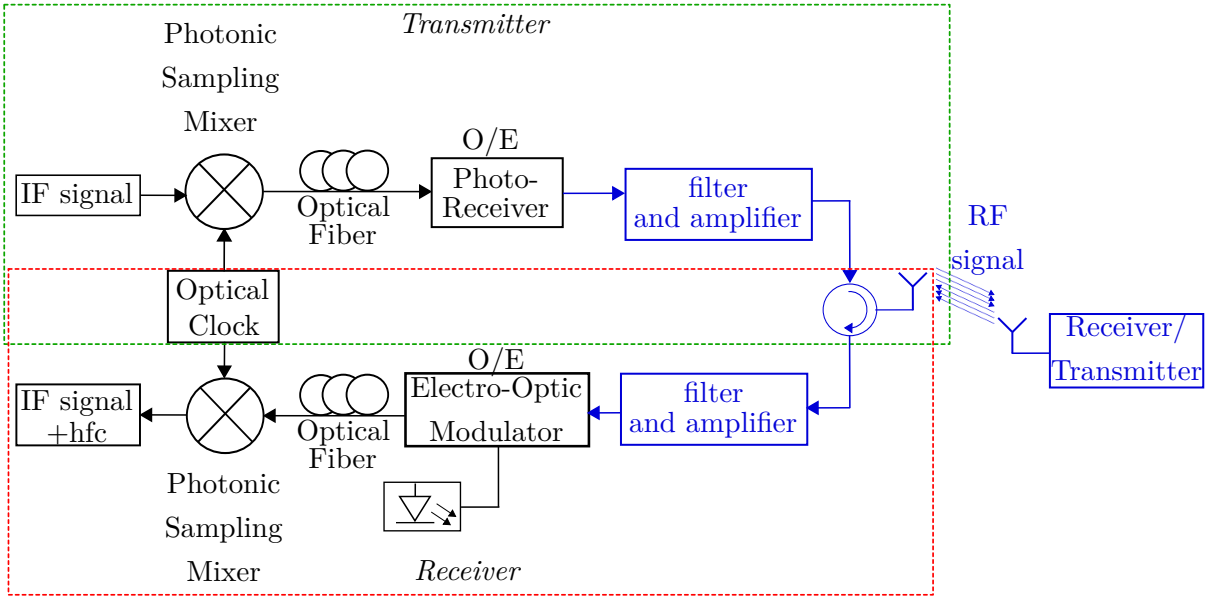

Figure 1.5: Integration of the photonic sampling mixer into a radio over fiber (RoF) system. RF electrical wiring and the outline of electrical devices are in blue color, whereas the fiber connections, the outline of photonic devices and modules, as well as the Photo-receiver which performs the conversion from the optical to the electric domain (O/E) are in black color. Hfc: Higher frequency components.

In the transmitter, the IF optical signal is up-converted by the Photonic Sampling Mixer, exploiting the property of sampling, from f_{dat} to $if_{ck} \pm f_{dat}$, as shown in Figure 1.6. The Photonic Sampling Mixer's output is transmitted by the optical fiber to the Photonic Receiver where it is converted to the electrical domain. Then the resultant electrical signal is filtered and amplified in order to retain only the frequency content of the desired target RF frequency. Finally, the up-converted signal is emitted by the antenna to the remote receivers/transmitters. In the receiver, the incoming RF electrical signal is received by the antenna, subsequently filtered, amplified and converted to the electrical domain by an EOM. Then, the optical RF signal is transmitted to the Photonic Sampling Mixer by an optical fiber where it is down-converted from f_{dat} to $f_{dat} - if_{ck}$, as shown in Figure 1.7. A key benefit of a Photonic Sampling Mixer other than the ones that stem from the direct compatibility with optical fiber is that compared to an Electronic Mixer, the Photonic Sampling Mixer permits to avoid the electrical up-conversions and down-conversions with noisy high frequency RF oscillators by employing an ultra-stable optical clock

[7, 26]. However, it should be noted that in the case where either the input sampling signal or the output sampled signal has to be transmitted over a long distance through an optical fiber, the problem of fiber chromatic distortion must be addressed. One possible solution to compensate for the chromatic dispersion and overcome the associated problem is through using a Dispersion Compensating Fiber (DCF) of appropriate length just before the electro-optic conversion stage.

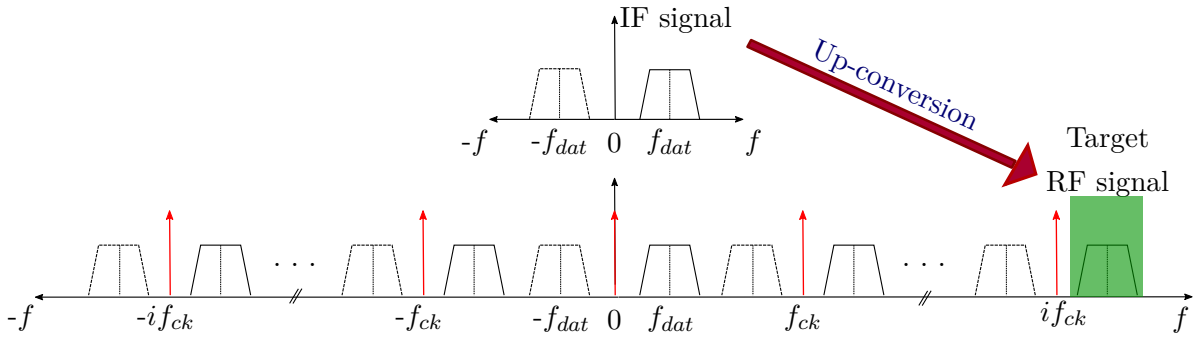

Figure 1.6: Conceptual diagram of sampling for the purpose of up-conversion.

In addition, it is worth noting that this system could be applicable to Coarse Wavelength Division Multiplexing (CWDM) and Dense Wavelength Division Multiplexing (DWDM) systems, provided that $if_{ck} \pm f_{dat}$ is smaller than the channel bandwidth also known as channel spacing of the utilized grid.

At the first such study [46], the repetition rate of MLL was $f_{ck} = 7.8$ GHz and the intermediate frequency was $f_{dat} = 1$ GHz. The SOA-MZI bandwidth was 7.3 GHz and the ER equal to 19.2 dB for the selected operating point. The data signal was up-converted from $f_{dat} = 1$ GHz to $if_{ck} \pm f_{dat}$, with $i = 1, 2, 3, 4, 5$. As the frequency of up-converted signal increased, the CG was diminishing from 14.4 dB for the first up-conversion frequency to -20 dB for the fifth up-conversion frequency.

At the second study [45], a different optical pulse source was used with shorter pulses and the same technique was employed for both up- and down-conversion. The repetition rate was f_{ck} = 7.8 GHz, and the frequency of the sampled to be up-converted was 0.5 GHz for up-conversion and 39.5 GHz for down-conversion. The SOA-MZI bandwidth was 6.5 GHz and the ER was 23 dB for the selected operating point. The up-conversions were performed from $f_{dat} = 0.5$ GHz to $if_{ck} \pm f_{dat}$, and the down-conversions from $f_{dat} = 39.5$ GHz to $f_{dat} - if_{ck}$, with i = 1, 2, 3, 4, 5. CG for down-conversion was diminishing as the frequency increased from 20.4 dB for the first up-conversion frequency to 0 dB for the fifth up-conversion frequency. For up-conversion,

the CG was similarly reduced from 15.5 dB to -13.4 dB.

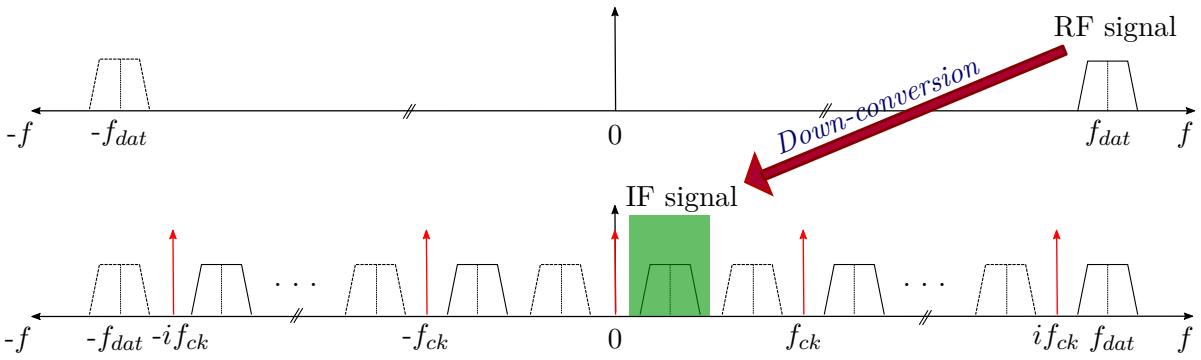

Figure 1.7: Conceptual diagram of sampling for the purpose of down-conversion.

Plenty of functions have been developed in the last few years in MWP using SOAs and SOA-MZIs. These multi-functional devices and modules present a large wavelength operating range and a high nonlinear behavior. Moreover they have the advantage of small size and that they can be integrated either monolithically or hybridically with other RF components [48, 49].

1.2 Thesis Contribution

The dissertation's subject is focused on the SOA-MZI, an all-optical interferometric module, used for the purpose of photonic sampling (Figure 1.8). This thesis aims at investigating and showing the viability of the SOA-MZI module as a photonic sampler in place of the EOM and MZM which are the most frequent choices, as previously discussed. In this manner, the additional benefit of rendering the photonic sampler an all-optical module as opposed to an electro-optical module is attained, thus circumventing the need for additional slow and high cost electro-optic conversions.

The optical sampling clock utilized for this realisation is produced by an active MLL laser. Two architectures are possible with the SOA-MZI photonic sampler, Switching and Modulation architectures. The former architecture is well-established for the SOA-MZI module whereas the latter is novel and is presented for the first time during this thesis work to the best of our knowledge. Also, in this thesis unlike most of the related research, experimental results of sampling in the time domain are extensively shown and analyzed. Furthermore, a post-distortion linearization method is formulated theoretically and applied experimentally in the case of SOA-MZI photonic sampler for the first time to the best of our knowledge.

The SOA-MZI photonic sampler can eventually be incorporated as a module in more complex systems. The SOA-MZI photonic sampler can be utilized to perform the process of sampling in a photonic ADC scheme with either time-division as the one shown in Figure 1.3 or with time-to-wavelength mapping as the one shown in Figure 1.4. Furthermore, the SOA-MZI photonic sampler can be utilized as a frequency up- and down-converter from one frequency to multiple frequencies in a complete RoF application alike to the one of Figure 1.5. In the aforementioned applications, the proposed system enjoys the benefit of low temporal jitter, presented in detail in 2.1.2.1, while converting the corresponding electro-optical systems to all-optical ones.

The proposed study has several objectives, detailed in the following chapters, however the main ones are:

- Performance evaluation of the sampling process of SOA-MZI photonic sampler, followed by a post-distortion linearization technique in order to optimize its operation.
- Performance evaluation of different architectures based on the SOA-MZI photonic sampler on the application of up-conversion at theoretical and experimental level.

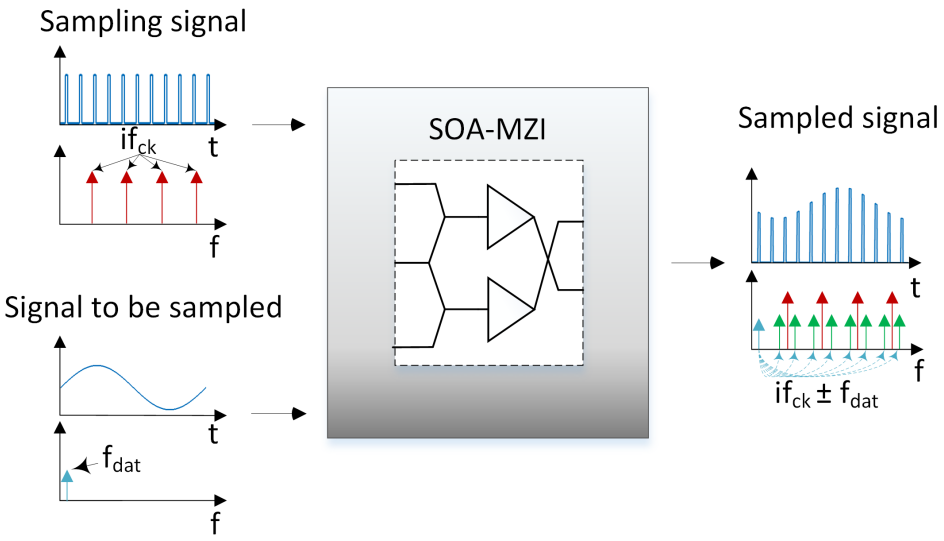

Figure 1.8: Schematic diagram of the SOA-MZI photonic sampler

1.3 Thesis Organization

In chapter 2, the theory of optical sampling, i.e. the notions of sampling in general and optical sampling in particular are discussed, as well as the fundamentals of the SOA-MZI module are presented, i.e. the SOA and SOA-MZI model is formulated, the SOA-MZI principle of operation

is demonstrated and finally, its most important characteristics are provided theoretically and experimentally. In chapter 3, the SOA-MZI sampling process is demonstrated, employing two possible architectures of the SOA-MZI photonic sampler, the Switching and the Modulation architectures. The Switching and Modulation architectures are presented, and their advantages and disadvantages are cited. Moreover, experimental results of sampling using the Modulation architecture are presented in the time and frequency domains. Furthermore, a post-distortion linearization technique is formulated theoretically and applied experimentally to improve the performance of the sampler. In chapter 4, the Modulation and Switching architectures of the SOA-MZI sampler are evaluated and compared for the application of frequency conversion at theoretical and experimental level. Finally, in the Conclusion, the main outcomes of the dissertation are summarised and suggestions for future research work are concisely given.

References

[1] A. Seeds, "Microwave photonics," *IEEE Transactions on Microwave Theory and Techniques*, vol. 50, no. 3, pp. 877–887, Mar. 2002.

[2] A. Vilcot, B. Cabon, and J. Chazelas, Eds., *Microwave Photonics: From Components to Applications and Systems*. Boston, MA: Springer US, 2003.

[3] J. Capmany and D. Novak, "Microwave photonics combines two worlds," *Nature Photonics*, vol. 1, no. 6, pp. 319–330, Jun. 2007.

[4] N. Hamdash, A. Sharaiha, T. Rampone, P. Morel, D. Le Berre, N. Martin, and C. Quendo, "Experimental and Small-signal Analysis of Microwave Photonic Phase Shifter based on Slow and Fast Light using Linear and Nonlinear Semiconductor Optical Amplifiers," in *Proc. IEEE 2018 International Topical Meeting on Microwave Photonics (MWP)*, Oct. 2018, pp. 1–4.

[5] N. Hamdash, A. Sharaiha, T. Rampone, C. Quendo, N. Martin, and D. Le Berre, "Optically Controlled RF Phase Shifts in SOAs by Adding the XGM Response of an Optical Signal," *IEEE Photonics Technology Letters*, vol. 31, no. 13, pp. 1060–1063, Jul. 2019.

[6] N. Hamdash, A. Sharaiha, T. Rampone, D. L. Berre, N. Martin, and C. Quendo, "Small-Signal Analysis in Two Calculation Sections and Experimental Validation of Up-Converted Coherent Population Oscillations in Semiconductor Optical Amplifiers," *IEEE Photonics Journal*, vol. 13, no. 4, pp. 1–10, Aug. 2021.

[7] G. C. Valley, "Photonic analog-to-digital converters," *Optics Express*, vol. 15, no. 5, pp. 1955–1982, Mar. 2007.

[8] S. Iezekiel, "Microwave Photonics – an Introductory Overview," in *Microwave Photonics*. John Wiley & Sons, Ltd, 2009, pp. 1–37.

[9] J. Yao, "Microwave Photonics," *Journal of Lightwave Technology*, vol. 27, no. 3, pp. 314–335, Feb. 2009.

[10] A. Khilo, S. J. Spector, M. E. Grein, A. H. Nejadmalayeri, C. W. Holzwarth, M. Y. Sander, M. S. Dahlem, M. Y. Peng, M. W. Geis, N. A. DiLello, J. U. Yoon, A. Motamedi, J. S. Orcutt, J. P. Wang, C. M. Sorace-Agaskar, M. A. Popović, J. Sun, G.-R. Zhou, H. Byun,

J. Chen, J. L. Hoyt, H. I. Smith, R. J. Ram, M. Perrott, T. M. Lyszczarz, E. P. Ippen, and F. X. Kärtner, "Photonic ADC: Overcoming the bottleneck of electronic jitter," *Optics Express*, vol. 20, no. 4, pp. 4454–4469, Feb. 2012.

[11] J. Capmany, J. Mora, I. Gasulla, J. Sancho, J. Lloret, and S. Sales, "Microwave Photonic Signal Processing," *Journal of Lightwave Technology*, vol. 31, no. 4, pp. 571–586, Feb. 2013.

[12] R. A. Minasian and X. Yi, "Advances in High-speed and Adaptive Microwave Photonic Signal Processing," *Procedia Engineering*, vol. 140, pp. 217–224, Jan. 2016.

[13] Z. Tang, Y. Li, J. Yao, and S. Pan, "Photonics-Based Microwave Frequency Mixing: Methodology and Applications," *Laser & Photonics Reviews*, vol. 14, no. 1, p. 1800350, 2020.

[14] X. Li, J. Yu, and G.-K. Chang, "Photonics-Aided Millimeter-Wave Technologies for Extreme Mobile Broadband Communications in 5G," *Journal of Lightwave Technology*, vol. 38, no. 2, pp. 366–378, Jan. 2020.

[15] C. Vagionas, E. Ruggeri, A. Tsakyridis, G. Kalfas, Y. Leiba, A. Miliou, and N. Pleros, "Linearity Measurements on a 5G mmWave Fiber Wireless IFoF Fronthaul Link With Analog RF Beamforming and 120° Degrees Steering," *IEEE Communications Letters*, vol. 24, no. 12, pp. 2839–2843, Dec. 2020.

[16] D. Paredes Páliz, G. Royo, F. Aznar, C. Aldea, and S. Celma, "Radio over Fiber: An Alternative Broadband Network Technology for IoT," *Electronics*, vol. 9, p. 1785, Oct. 2020.

[17] P. Ghelfi, F. Laghezza, F. Scotti, G. Serafino, S. Pinna, D. Onori, E. Lazzeri, and A. Bogoni, "Photonics in Radar Systems: RF Integration for State-of-the-Art Functionality," *IEEE Microwave Magazine*, vol. 16, no. 8, pp. 74–83, Sep. 2015.

[18] P. Ghelfi, F. Scotti, D. Onori, and A. Bogoni, "Photonics for Ultrawideband RF Spectral Analysis in Electronic Warfare Applications," *IEEE Journal of Selected Topics in Quantum Electronics*, vol. 25, no. 4, pp. 1–9, Jul. 2019.

[19] J. Hervás, A. L. Ricchiuti, W. Li, N. H. Zhu, C. R. Fernández-Pousa, S. Sales, M. Li, and J. Capmany, "Microwave Photonics for Optical Sensors," *IEEE Journal of Selected Topics in Quantum Electronics*, vol. 23, no. 2, pp. 327–339, Mar. 2017.

[20] S. Zhu, S. Zhu, S. Zhu, X. Fan, X. Fan, X. Fan, M. Li, M. Li, M. Li, N. H. Zhu, N. H. Zhu, N. H. Zhu, W. Li, W. Li, and W. Li, "Microwave photonic frequency down-conversion and channel switching for satellite communication," *Optics Letters*, vol. 45, no. 18, pp. 5000–5003, Sep. 2020.

[21] S. Weber, E. H. Waller, C. Kaiser, and G. von Freymann, "Time-stretched real-time measurement technique for ultrafast absorption variations with TS/s sampling-rate," *Optics Express*, vol. 25, no. 13, pp. 14 125–14 133, Jun. 2017.

[22] D. Novak, R. B. Waterhouse, A. Nirmalathas, C. Lim, P. A. Gamage, T. R. Clark, M. L. Dennis, and J. A. Nanzer, "Radio-Over-Fiber Technologies for Emerging Wireless Systems," *IEEE Journal of Quantum Electronics*, vol. 52, no. 1, pp. 1–11, Jan. 2016.

[23] A. Ly, V. Auroux, R. Khayatzadeh, N. Gutierrez, A. Fernandez, and O. Llopis, "Highly Spectrally Pure 90-GHz Signal Synthesis Using a Coupled Optoelectronic Oscillator," *IEEE Photonics Technology Letters*, vol. 30, no. 14, pp. 1313–1316, Jul. 2018.

[24] V. Billault, V. Crozatier, G. Baili, L. Morvan, D. Dolfi, N. Kanagaraj, and H. G. de Chatellus, "Phase Noise of Optical Pulse Trains Generated by Talbot Effect in Frequency Shifting Loops," *Journal of Lightwave Technology*, vol. 39, no. 8, pp. 2336–2347, Apr. 2021.

[25] B. C. Pile and G. W. Taylor, "Performance of Subsampled Analog Optical Links," *Journal of Lightwave Technology*, vol. 30, no. 9, pp. 1299–1305, May 2012.

[26] P. W. Juodawlkis, J. C. Twichell, G. E. Betts, J. J. Hargreaves, R. D. Younger, J. L. Wasserman, F. J. O'Donnell, K. G. Ray, and R. C. Williamson, "Optically sampled analog-to-digital converters," *IEEE Transactions on Microwave Theory and Techniques*, vol. 49, no. 10, pp. 1840–1853, Oct. 2001.

[27] P. T. Callahan, M. L. Dennis, and T. R. C. Jr, "Photonic Analog-to-Digital Conversion," *Johns Hopkins APL Technical Digest*, vol. 30, no. 4, pp. 280–286, Jan. 2012.

[28] R. Williamson, P. Juodawlkis, J. Wasserman, G. Betts, and J. Twichell, "Effects of crosstalk in demultiplexers for photonic analog-to-digital converters," *Journal of Lightwave Technology*, vol. 19, no. 2, pp. 230–236, Feb. 2001.

[29] R. Williamson, R. Younger, P. Juodawlkis, J. Hargreaves, and J. Twichell, "Precision calibration of an optically sampled analog-to-digital converter," in *Proc. 2003 Digest of LEOS Summer Topical Meeting (Cat. No.03TH8701)*, Jul. 2003, pp. MC4.2/22–MC4.2/23.

[30] A. Yariv and R. G. M. P. Koumans, "Time interleaved optical sampling for ultra-high speed A/D conversion," *Electronics Letters*, vol. 34, no. 21, pp. 2012–2013, Oct. 1998.

[31] J. U. Kang and R. D. Esman, "Demonstration of time interweaved photonic four-channel WDM sampler for hybrid analogue-digital converter," *Electronics Letters*, vol. 35, no. 1, pp. 60–61, Jan. 1999.

[32] Y. Han, O. Boyraz, and B. Jalali, "Ultrawide-band photonic time-stretch a/D converter employing phase diversity," *IEEE Transactions on Microwave Theory and Techniques*, vol. 53, no. 4, pp. 1404–1408, Apr. 2005.

[33] B. Jalali and Y. Han, *Microwave Photonics*. CRC Press, Dec. 2006, ch. Tera Sample Per-Second Time- Stretched Analog-to-Digital Conversion.

[34] J. Chou, O. Boyraz, D. Solli, and B. Jalali, "Femtosecond real-time single-shot digitizer," *Applied Physics Letters*, vol. 91, no. 16, p. 161105, Oct. 2007.

[35] V. A. Thomas, M. El-Hajjar, and L. Hanzo, "Millimeter-Wave Radio Over Fiber Optical Upconversion Techniques Relying on Link Nonlinearity," *IEEE Communications Surveys Tutorials*, vol. 18, no. 1, pp. 29–53, Apr. 2016.

[36] Chul Soo Park, Choong Keun Oh, Chung Ghiu Lee, Dong-Hwan Kim, and Chang-Soo Park, "A photonic up-converter for a WDM radio-over-fiber system using cross-absorption modulation in an EAM," *IEEE Photonics Technology Letters*, vol. 17, no. 9, pp. 1950–1952, Sep. 2005.

[37] J. Thouras, B. Benazet, H. Leblond, and C. Aupetit-Berthelemot, "Photonic radio frequency down-converter based on parallel electro-absorption modulators in Ku/Ku band for space applications," in *Proc. 2016 21st OptoElectronics and Communications Conference (OECC) Held Jointly with 2016 International Conference on Photonics in Switching (PS)*, Jul. 2016, pp. 1–3.

[38] A. W. Mohammad, H. Shams, C. Liu, C. Graham, M. Natrella, A. J. Seeds, and C. C. Renaud, "60-GHz Transmission Link Using Uni-Traveling Carrier Photodiodes at the Transmitter and the Receiver," *Journal of Lightwave Technology*, vol. 36, no. 19, pp. 4507–4513, Oct. 2018.

[39] W. Shieh, S. Yao, G. Lutes, and L. Maleki, "An all-optical microwave mixer with gain [using semiconductor optical amplifier]," in *Proc. Optical Fiber Communication Conference*, Feb. 1997, pp. 263–264.

[40] Y.-K. Seo, C.-S. Choi, and W.-Y. Choi, "All-optical signal up-conversion for radio-on-fiber applications using cross-gain modulation in semiconductor optical amplifiers," *IEEE Photonics Technology Letters*, vol. 14, no. 10, pp. 1448–1450, Oct. 2002.

[41] C. Bohemond, T. Rampone, and A. Sharaiha, "Performances of a Photonic Microwave Mixer Based on Cross-Gain Modulation in a Semiconductor Optical Amplifier," *Journal of Lightwave Technology*, vol. 29, no. 16, pp. 2402–2409, Aug. 2011.

[42] H.-J. Song, J. S. Lee, and J.-I. Song, "Signal up-conversion by using a cross-phase-modulation in all-optical SOA-MZI wavelength converter," *IEEE Photonics Technology Letters*, vol. 16, no. 2, pp. 593–595, Feb. 2004.

[43] H.-J. Kim and J.-I. Song, "All-optical single-sideband upconversion with an optical interleaver and a semiconductor optical amplifier for radio-over-fiber applications," *Optics Express*, vol. 17, no. 12, p. 9810, Jun. 2009.

[44] D.-H. Kim, J.-Y. Lee, H.-J. Choi, and J.-I. Song, "All-optical single-sideband frequency upconversion utilizing the XPM effect in an SOA-MZI," *Optics Express*, vol. 24, no. 18, p. 20309, Sep. 2016.

[45] H. Termos, T. Rampone, A. Sharaiha, A. Hamié, and A. Alaeddine, "All-Optical Radiofrequency Sampling Mixer Based on a Semiconductor Optical Amplifier Mach–Zehnder Interferometer Using a Standard and a Differential Configuration," *Journal of Lightwave Technology*, vol. 34, no. 20, pp. 4688–4695, Oct. 2016.

[46] T. Rampone, A. Lagrost, A. Sharaiha, and A. Kabalan, "Optical Radiofrequency Signal Mixing by All-Optical Sampling Based on a Semiconductor Optical Amplifier Mach–Zehnder Interferometer," *Journal of Lightwave Technology*, vol. 31, no. 23, pp. 3597–3602, Dec. 2013.

[47] H.-J. Kim, S.-H. Lee, and J.-I. Song, "Generation of a 100-GHz optical SSB signal using XPM-based all-optical frequency upconversion in an SOA-MZI," *Microwave and Optical Technology Letters*, vol. 57, no. 1, pp. 35–38, 2015.

[48] M. J. Connelly, *Semiconductor Optical Amplifiers*. Boston: Kluwer Academic Publishers, 2004.

[49] S. Nakamura, Y. Ueno, K. Tajima, J. Sasaki, T. Sugimoto, T. Kato, T. Shimoda, M. Itoh, H. Hatakeyama, T. Tamanuki, and T. Sasaki, "Demultiplexing of 168-Gb/s data pulses with a hybrid-integrated symmetric Mach-Zehnder all-optical switch," *IEEE Photonics Technology Letters*, vol. 12, no. 4, pp. 425–427, Apr. 2000.

Chapter 2

Fundamentals of SOA-MZI sampler

In this chapter, the notions of sampling in general and optical sampling in particular are discussed in section 2.1. Subsequently, the background of ADCs and photonic mixers, which are applications of the optical sampling, are presented in section 2.2. Thereafter, general information on the SOA are provided concerning its structure and its non-linear effects, as well as the model equations used in this thesis and its main characteristics are demonstrated in section 2.8. Next, in section 2.4, the principle of operation of the SOA-MZI is explained, and then a detailed derivation of the SOA-MZI equations is demonstrated, followed by the static and dynamic characterizations of the SOA-MZI module, which are theoretically analyzed and experimentally investigated.

2.1 Theory of Sampling

2.1.1 Introduction

Optical or electric signals are passed between devices, modules and users in order to send and receive information, which might be video, audio, or some sort of encoded data. Aiming to process these analog signals and either convert them to digital binary code or transmit them, the first step is the sampling of these signals, which serves as the interface between the received analog signals and the digital domain. Sampling is a process of transforming an analog signal to a series of pulses. The amplitude of each pulse is representative of that of the input signal at each sampling instant. In other words, sampling of a signal consists of taking the instantaneous amplitude or power values of a signal at defined regular time intervals.

The sampling of an analog sinusoidal signal $x(t)$ is shown in Figure 2.1. Mathematically, in order to get the sampled $y(t)$ signal at the output of the sampler, the continuous signal $x(t)$ is multiplied by a periodic sequence of impulses or the Dirac comb function $\sqcup\!\sqcup_{T_{ck}}(t)$. The sampling frequency or sampling rate is f_{ck} and the temporal resolution of $y(t)$ is equal to $T_{ck} = \frac{1}{f_{ck}}$. $y(t)$ is given by the Equation:

$$y(t) = x(t) \cdot \sqcup\!\sqcup_{T_{ck}}(t) = x(t) \cdot \sum_{k} \delta(t - kT_{ck}) \tag{2.1}$$

The process of sampling in the frequency domain is shown in Figure 2.2. The signal to be

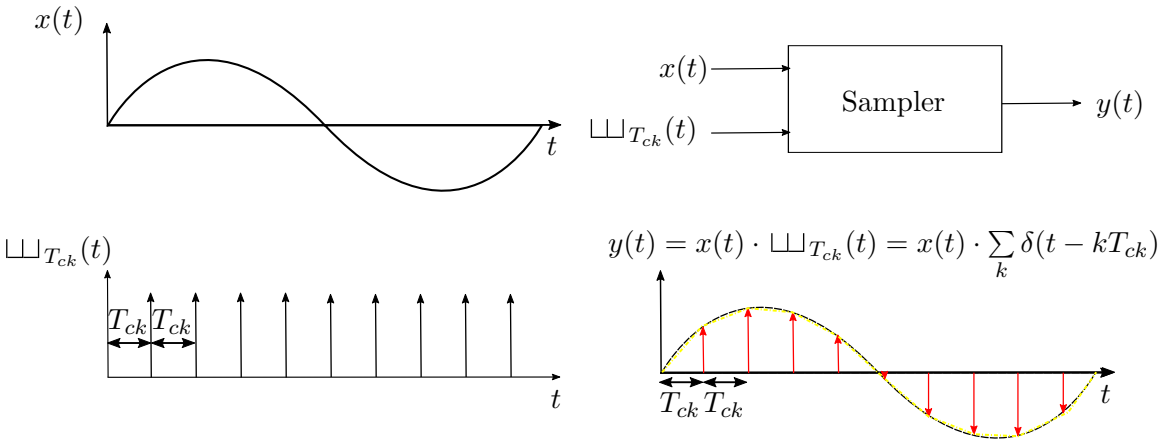

Figure 2.1: Sampling of sinusoidal signal $x(t)$. The sampling process mathematically consists of multiplying analog $x(t)$ by Dirac comb, $\sqcup\!\sqcup_{T_{ck}}(t)$. The envelope of the sampled signal $y(t)$, denoted by the dashed black line, is the original signal $x(t)$.

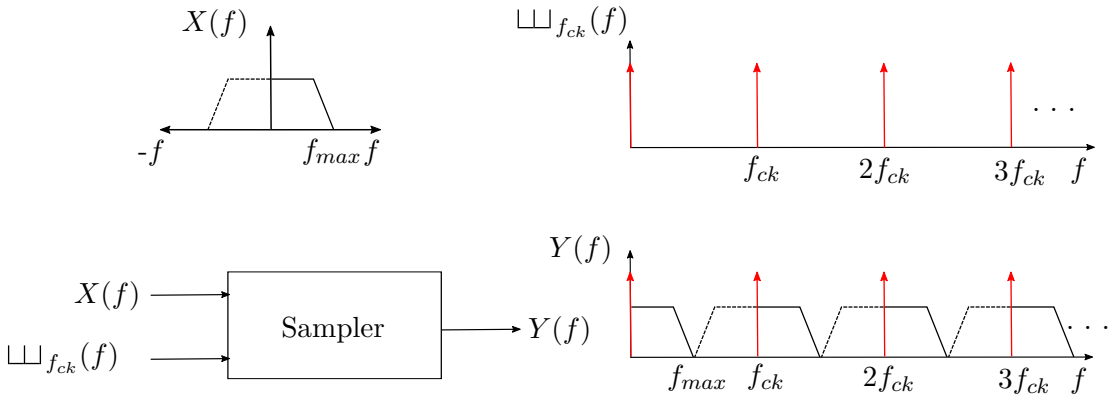

Figure 2.2: Sampling of signal X(f) in the frequency domain. Dirac comb, $\sqcup\!\sqcup_{f_{ck}}(f)$, in the frequency domain. Through sampling, the frequency content of X(f) is copied around the equidistant frequency components of Dirac comb in Y(f).

sampled, $X(f)$, is a base-band signal with f_{max} its highest frequency component. It should be noted that the Fourier transform of a Dirac comb is a Dirac comb, and thus the form of the

sampling signal is unchanged between the time and frequency domains. The process of sampling of $x(t)$ in the time domain results in the replication of $X(f)$ in the frequency domain. More precisely, the Fourier transform of the sampled signal, $Y(f)$, occurs from the replication of the frequency content of the signal to be sampled, $X(f)$, at the frequency components of Dirac comb, $\sqcup\!\sqcup_{f_{ck}}(f)$, as shown in Figure 2.2.

An important question that arises concerning the sampling process is which is the minimum sampling frequency that will allow for the accurate reconstruction of the analog signal $X(f)$. According to the Nyquist-Shannon sampling theorem, the minimum sampling frequency should be double the highest frequency component, f_{max}, of the signal to be sampled, so that the underlying information in $X(f)$ will not be distorted. In other words, the sampling rate should be such that we take at least two samples for every period of the maximum frequency component of the signal to be sampled. Mathematically, the Nyquist-Shannon sampling theorem can be expressed by:

$$f_{ck} \geq 2f_{max} = f_N \tag{2.2}$$

where f_N is the Nyquist frequency

There are three cases that characterize the sampling process depending on the relation between f_{max} and f_{ck}, shown in Figure 2.3. The first case where $f_{ck} \gg f_N$ is named oversampling. The second case where $f_{ck} = f_N$ is named Nyquist sampling. The third and final case where $f_{ck} < f_N$ is named undersampling. In the case of undersampling of a base-band signal, the undesired phenomenon of aliasing is expected which distorts the underlying information of signal $X(f)$ and makes its faithful reconstruction impossible. In Figure 2.3, the frequency ranges where aliasing takes place are shaded.

Another characteristic value of the sampler is the input range of amplitudes, $\Delta_{sampler}$, over which the sampler functions efficiently.

2.1.2 Sampler performance limitation factors

2.1.2.1 Temporal jitter of sampling clock

Ideally, the sampling signal is a perfect Dirac comb where the pulses are instantaneous and perfectly periodic. However, in reality, there is an uncertainty, Δt, on the sampling instant for both electronic clocks and optical pulse clocks, which is an important limiting performance factor, especially at high sampling frequencies.

A quantification of the error induced by the temporal jitter of the sampling clock to the sampled signal is presented in the following.

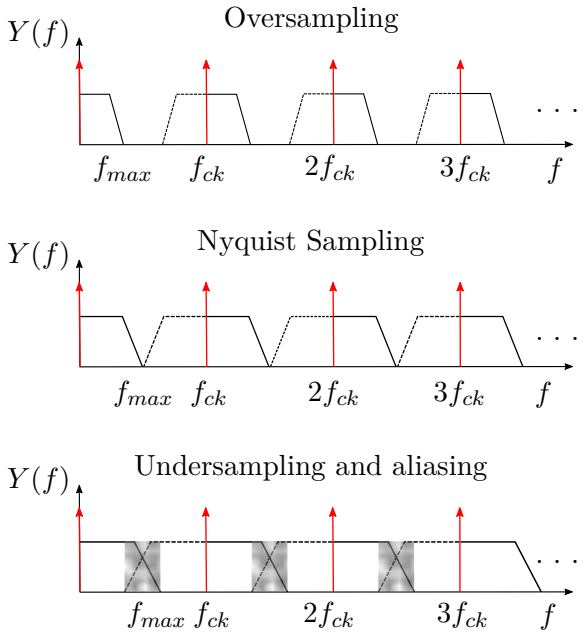

Figure 2.3: Examples of oversampling $f_{ck} \gg f_N$, Nyquist sampling $f_{ck} = f_N$, undersampling $f_{ck} < f_N$. Aliasing is expected in the shaded parts of the spectrum.

A time-domain sinusoidal signal to be sampled is given by:

$$x(t) = A \cdot \sin(\omega t) \tag{2.3}$$

The introduction of the temporal jitter, Δt, leads to an error, Δx, in the value of the sampled signal.

By differentiating Equation (2.3) and applying the temporal jitter Δt, the following expression is obtained:

$$\Delta x = \omega A \cdot \cos(\omega t) \cdot \Delta t \tag{2.4}$$

Then, the maximum error due to the temporal jitter is:

$$\Delta x_{max} = 2\pi f \cdot A \cdot \Delta t \tag{2.5}$$

Finally, the rms error is equal to:

$$\Delta x_{rms} = \frac{A}{\sqrt{2}} \cdot 2\pi f \cdot \Delta t_{rms} \tag{2.6}$$

An important observation to be noticed from Equation (2.6) is that the rms error is proportional to the amplitude, the frequency of the signal to be sampled and the rms jitter of the

sampling signal. Assuming that jitter is the only source of error, the Signal to Noise Ratio (SNR) can be determined by the following Equation [1]:

$$SNR = 20\,log_{10}\left(\frac{A/\sqrt{2}}{\Delta x_{rms}}\right) = 20\,log_{10}\left(\frac{1}{2\pi f \cdot \Delta t_{rms}}\right) \tag{2.7}$$

The lower temporal jitter of optical samplers compared to electronic samplers, stems from the fact that the temporal jitter variance of the mode-locked laser (MLL) is proportional to its pulses width, which can be as low as few femtoseconds, whereas the temporal jitter variance of microwave oscillators is proportional to the period of the microwave signal, which is typically equal to hundreds of picoseconds. Supposing that the mode/pulse energy and the cavity decay times are similar, an MLL can easily achieve two orders of magnitude less timing jitter compared to a microwave oscillator [2].

2.1.2.2 White Noise

2.1.2.2.1 Thermal Noise

Thermal noise, also known as Johnson noise, is generated by electrical resistors used in electronic or opto-electronic communications. Thermal noise is a Gaussian process and its spectral density is given by [3]:

$$\sigma_{th}^2 = \frac{4kT}{R_L} \tag{2.8}$$

where k is the Boltzmann's constant, T is the absolute temperature and R_L is the load's resistance. The unit of σ_{th}^2 is $[A^2/Hz]$.

2.1.2.2.2 Shot noise

Shot noise describes the fluctuations of the number of photons in a photodiode or electrons in a resistor due to the discrete or corpuscular nature of photons and electrons, respectively. Shot noise poses a fundamental limit to the optical intensity noise as observed in many situations such as the measurements with a photodiode. Shot noise is a Poisson process and its spectral density can be expressed by [3]:

$$\sigma_s^2 = 2qI_s = 2qrP_s \tag{2.9}$$

where q is the elementary charge, I_s is the photo-current produced by the photodiode, r with units $[A/W]$ is the responsivity of the photodiode and represents its conversion efficiency and P_s is the received optical power. The unit of σ_s^2 is $[A^2/Hz]$.

The spectral density of the thermal and shot noise are both independent of frequency, and thus can be approximated together as white noise [4]. White noise follows a Gaussian distribution

and the mean-square value of its current is given by:

$$N_{white} = 4kT \cdot R_{eff} \cdot \frac{f_{ck}}{2} \tag{2.10}$$

where R_{eff} is effective equivalent resistance modeling the thermal and shot noise. The unit of N_{white} is $[V^2]$.

2.1.2.3 Total Harmonic Distortion

Figures 2.1, 2.2 and 2.3 present ideal sampling cases, where there is not second or higher term intermodulation products at the output of the sampler. However, in a real sampler, there is a level of harmonic distortion depending on the operating conditions of the sampler, which causes a distortion of the underling information and poses a limiting factor to its faithful reconstruction. In Figure 2.4, an example of sampling with harmonic distortion is presented. The signal to be sampled is a sinusoidal signal $X(f)$ at frequency f_{dat}. The spectrum of the sampled signal $Y(f)$ is richer than in the ideal case and additionally to the desired replicas at $if_{ck} \pm f_{dat}$, shown in blue color, unwanted replicas appear at $if_{ck} \pm 2f_{dat}$, depicted in green colour and at $if_{ck} \pm 3f_{dat}$, illustrated in magenta color. In the case of even higher harmonic distortion, replicas at $if_{ck} \pm mf_{dat}$ with $m = 4, 5, 6,..$ can appear, which will ultimately interfere with the desired replicas at $if_{ck} \pm f_{dat}$, significantly and irreversibly distorting the sampled signal. In order to quantify the harmonic distortion, the Total Harmonic Distortion (THD) in the full Nyquist band (0, $f_{ck}/2$) is defined as:

$$THD_{dB} = 10\,log\frac{P_{2f_{dat}} + P_{3f_{dat}} + ... + P_{nf_{dat}}}{P_{f_{dat}}} \tag{2.11}$$

where $P_{nf_{dat}}$, $n = 1, 2, ..., n$ is the sampled signal power at frequency nf_{dat}.

2.2 Sampling Applications

2.2.1 ADC

The ADC is a key application in which a sampler is used. In Figure 2.5, the different steps or phases that an analog signal passes inside an ADC are presented, in order to be converted to a digital one. The first such phase is sampling in which the analog signal (Figure 2.5(a)) is converted to a discrete-time continuous amplitude signal (Figure 2.5(b)). The second phase is quantization, which is performed by rounding the amplitude of the sampled signal to the nearest discrete level while keeping it constant until the next sample (Figure 2.5(c)). Finally, the quantized signal is converted to a digital signal (discrete-time, discrete-amplitude signal), where each quantized sample is expressed in the form of an n-bit binary code (3-bits in Figure

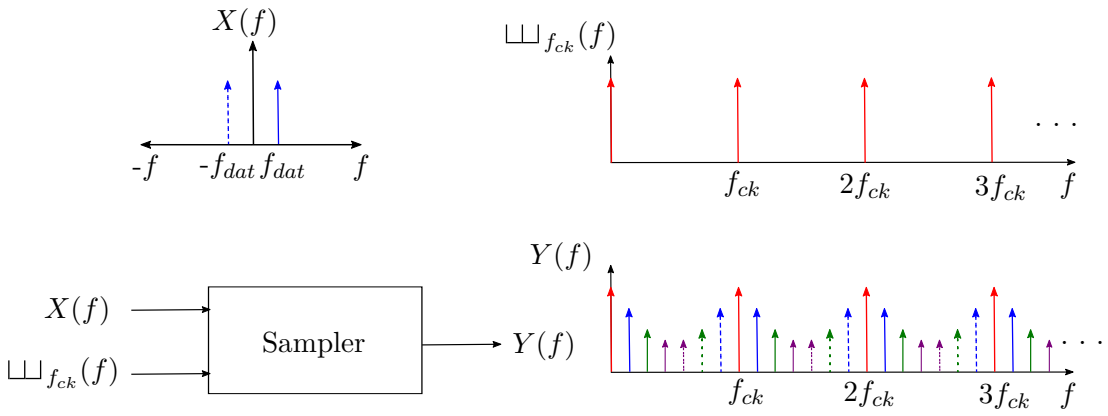

Figure 2.4: Effect of harmonic distortion on the process of sampling. Replicas of the signal to be sampled $X(f)$ appear at frequencies $if_{ck} \pm 2f_{dat}$ and $if_{ck} \pm 3f_{dat}$, filling the spectrum of the sampled signal $Y(f)$.

2.5(d)). An n-bit ADC has 2^n quantization levels. In the general case, i.e., when the nature and the distribution of the signal to be digitized (sinusoidal, triangular, any) are unknown, a so-called uniform quantization law is used, where the quantization levels are equally spaced. Another characteristic of the ADC is the resolution Q, which signifies the amplitude interval assigned in between two consecutive code levels, and it is defined as:

$$Q = \frac{A_{ref}}{2^n} \tag{2.12}$$

where A_{ref} is the full scale amplitude range or scale of ADC. Also, Q is equal to the Least Significant Bit (LSB) amplitude. As an example, in Figure 2.5(d), $Q = LSB = \frac{2A}{2^3} = \frac{A}{2^2}$, where A is the amplitude of the sinusoidal signal to be sampled.

2.2.2 Sampling Mixers

Another critical application of a sampler is its employment as a frequency converter for both up- and down-conversion.

2.2.2.1 Up-conversion with Nyquist sampling or oversampling

Using Nyquist sampling or oversampling, a signal is replicated around the multiples of the repetition frequency f_{ck}. This property of sampling can be exploited in order to up-convert a signal from f_{dat} to $if_{ck} \pm f_{dat}$. In Figure 2.6, the signal $X(f)$ is sampled at a sampling rate

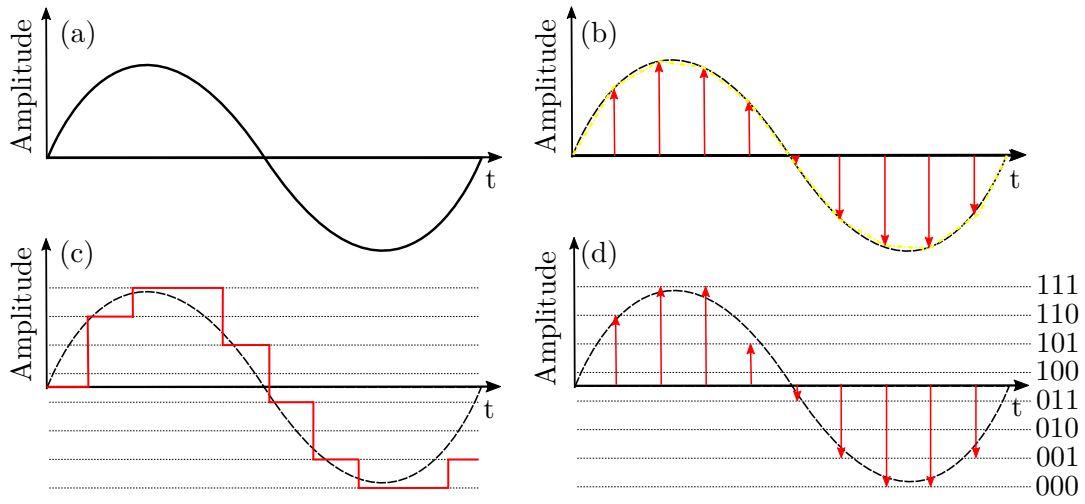

Figure 2.5: The different steps of analog to digital conversion. (a) The analog input signal (continuous-time, continuous-amplitude). (b) The sampled signal (discrete-time, continuous-amplitude). (c) The quantized signal (continuous-time, discrete-amplitude signal). (d) The digital output signal. Each quantized sample is converted to a 3 bit code, a discrete-time, discrete-amplitude signal. The input signal is shown in dashed line in (b), (c) and (d) for comparison. The discrete quantization levels are shown in dotted lines in (c) and (d).

f_{ck}, where $f_{ck} > f_N$, in accordance to the Nyquist-Shannon sampling theorem, intending to avoid aliasing. The spectrum of the sampled intermediate frequency signal Y(f) after sampling is shown in Figure 2.6. Finally, the replica around $3f_{ck} + f_{dat}$ passes through, whereas the rest of $Y(f)$ frequency content is discarded by the filter. In Figure 2.6, the filter is supposed to be ideal, so that its passband has the shape of a brickwall.

2.2.2.2 Down-conversion with band-pass sampling

In band-pass sampling, a signal in the radio frequencies (RF) is relocated to lower RF frequencies or to an intermediate frequency or to the base-band.

The spectrum of a band-pass signal $X(f)$, centered at RF frequency f_{dat} with a bandwidth BW, defined between a minimum frequency f_{min} and a maximum frequency f_{max}, is depicted in Figure 2.7. Signal $X(f)$ is sampled at a sampling rate f_{ck}, which is below the frequency content of the band-pass signal. Moreover, the sampling rate is chosen so that the spectral replicas of positive and negative bands just shift against each other but do not overlap. The spectrum of the sampled band-pass signal, $Y(f)$, is shown in Figure 2.7. Finally, the desired replica of the 1^{st} Nyquist zone passes through the filter, while the rest of Nyquist zones are discarded. In Figure 2.7, the filter is supposed ideal as in Figure 2.6.

In case of band-pass sampling, more relaxed constraints on the sampling rate than that of the Nyquist-Shannon sampling theorem can be applied, which ensure equally that the underline

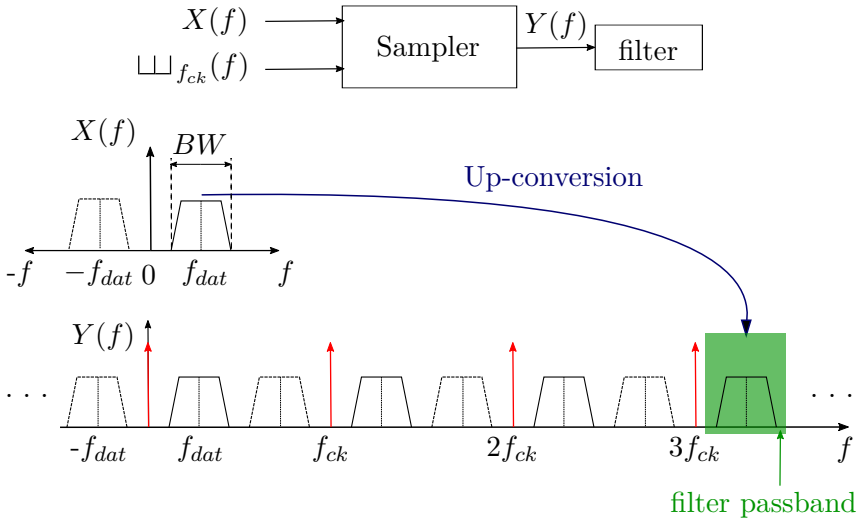

Figure 2.6: Conceptual diagram of base-band sampling for the purpose of up-conversion. The original base-band signal spectrum is $X(f)$. The sampled signal spectrum is Y(f). BW is the bandwidth of the band-pass signal. The band-pass filter allows only the replica around $3f_{ck}+f_{dat}$ to pass, whereas it discards the rest of the frequency components of Y(f).

information in $X(f)$ will not be distorted. According to the band-pass theory [5], the sampling rate should be confined in the range of frequencies defined by:

$$\frac{2f_{max}}{n} \leq f_{ck} \leq \frac{2f_{min}}{n-1} \iff \frac{2f_{dat}+BW}{n} \leq f_{ck} \leq \frac{2f_{dat}-BW}{n-1} \tag{2.13}$$

where n is an integer which satisfies:

$$1 \leq n \leq I_g\left[\frac{f_{max}}{BW}\right] \iff 1 \leq n \leq I_g\left[\frac{2f_{dat}+BW}{2BW}\right] \tag{2.14}$$

where $I_g\left[\frac{X}{Y}\right]$ is the quotient of Euclidean division $\frac{X}{Y}$.

A marginal case is when f_{max} is an exact multiple of BW and $n = \frac{f_{max}}{BW}$. In this case, Equation (2.13) becomes:

$$2BW \leq f_{ck} \leq 2BW \iff f_{ck} = 2BW \tag{2.15}$$

In a real system, this is a dangerous case because any imperfection or instability in the sampling rate will be a cause of aliasing.

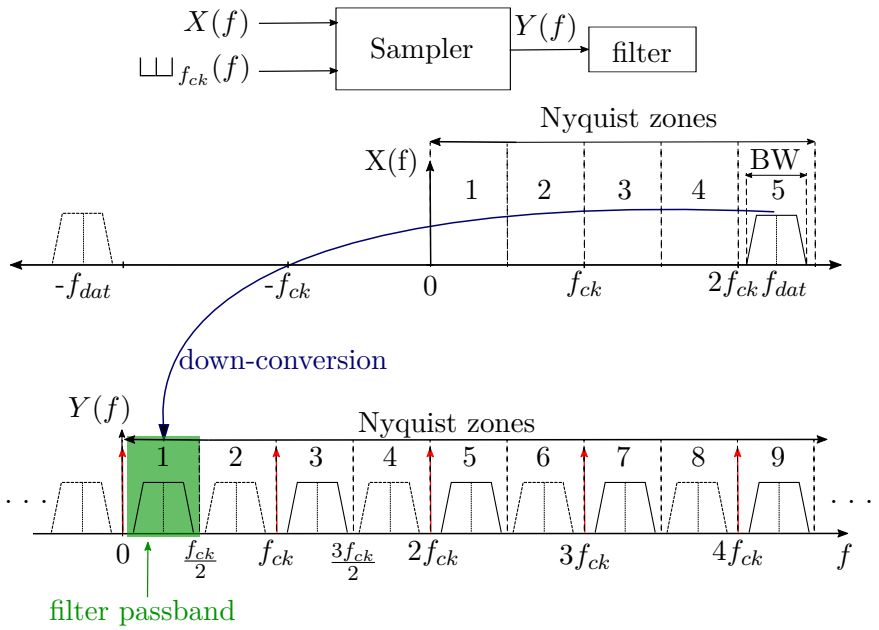

Figure 2.7: Conceptual diagram of band-pass sampling for the purpose of down-conversion. The original band-pass signal spectrum is $X(f)$. The sampled signal spectrum is $Y(f)$. BW is the bandwidth of the band-pass signal. The filter lets only the first Nyquist zone of Y(f) to pass, whereas it discards the higher order Nyquist zones.

2.2.2.3 Conversion Gain

A key parameter for the characterization of a mixer's performance is the Conversion Gain (CG). CG is defined as the ratio of desired output power level at $if_{ck} \mp f_{dat}$ to the input power level at f_{dat}. If CG is negative as it is the case for many passive mixers it is common to refer to conversion loss instead of CG.

2.3 SOA Background

An SOA is a type or category of optical amplifiers, and as such it can, under appropriate operating conditions, amplify an incident light signal directly without the need to first convert it into an electrical signal. An SOA is essentially a laser diode (LD) with no optical feedback from its input and output ports, and hence is also referred to as a Traveling-Wave Amplifier (TWA).

2.3.1 Structure

A basic structure of an SOA is shown in Figure 2.8. Its main element is the active region of semiconductor material, which provides optical gain when the amplifier is electrically pumped. The device is driven by an electric current. Pumping is necessary to achieve the population inversion and therefore the stimulated emission, which is the mechanism that conveys the gain. However, due to the population inversion undesired spontaneous emission is also produced and amplified, giving rise to the Amplified Spontaneous Emission (ASE) noise. An integrated waveguide is used to confine the signal wave to the active region. The laser effect is suppressed by an anti-reflective treatment of the entry and exit facets. The reflectivity of the output facets must be as low as possible in order to eliminate optical reflections and to induce a very low ripple of the optical gain of the SOA.

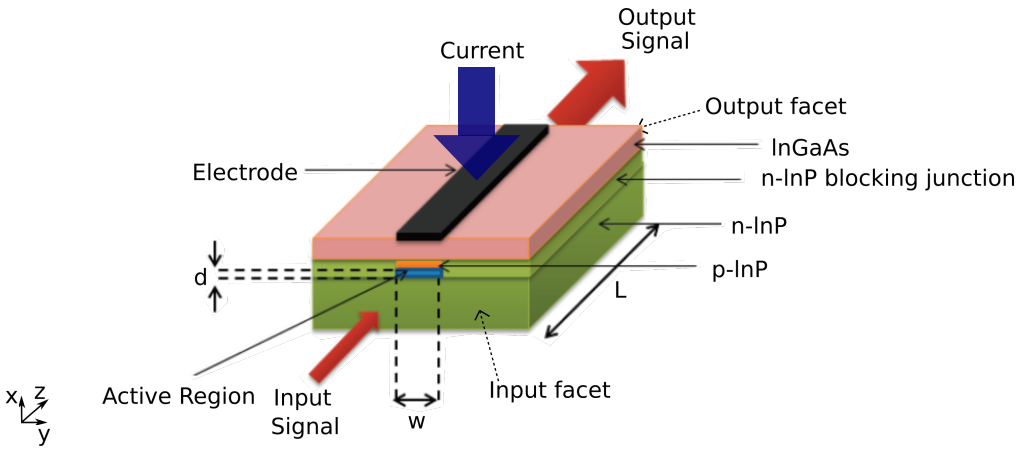

Figure 2.8: Basic structure of a Semiconductor optical amplifier. L, d and w are the length, thickness and width of the active area, respectively.

2.3.2 SOA non-linearities

Although SOAs were originally used to amplify optical signals to compensate for optical fiber losses during transmission, to date they have been widely used in signal processing applications such as optical switching, logic gates, wavelength conversion and frequency converters, exploiting their non-linear properties based on Cross-Gain modulation (XGM), Cross-Phase modulation (XPM) and Four-Wave Mixing (FWM) [6–8]. The saturated gain response of SOAs, which is in the order of a few tens of picoseconds, allows operation at very high bit rates well beyond 100 Gb/s [9, 10]. For this reason, the use of SOAs in optical signal processing circuits in a purely

photonic manner is a milestone technology on the road to the implementation of high-speed optical networks [11].

2.3.2.1 Cross-Gain Modulation

One mechanism of interaction between two optical signals, one of high power (pump signal) and one of low power (probe signal) at different wavelengths, entering simultaneously into an SOA is due to the XGM effect. In this case, the pump signal modulates the carrier density and ultimately the gain of the amplifier, imposing a corresponding modulation in the gain that the probe signal experiences while traversing the SOA.

2.3.2.2 Cross-Phase Modulation

A second effect present when a pump signal and a probe signal enter into the active region of an SOA is that the pump signal modulates the refractive index of the active region due to Kerr effect. This modulation of the refractive index causes a non-linear phase shift in the parallel probe signal passing simultaneously through the SOA. The modulation of the refractive index and the modulation of the gain are interconnected via the linewidth enhancement factor or Henry factor, α_H, given by the following expression [12]:

$$\alpha_H = -\frac{4\pi}{\lambda}\frac{\frac{\partial n_e}{\partial N}}{\frac{\partial g_n}{\partial N}} \tag{2.16}$$

where λ is the wavelength of the probe signal, n_e is the effective refractive index of the SOA active area, N is the carrier density and g_n is the SOA net gain. In order to exploit the phase variation due to XPM and convert it to an amplitude variation (PM-to-AM conversion), it is necessary to use modules such as the SOA-MZI, placing individual SOAs in the interferometric structure of the Mach-Zehder Interfererometer.

2.3.2.3 Four-Wave Mixing

FWM is a nonlinear process that occurs in an SOA when two optical signals, a pump signal at optical frequency f_{pump} and a probe signal at a lower optical frequency f_{probe} with same polarization traverse an SOA. In such event, the carrier density and ultimately the gain of the SOA is modulated by the frequency difference of the two signals, and finally a new third optical signal at a optical frequency $2f_{pump} - f_{probe}$ is produced [13].

2.3.3 SOA main characteristics

2.3.3.1 Gain

One of the most important characteristics of an SOA is its optical gain G which in dB is defined by:

$$G_{dB} = 10 \cdot log\left(\frac{P_{out} - P_{ASE}}{P_{in}}\right) \tag{2.17}$$

where P_{out} is the SOA output power, P_{ASE} is the power of the ASE and P_{in} is the SOA input power Typical values for the SOA gain are up to 35 dB.

2.3.3.2 Amplification bandwidth

The amplification or gain bandwidth of an SOA is defined as the width of the wavelength range where the optical gain is at most 3 dB below its maximum value. The amplification bandwidth of an SOA is a very important factor as it specifies its operational wavelength range. Typical values for the operational wavelength range are between 30 nm and 50 nm (or equivalently between 3.75 THz and 6.2 THz) [13].

2.3.3.3 Polarization Sensitivity

SOA gain is also polarization sensitive, thus presenting a different gain coefficient between TE and TM modes. However, polarization sensitivity can be mitigated using appropriate SOA construction techniques such as square cross-section or strained quantum well material in the active region to compensate the difference in the gain coefficients between TE and TM modes [14]. The polarization sensitivity of the SOAs used in our design, quantified by the metric of Polarization Dependant saturated Gain (PDG), is lower than 1 dB [15].

2.3.3.4 Noise

The noise of an optical amplifier is quantified in analogy with electric amplifiers by the noise figure. The noise figure of an SOA is defined in linear units as:

$$nf = \frac{SNR_{in}}{SNR_{out}} \tag{2.18}$$

where SNR_{in} is signal to noise ratio at the SOA input and SNR_{out} is the signal to noise ratio at the SOA output. The SNR of the amplified signal is degraded due to ASE that adds noise to the signal during the amplification process. The sources that contribute to the noise are [16]:

1. Signal-Shot beat noise
2. Signal and ASE shot noise

3. Signal-ASE beat noise
4. ASE-ASE beat noise
5. Thermal noise

SNR_{in} and SNR_{out} in Equation (2.18) are calculated assuming that the input and output powers of the amplifier are detected after narrow-band optical filtering by an ideal photo-detector whose performance is limited by the shot noise exclusively. In this case, the noise sources that need to be taken into account are the signal-ASE beat noise and the shot noise [14], and thus the noise figure in the dB scale is defined as:

$$NF = 10\,log\left(\frac{2P_{ASE}}{hv \cdot G \cdot B_0} + \frac{1}{G}\right) \tag{2.19}$$

where v is the optical frequency of the signal, B_0 is the resolution bandwidth of the measurement, P_{ASE} is the power of ASE noise at the SOA output.

The first term of parenthesis in Equation (2.19) is due to the Signal-ASE beat noise inside the resolution bandwidth, whereas the second term is due to the shot noise. For typical gain values the second term is neglected.

The ASE power at the amplifier's output, P_{ASE}, can be expressed as:

$$P_{ASE} = n_{sp}hv \cdot (G-1) \cdot B_0 \tag{2.20}$$

where n_{sp} is the spontaneous emission factor. Substituting Equation (2.20) in (2.19) under normal conditions where $G >> 1$, we obtain:

$$NF = 2n_{sp} \tag{2.21}$$

For an ideal amplifier n_{sp} is equal to 1, whereas for practical amplifiers n_{sp} is higher than 1. Thus, the theoretical lower limit of NF for SOAs is 3 dB [17]. Practical SOAs exhibit an NF significantly higher than the theoretical limit due to their intrinsic internal loss, ASE and the lower coupling efficiency at their input. Typical NF values of commercial SOAs are between 7 dB and 11 dB. The NF of an SOA depends on the operating wavelength, the operating current, and the input power of the incoming signal.

2.3.3.5 Saturation Power

SOA gain is constant for low power of input signals. However, as the power of the input signal increases, the SOA gain decreases as the carrier density in the active region gets depleted. The saturation power at the output, $P_{sat,out}$, is defined as the amplifier output power at which the amplifier gain is half the unsaturated gain in linear units, or 3 dB lower in dB units. A typical

gain characteristic as a function of the output power, as well as the $P_{sat,out}$ are shown in Figure 2.9. Using $P_{sat,out}$ the saturation power, P_{sat}, can be calculated from the expression [18]:

$$P_{sat,out} = ln2 \cdot P_{sat} \tag{2.22}$$

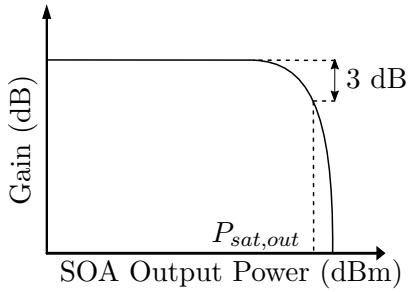

Figure 2.9: Gain Saturation

Typical values for SOA saturation powers are up to 10 dBm, however mode-adapted SOAs have been reported having saturation powers up to 17.4 dBm [19].

2.3.4 SOA modeling

This subsection is devoted to the SOA model and its equations permitting to quantify the effect of SOA non-linearities on the phase and on the amplitude of a signal traversing through an SOA.

The SOA model that we use is well known and is based on a two-level system approach with the rate-equation approximation [18]. In this model, the carrier density rate in the case of S input signals is described by:

$$\frac{\partial N(t)}{\partial t} = R_p - R(N(t)) - \sum_S R_S(N(t)) \tag{2.23}$$

where R_p is the carrier density rate supplied by the electric current which drives the SOA, R_S is the recombination rate due to the amplification of the S^{th} input signal at wavelength λ_S. R is the sum of the non-radiative R_{nr} and the recombination rate due to the ASE, $R_{ASE}(N)$. R_P is given by:

$$R_p = \frac{I_{SOA}}{qV} \tag{2.24}$$

where I_{SOA} is the SOA bias current, q is the elementary electron charge and V is the volume of

the SOA active region. R is given by:

$$R(N) = R_{nr}(N) + R_{ASE}(N) = \frac{N}{\tau_{eff}} \tag{2.25}$$

where τ_{eff} is the SOA effective carrier lifetime derived from τ_{nr}, which is related to R_{nr}, and τ_{ASE}, which is related to R_{ASE}, employing the Equation [20]:

$$\frac{1}{\tau_{eff}} = \frac{1}{\tau_{nr}} + \frac{1}{\tau_{ASE}} \tag{2.26}$$

Finally, R_S is given by:

$$R_S(N) = \frac{P_{i,S} \cdot \lambda_S}{hc} \cdot \frac{\Gamma \cdot g_m(N)}{g_n(N)} \cdot \frac{G(N) - 1}{V} \tag{2.27}$$

where $P_{i,S}$ is the input power of the S^{th} signal, λ_S is the wavelength of S^{th} signal, Γ is the optical confinement factor. g_m is the SOA material gain. We should note that we develop the SOA model on the assumption that the wavelengths λ_S of the S input signals are close enough (which is the case experimentally) that the SOA optical confinement factor, Γ, material gain, g_n, net gain, g_m and gain, G, are approximately constant in this wavelength range. The SOA material gain is given by the following Equation:

$$g_m(N) = \alpha(N - N_0) \tag{2.28}$$

where α is the peak-gain coefficient and N_0 is the carrier density at transparency. The SOA net gain is defined as:

$$g_n(N) = \Gamma \cdot g_m(N) - \alpha_{int} \tag{2.29}$$

where a_{int} is the internal losses, of the SOA.

The optical gain of the SOA is given with respect to carrier density by the following Equation [21]:

$$G(N(t)) = e^{g_n(N(t))L} = e^{\Gamma\alpha(N(t)-N_0)L-\alpha_{int}L} \tag{2.30}$$

The phase shift of the optical signal induced by an SOA with respect to the carrier density is given by [22]:

$$\Phi(N(t)) = -\frac{\alpha_H}{2} \cdot ln[G(N(t))] = -\frac{\alpha_H}{2} \left[\Gamma\alpha \left(N(t) - N_0\right) L - \alpha_{int}L\right] \tag{2.31}$$

2.4 SOA-MZI Basics

The most attractive example of a module exploiting the XPM phenomenon is the SOA-MZI, which converts the signal phase change into a power amplitude change based on the input condition of two optical signals traveling on different optical paths. Optical circuits based on Mach-Zehnder symmetric arrays and bearing in both arms semiconductor optical amplifiers (SOA-MZIs) have been used to date in a number of signal processing applications [23]. The most important advantages are the small amount of energy required to control the switching state of the switch and the ability to integrate into complex optical circuits with a large number of passive and active optical elements in the same chip, as well as their small size [24].

2.4.1 Principle of operation

The schematic diagram of a SOA-MZI, which corresponds to the module of CIP technologies with model name 40G-2R2-ORP [25] that is used in the experimental part of the thesis, is shown in Figure 2.10. Throughout the dissertation, the names of the SOA-MZI ports used are identical to the ones in the documentation of the device. The SOA-MZI is an optically controlled module which consists of a symmetrical architecture, where two SOAs are placed on each of the arms formed by 3 dB couplers C2, C3 and C4. In the general case, copies of the control signals A and D are introduced to the upper and lower arms of the SOA-MZI from the homonymous input ports through couplers C2 and C3, respectively. At the same time, another signal named C enters the module through input port C and is separated by the 3 dB coupler C1, to a pair of equal components, which travel independently along the SOA in their path. The following analysis is for signal C, however the analysis is identical for signal B entering from port B. Control signals A and D alter the nonlinear optical properties of the corresponding SOA and cause, through XPM, a phase difference between the split copies of signal C. Finally, the coupler C4 translates this phase difference of the split copies into changes in amplitude at the outputs I and J of the module. Thus the instantaneous power of control signals A and B define the fraction of the amplified input signal C that exits from I and J output ports.

2.4.2 SOA-MZI Model and Equations

The mathematical derivation of SOA-MZI powers at the outputs port I and J is given aiming at better understanding its principle of operation. Also, the final equations will be used in the following chapters.

This derivation starts with the electric field of the signals at the input ports B and C described by the relations $E_{in,B}(t) = E_B(t)e^{-j\omega_B t}$ and $E_{in,C}(t) = E_C(t)e^{-j\omega_C t}$, where E_B and E_C is the amplitude of the electric field at port B and C, respectively. After passing through the 3 dB input coupler, two copies emerge for every input electric field with equal amplitudes while a

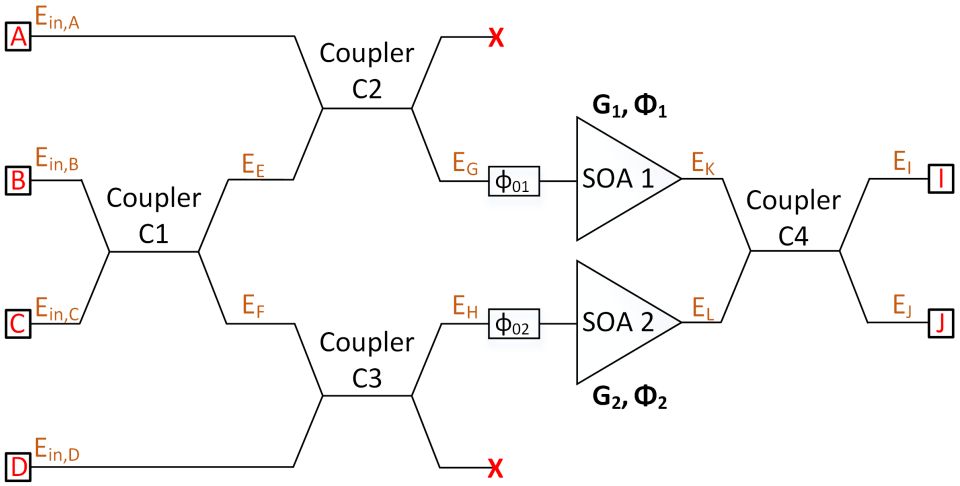

Figure 2.10: Detailed schematic diagram of the SOA-MZI module.

phase shift equal to $\frac{\pi}{2}$ is introduced to the crossover output port component of the coupler, i.e., to the lower coupler component due to $E_{in,B}$ and to the upper coupler component due to $E_{in,C}$. Thus:

$$E_E(t) = \frac{1}{\sqrt{2}} E_B(t) e^{-j\omega_B t} + \frac{1}{\sqrt{2}} E_C(t) e^{-j(\omega_C t + \frac{\pi}{2})} \tag{2.32}$$

$$E_F(t) = \frac{1}{\sqrt{2}} E_B(t) e^{-j(\omega_B t + \frac{\pi}{2})} + \frac{1}{\sqrt{2}} E_C(t) e^{-j\omega_C t} \tag{2.33}$$

Continuing our mathematical derivation of SOA-MZI model equations, the electric field of the signals at the input ports A and D are described by the relations $E_{in,A}(t) = E_A(t) e^{-j\omega_A t}$ and $E_{in,D}(t) = E_D(t) e^{-j\omega_D t}$, where E_A and E_D is the amplitude of the electric field at port A and D, respectively.

Couplers C2 and C3 in the upper arm and in the lower arm of the SOA-MZI, respectively, are essentially two 2X2 couplers in which one output port is disabled. More specifically, the upper port is disabled in coupler C2 and the lower port in coupler C3. Thus, following the same analysis as for couplers C2 and C3, the electric fields E_G and E_H can be derived:

$$\begin{aligned} E_G(t) &= \frac{1}{\sqrt{2}} E_E(t) + \frac{1}{\sqrt{2}} E_{in,A}(t) e^{-j\frac{\pi}{2}} \\ &= \frac{1}{2} E_B(t) e^{-j\omega_B t} + \frac{1}{2} E_C(t) e^{-j(\omega_C t + \frac{\pi}{2})} + \frac{1}{\sqrt{2}} E_A(t) e^{-(j\omega_A t + \frac{\pi}{2})} \end{aligned} \tag{2.34}$$

$$E_H(t) = \frac{1}{\sqrt{2}}E_F(t) + \frac{1}{\sqrt{2}}E_{in,D}(t)e^{-j\frac{\pi}{2}}$$
$$= \frac{1}{2}E_B(t)e^{-(j\omega_B t+\frac{\pi}{2})} + \frac{1}{2}E_C(t)e^{-j\omega_C t} + \frac{1}{\sqrt{2}}E_D(t)e^{-(j\omega_D t+\frac{\pi}{2})} \quad (2.35)$$

E_G and E_H are the electric fields of the signals introduced into the upper and the lower SOA-MZI arms. Initially, static phase shifts, ϕ_{01} and ϕ_{02}, by two phase shifters are applied to electric fields E_G and E_H, respectively, in order to properly adjust the phase relations between the two SOA-MZI arms and compensate for asymmetries in the couplers or between the two SOAs. Then, the phase shifted electric fields E_G and E_H enter into SOA1 and SOA2, respectively. Due to the non-linear phenomena of XGM and of XPM in the SOAs, in addition to the amplification $\sqrt{G_1}$ and $\sqrt{G_2}$, the electric fields undergo a phase shift, Φ_1 and Φ_2, respectively. Thus the electric fields E_K and E_L directly at the output of SOA1 and of SOA2 are:

$$E_K(t) = \sqrt{G_1}e^{-j(\Phi_1(t)+\phi_{01})}E_G(t)$$
$$= \frac{\sqrt{G_1}}{2}E_B(t)e^{-j(\omega_B t+\Phi_1(t)+\phi_{01})} + \frac{\sqrt{G_1}}{2}E_C(t)e^{-j(\omega_C t+\frac{\pi}{2}+\Phi_1(t)+\phi_{01})}$$
$$+ \frac{\sqrt{G_1}}{\sqrt{2}}E_A(t)e^{-(j\omega_A t+\frac{\pi}{2}+\Phi_1(t)+\phi_{01})} \quad (2.36)$$

$$E_L(t) = \sqrt{G_2}e^{-j(\Phi_2(t)+\phi_{02})}E_H(t)$$
$$= \frac{\sqrt{G_2}}{2}E_B(t)e^{-j(\omega_B t+\frac{\pi}{2}+\Phi_2(t)+\phi_{02})} + \frac{\sqrt{G_2}}{2}E_C(t)e^{-j(\omega_C t+\Phi_2(t)+\phi_{02})}$$
$$+ \frac{\sqrt{G_2}}{\sqrt{2}}E_D(t)e^{-(j\omega_D t+\frac{\pi}{2}+\Phi_2(t)+\phi_{02})} \quad (2.37)$$

Finally, the signals with electric fields E_K and E_L are divided in equal parts and recombined by the SOA-MZI output coupler C4 giving the following expressions for the output SOA-MZI electric fields at ports I and J, respectively:

$$E_I(t) = \frac{1}{\sqrt{2}}E_K(t) + \frac{1}{\sqrt{2}}E_L(t)e^{-j\frac{\pi}{2}} \quad (2.38)$$
$$E_J(t) = \frac{1}{\sqrt{2}}E_K(t)e^{-j\frac{\pi}{2}} + \frac{1}{\sqrt{2}}E_L(t) \quad (2.39)$$

Using the expression of Equation (2.36) for E_K and of Equation (2.37) for E_L, the expression

for E_I becomes:

$$E_I(t) = \frac{\sqrt{G_1}}{2\sqrt{2}}E_B(t)e^{-j(\omega_B t+\Phi_1(t)+\phi_{01})} - \frac{\sqrt{G_2}}{2\sqrt{2}}E_B(t)e^{-j(\omega_B t+\Phi_2(t)+\phi_{02})} + \frac{\sqrt{G_1}}{2\sqrt{2}}E_C(t)e^{-j(\omega_C t+\frac{\pi}{2}+\Phi_1(t)+\phi_{01})} + \frac{\sqrt{G_2}}{2\sqrt{2}}E_C(t)e^{-j(\omega_C t+\frac{\pi}{2}\Phi_2(t)+\phi_{02})} + \frac{\sqrt{G_1}}{2}E_A(t)e^{-(j\omega_A t+\frac{\pi}{2}+\Phi_1(t)+\phi_{01})} - \frac{\sqrt{G_2}}{2}E_D(t)e^{-(j\omega_D t+\Phi_2(t)+\phi_{02})} \quad (2.40)$$

Similarly, using the expression of Equation (2.36) for E_K and of Equation (2.37) for E_L, the expression for E_J becomes:

$$E_J(t) = \frac{\sqrt{G_1}}{2\sqrt{2}}E_B(t)e^{-j(\omega_B t+\frac{\pi}{2}+\Phi_1(t)+\phi_{01})} - \frac{\sqrt{G_2}}{2\sqrt{2}}E_B(t)e^{-j(\omega_B t+\frac{\pi}{2}+\Phi_2(t)+\phi_{02})} - \frac{\sqrt{G_1}}{2\sqrt{2}}E_C(t)e^{-j(\omega_C t+\Phi_1(t)+\phi_{01})} + \frac{\sqrt{G_2}}{2\sqrt{2}}E_C(t)e^{-j(\omega_C t+\Phi_2(t)+\phi_{02})} + \frac{\sqrt{G_1}}{2} - E_A(t)e^{-(j\omega_A t+\Phi_1(t)+\phi_{01})} - \frac{\sqrt{G_2}}{2}E_D(t)e^{-(j\omega_D t+\frac{\pi}{2}+\Phi_2(t)+\phi_{02})} \quad (2.41)$$

In the experimental part of this thesis, there is no signal at ports B and D, so that E_B and E_D are equal to zero. In this case, the expressions for E_I and for E_J become:

$$E_I(t) = \frac{\sqrt{G_1}}{2\sqrt{2}}E_C(t)e^{-j(\omega_C t+\frac{\pi}{2}+\Phi_1(t)+\phi_{01})} + \frac{\sqrt{G_2}}{2\sqrt{2}}E_C(t)e^{-j(\omega_C t+\frac{\pi}{2}+\Phi_2(t)+\phi_{02})} + \frac{\sqrt{G_1}}{2}E_A(t)e^{-j(\omega_A t+\frac{\pi}{2}+\Phi_1(t)+\phi_{01})} \quad (2.42)$$

$$E_J(t) = -\frac{\sqrt{G_1}}{2\sqrt{2}}E_C(t)e^{-j(\omega_C t+\Phi_1(t)+\phi_{01})} + \frac{\sqrt{G_2}}{2\sqrt{2}}E_C(t)e^{-j(\omega_C t+\Phi_2(t)+\phi_{02})} - \frac{\sqrt{G_1}}{2}E_A(t)e^{-j(\omega_A t+\Phi_1(t)+\phi_{01})} \quad (2.43)$$

As the signals at ports A and C are at wavelengths λ_A and λ_C, respectively, in I and J output ports of SOA-MZI signals at these different wavelengths are present. The output signal at wavelength λ_A is the amplified and phase shifted version of the input signal at port A. The output signal at wavelength λ_C is the real product of SOA-MZI interferometric module. As a result, in order to filter out the output signal at λ_A, an optical filter will be used in the

experimental part. The electric fields E_I and E_J at λ_A are given by:

$$E_I(t) = \frac{\sqrt{G_1}}{2} E_A(t) e^{-j(\omega_A t + \frac{\pi}{2} + \Phi_1(t) + \phi_{01})} \tag{2.44}$$

$$E_J(t) = -\frac{\sqrt{G_1}}{2} E_A(t) e^{-j(\omega_A t + \Phi_1(t) + \phi_{01})} \tag{2.45}$$

The electric fields E_I and E_J at λ_C are given by:

$$E_I(t) = \frac{\sqrt{G_1}}{2\sqrt{2}} E_C(t) e^{-j(\omega_C t + \frac{\pi}{2} + \Phi_1(t) + \phi_{01}))} + \frac{\sqrt{G_2}}{2\sqrt{2}} E_C(t) e^{-j(\omega_C t + \frac{\pi}{2} + \Phi_2(t) + \phi_{02}))} \tag{2.46}$$

$$E_J(t) = -\frac{\sqrt{G_1}}{2\sqrt{2}} E_C(t) e^{-j(\omega_C t + \Phi_1(t) + \phi_{01}))} + \frac{\sqrt{G_2}}{2\sqrt{2}} E_C(t) e^{-j(\omega_C t + \Phi_2(t) + \phi_{02}))} \tag{2.47}$$

Since the relation between the power and the amplitude of electric field is $P(t) = E(t) \cdot E^*(t)$, where the amplitude of the electric field E is normalized [18], the power at output ports I and J of SOA-MZI is given by Equation (2.48) and (2.49), respectively:

$$P_I(t) = \frac{1}{8} P_C(t) \left[G_1(t) + G_2(t) + 2\sqrt{G_1(t) G_2(t)} \cos(\Delta\Phi(t)) \right] \tag{2.48}$$

$$P_J(t) = \frac{1}{8} P_C(t) \left[G_1(t) + G_2(t) - 2\sqrt{G_1(t) G_2(t)} \cos(\Delta\Phi(t)) \right] \tag{2.49}$$

where $\Delta\Phi(t) = \phi_{01} - \phi_{02} + \Phi_1(t) - \Phi_2(t) = \Delta\phi_0 + \Phi_1(t) - \Phi_2(t)$ is the phase difference created both due to the SOAs nonlinearities, and due to the relative static phase shift between the copies of the input signal at port C, traveling on the upper and the lower arm of the SOA-MZI.

2.4.3 Static characterization of SOA-MZI switch

2.4.3.1 Theoretical static characteristic

Two states are possible for the SOA-MZI when it is used as a switch, and the phases of the SOA-MZI arms are properly adjusted by ϕ_{01} and ϕ_{02} phase shifters. These states are named cross and bar state. Ideally, in the case of cross state, where there is no control signal A, the signal C is amplified and exits from SOA-MZI port I while $P_J = 0$. Also, in the case of bar state, where there is a control signal A of suitable power such that it induces a nonlinear phase shift of π in SOA1, the signal C is amplified and exits from SOA-MZI port J while $P_I = 0$. In this framework, and for a static configuration, where $P_C(t) = \overline{P}_C$ and $P_A(t) = \overline{P}_A$, we are going to express the Equations (2.48) and (2.49) for the bar and cross states. In the case of the bar state, $\overline{P}_A = 0$, the phase difference $\Delta\overline{\Phi} = 0$ and the gain in the two SOAs is the same and equal to

the unsaturated value of gain, G_0. Thus, the Equations (2.48) and (2.49) are transformed into:

$$P_{I,bar} = \frac{1}{8}\overline{P}_C \left[G_0 + G_0 + 2\sqrt{G_0 G_0}\right] = \frac{1}{2} G_0 \overline{P}_C \tag{2.50}$$

$$P_{J,bar} = \frac{1}{8}\overline{P}_C \left[G_0 + G_0 - 2\sqrt{G_0 G_0}\right] = 0 \tag{2.51}$$

In the case of the cross state, the control signal $\overline{P}_A$ is non zero, $\Delta\overline{\Phi} = \pi$ and the gain of the two SOAs are different due to the saturation of SOA1 by $\overline{P}_A$, meaning that $\overline{G}_1 < G_0$. Thus, the Equations (2.48) and (2.49) are transformed into:

$$\begin{aligned} P_{I,cross} = \frac{1}{8}\overline{P}_C \left[\overline{G}_1 + G_0 - 2\sqrt{\overline{G}_1 G_0}\right] &= \frac{1}{8}\overline{P}_C \cdot G_0 \left[1 + \frac{\overline{G}_1}{G_0} - 2\sqrt{\frac{\overline{G}_1}{G_0}}\right] \\ &= \frac{1}{8}\overline{P}_C \cdot G_0 \left[\sqrt{\frac{\overline{G}_1}{G_0}} - 1\right]^2 \end{aligned} \tag{2.52}$$

$$\begin{aligned} P_{J,cross} = \frac{1}{8}\overline{P}_C \left[\overline{G}_1 + G_0 + 2\sqrt{\overline{G}_1 G_0}\right] &= \frac{1}{8}\overline{P}_C \cdot G_0 \left[1 + \frac{\overline{G}_1}{G_0} + 2\sqrt{\frac{\overline{G}_1}{G_0}}\right] \\ &= \frac{1}{8}\overline{P}_C \cdot G_0 \left[\sqrt{\frac{\overline{G}_1}{G_0}} + 1\right]^2 \end{aligned} \tag{2.53}$$

A deviation from the ideal behavior of a switch can be observer as $P_{J,bar}$ is not equal to zero, and thus $P_{J,cross} \neq P_{I,bar}$. The symmetric operation of the SOA-MZI switch is disrupted. Another deviation from the ideal which is not shown explicitly in this analysis is the fact that at SOA-MZI output port I and J, there is an amount of P_{ASE} produced by the SOAs. As a result, in practical applications $P_{J,bar}$ can not be zero as well. An important metric in the static regime, in order to quantify the quality of the switching operation in an SOA-MZI, is the Extinction Ratio (ER), which for port J and I is given, respectively, by:

$$ER_J(dB) = 10 \cdot log\left(\frac{P_{J,bar} + P_{ASE}}{P_{J,cross}}\right) = 10 \cdot log\left(\frac{8P_{ASE}}{\overline{P}_C \cdot G_0 \left[\sqrt{\frac{\overline{G}_1}{G_0}} + 1\right]^2}\right) \tag{2.54}$$

$$ER_I(dB) = 10 \cdot log\left(\frac{P_{I,cross} + P_{ASE}}{P_{I,bar}}\right) = 10 \cdot log\left(\frac{\overline{P}_C \cdot G_0\left[\sqrt{\frac{G_1}{G_0}} - 1\right]^2 + 8P_{ASE}}{4G_0\overline{P}_C}\right) \quad (2.55)$$

In the above ER Equations, the ASE noise is omitted for $P_{J,cross}$ and for $P_{I,bar}$, as it is negligible in comparison to them, whereas it has been added for $P_{J,bar}$ and for $P_{I,cross}$ because it is comparable to them.

2.4.3.2 Experimental static characteristic

A static characterization experimental setup shown in Figure 2.11 is employed in order to measure the ER of the SOA-MZI module (CIP 40G-2R2-ORP). A CW tunable laser source is

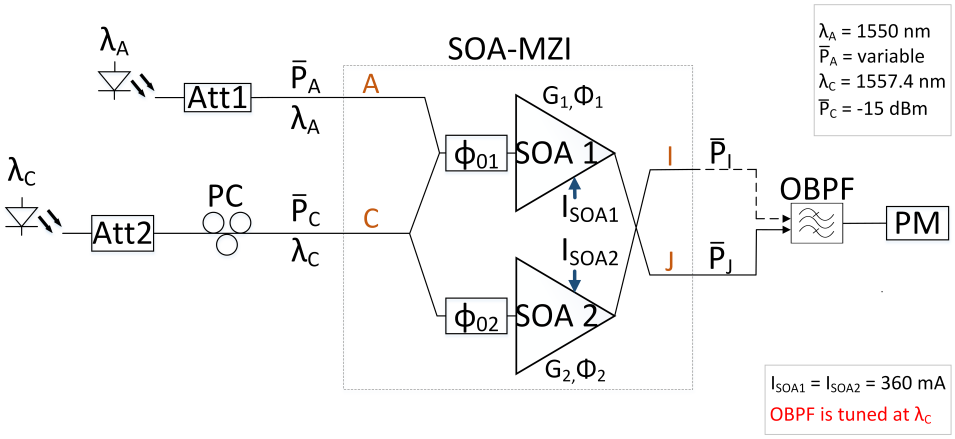

Figure 2.11: Experimental setup for the static characteristic of the SOA-MZI. Att: Attenuator. PC: Polarization Controller. OBPF: Optical Band-Pass Filter. PM: Optical Power Meter.

configured to emit at wavelength $\lambda_C = 1557.4$ nm and subsequently its optical mean power is adjusted by attenuator Att2 so that we have $P_C(t) = \overline{P}_C = -15$ dBm at input C. The SOA currents are symmetric and $I_{SOA1} = I_{SOA2} = 360$ mA. The phase-shifters ϕ_{01} and ϕ_{02} in the two arms of the SOA-MZI and the polarization controller (PC) placed in the path of port C are adjusted so that the optical power at output port J is minimum when there is no power at input port A. After the aforementioned adjustments, the additional modification of the I_{SOA2} value does not provide any further decrease of the minimum, and thus the SOA currents are kept symmetric.

Another CW tunable laser source is configured to emit at wavelength $\lambda_A = 1550$ nm and subsequently its optical mean power is adjusted by attenuator Att1 so that we can sweep $P_A(t) = \overline{P}_A$ in the range from -40 dBm to +10 dBm.

At the SOA-MZI outputs I and J, an OBPF is used to filter out the signal around λ_A. Finally, the powers at ports I and J are measured utilizing a Power Meter (PM). The results of this static characterization are depicted in Figure 2.12. The powers of port I and J in Figure 2.12 correspond to $P_I(t) = \overline{P}_I$ and $P_J(t) = \overline{P}_J$, directly at the output of the SOA-MZI, as we have taken into account the losses of OBPF to the PM results.

As discussed in subsection 2.4.3 and specifically from Equations (2.55) and (2.54), it becomes clear that ER_J and ER_I have different values. Indeed, in the specific example of Figure 2.12, ER_J and ER_I the difference is almost 10 dB.

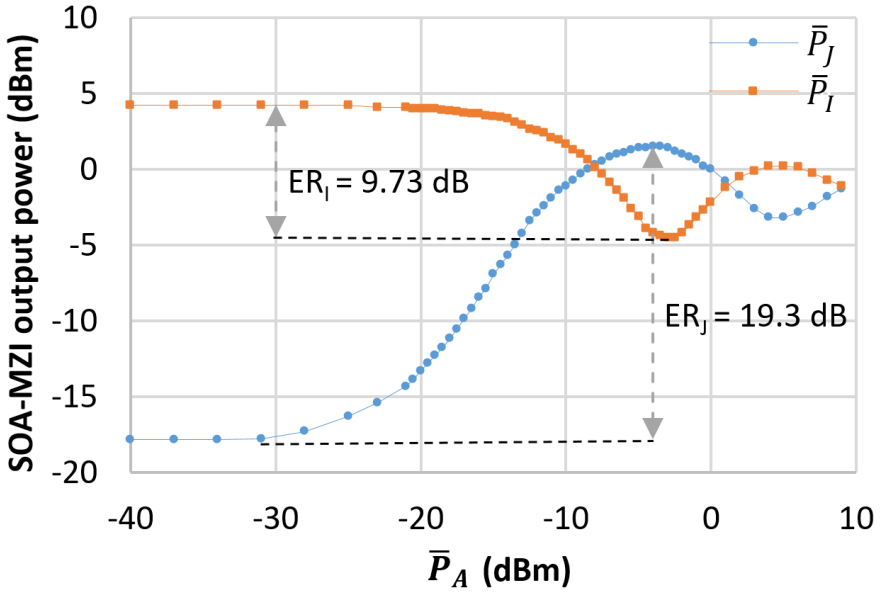

Figure 2.12: Static characteristic and extinction ratio of both output ports of the SOA-MZI.

2.4.4 Dynamic characterization of SOA-MZI switch

2.4.4.1 Theoretical dynamic characteristic

An important parameter that determines the SOA-MZI behavior in general and as a sampler in particular is its 3 dB XPM bandwidth. The XPM bandwidth is a dynamic characteristic of the SOA-MZI that can be measured when P_C is a static or Continuous Wave (CW) optical power, whereas P_A is a CW superimposed by a sinusoidal signal, whose frequency is swept into a range of frequencies and the transfer function as a function of the frequency is obtained. The 3 dB XPM bandwidth defines the frequency range of signals entering from port A for which the SOA-MZI performance is optimum.

A rigorous theoretical analysis based in a SOA-MZI small-signal model has been presented in [22, 26]. The conversion efficiency at the output J of the SOA-MZI, η, is defined as the ratio

Table 2.1: Parameters used in the analysis

Parameter	Value	Units
α_{int}	$\alpha_{int} \ll \Gamma g_m$ [22, 26]	cm^{-1}
α_H	4	
L	1.5	mm
$\Gamma g_m L$	1-9 [22, 26]	
τ_{eff}	25 and 50 [22]	ps
$\frac{\tau_s}{\tau_{eff}}$	4 [22]	
ϕ_0	$\phi_0 \approx 0$ [22, 26]	rad

of the output power variation at port J, δp_J, to the input power variation at control port A, δp_A, given by [22, 26]:

$$\eta(\omega) = \frac{\delta p_J}{\delta p_A} = [1 - \cos(\phi_0)] \left| \left[e^{\frac{-\Gamma g_m L}{\tau_s \left(1/\tau_{eff} + j\omega\right)}} - 1 \right] + \gamma \frac{\Gamma g_m}{\tau_s \left(1/\tau_{eff} + j\omega\right)} \cdot \left[(\Gamma g_m - \alpha_{int}) - \frac{\Gamma g_m}{\tau_s \left(1/\tau_{eff} + j\omega\right)} \right]^{-1} \cdot e^{\frac{-\Gamma g_m L}{\tau_s \left(1/\tau_{eff} + j\omega\right)}} \right| \quad (2.56)$$

where τ_{eff} is the effective carrier lifetime, τ_s is the stimulated carrier recombination time and γ is the bandwidth enhancement factor given by:

$$\gamma = \frac{\alpha_H \cdot sin(\phi_0)}{1 - \cos(\phi_0)} \quad (2.57)$$

In this small-signal analysis, despite the fact that the SOA-MZI frequency response does not take into account the ASE, it could be taken into account by adding an additional carrier recovery time constant $\tau_{s,ASE}$.

The conversion efficiency in dB, normalized with respect to the efficiency at a frequency equal to zero, is given by:

$$\eta_{norm} = 20 \cdot log \left(\frac{\eta(\omega)}{\eta(0)} \right) \quad (2.58)$$

It should be noted that in Equation (2.58) the logarithm coefficient for the normalized frequency is 20 as it is calculated in the electronic domain after photodetection, whereas in [22], the logarithm coefficient is 10 as it is calculated in the optical domain.

Figures 2.13 and 2.14 depict the normalized conversion efficiency as a function of the frequency for different total gain factors ($\Gamma g_m L$) and for effective carrier lifetimes, τ_{eff}, equal to 25 ps and to 50 ps, respectively, assuming that $\tau_s/\tau_{eff} = 4$. α_{int} is considered insignificant com-

Table 2.2: Correspondence between $\Gamma g_m L$ and SOA Gain using Equation (2.59)

$\Gamma g_m L$	**SOA Gain (dB)**
1	4
3	13
5	21.7
7	30.4
9	39.1

Table 2.3: XPM Bandwidth

τ_{eff} **(ps)**	$\Gamma g_m L$	**XPM Bandwidth (GHz)**
25	1	5.9
»	3	10.7
»	5	20.6
»	7	20.5
»	9	21.5
50	1	2.9
»	3	5.4
»	5	10.2
»	7	10.1
»	9	10.8

pared to Γg_m for simplicity reasons. All values are the same as the ones used in [22] except for α_H where a lower and more common value is used (4 compared to 6) and for L where a higher value is used (1.5 mm to 1 mm), typical for long SOA devices as the ones used experimentally. All parameters used in this calculation are shown in Table 2.1.

Assuming that $\alpha_{int} \ll \Gamma g_m$ an approximation of the SOA Gain, G_{dB}, can be given for a known value of $\Gamma g_m L$ using Equation (2.30):

$$G_{dB} = 10\,log\left(e^{(\Gamma g_m - \alpha_{int})L}\right) \approx 10\,log\left(e^{\Gamma g_m L}\right) \tag{2.59}$$

The correspondence between $\Gamma g_m L$ and G_{dB} values is shown in Table 2.2.

The 3 dB XPM bandwidth is defined as the width of the frequency range where the conversion efficiency is at most 3 dB below its maximum value.

The frequency response of the conversion efficiency in Figure 2.13 has the shape of a first order low pass filter for $\Gamma g_m L = 1$, 3 and 5, whereas a resonant overshooting appears roughly

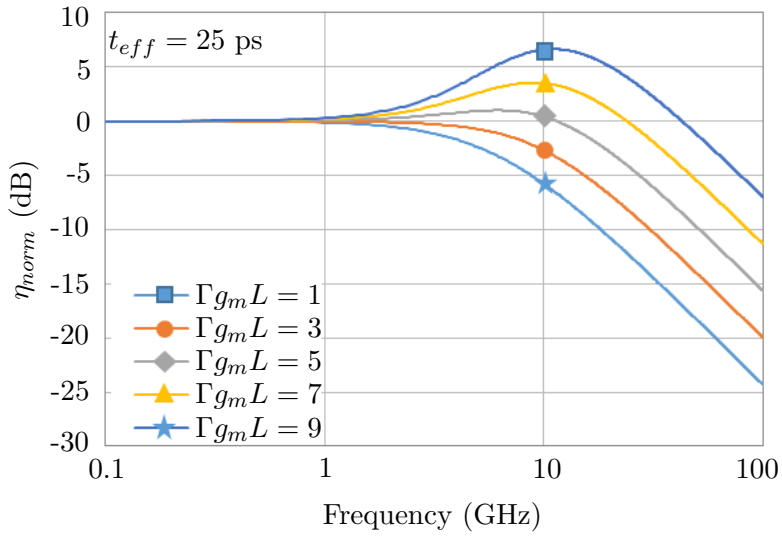

Figure 2.13: Normalized frequency response of the SOA-MZI for effective carrier lifetime τ_{eff} = 25 ps with different total gain factors.

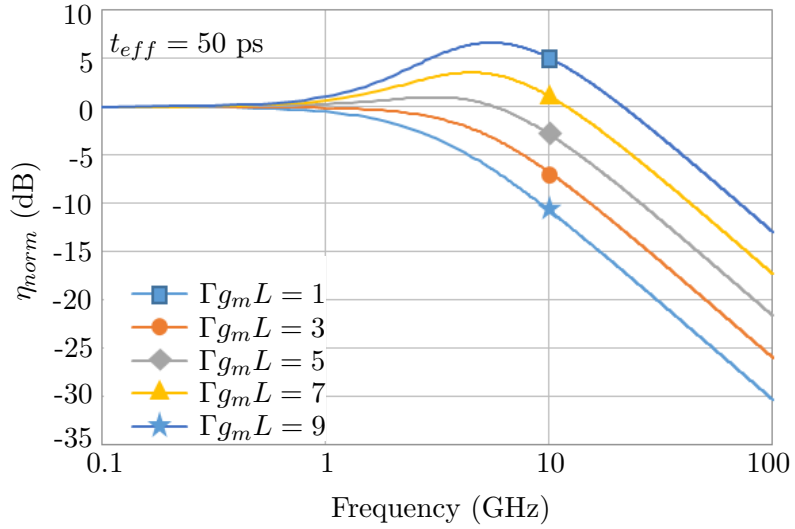

Figure 2.14: Normalized frequency response of the SOA-MZI for effective carrier lifetime τ_{eff} = 50 ps with different total gain factors.

around 10 GHz for $\Gamma g_m L = 7$ and 9. The frequency response of the conversion efficiency in Figure 2.14 has once more a first order low pass filter behavior for $\Gamma g_m L = 1$, 3 and 5, whereas a resonant overshooting appears roughly around 6 GHz for $\Gamma g_m L = 7$ and 9. Comparing Figures 2.13 and 2.14, it can be observed that an increase of τ_{eff} from 25 ps to 50 ps while preserving

the ratio $\tau_s/\tau_{eff} = 4$, causes the resonant overshooting to be displaced 4 GHz towards the lower frequencies.

Table 2.3 shows the 3 dB XPM bandwidth for all cases of Figures 2.13 and 2.14. It can be observed that the 3 dB bandwidth is lower for $\tau_{eff} = 50$ ps than for $\tau_{eff} = 25$ ps for the same gain factor. Moreover, another point is that for the same τ_{eff}, the increase of the gain factor, $\Gamma g_m L$, causes an increase of the 3 dB bandwidth, except for the case between the $\Gamma g_m L = 5$ and $\Gamma g_m L = 7$, where the 3 dB bandwidth decreases by 0.1 dB.

According to the above analysis, it is concluded that the combination of the two key parameters $\Gamma g_m L$ and τ_{eff} determines the XPM bandwidth of the SOA-MZI module, which is of great importance for the performance of the SOA-MZI photonic sampler. SOA-MZI modules which employ SOAs with high $\Gamma g_m L$ and low τ_{eff} values will have a very high XPM SOA-MZI bandwidth and permit either a very high sampling rate or a very high bandwidth of the signal to be sampled depending on the architecture employed. The two architectures of the SOA-MZI photonic sampler are presented in chapter 3.

2.4.4.2 Experimental dynamic characteristic

A pump-probe configuration, shown in Figure 2.15, is used to measure the XPM bandwidth for different average optical powers and wavelengths launched at the SOA-MZI inputs.

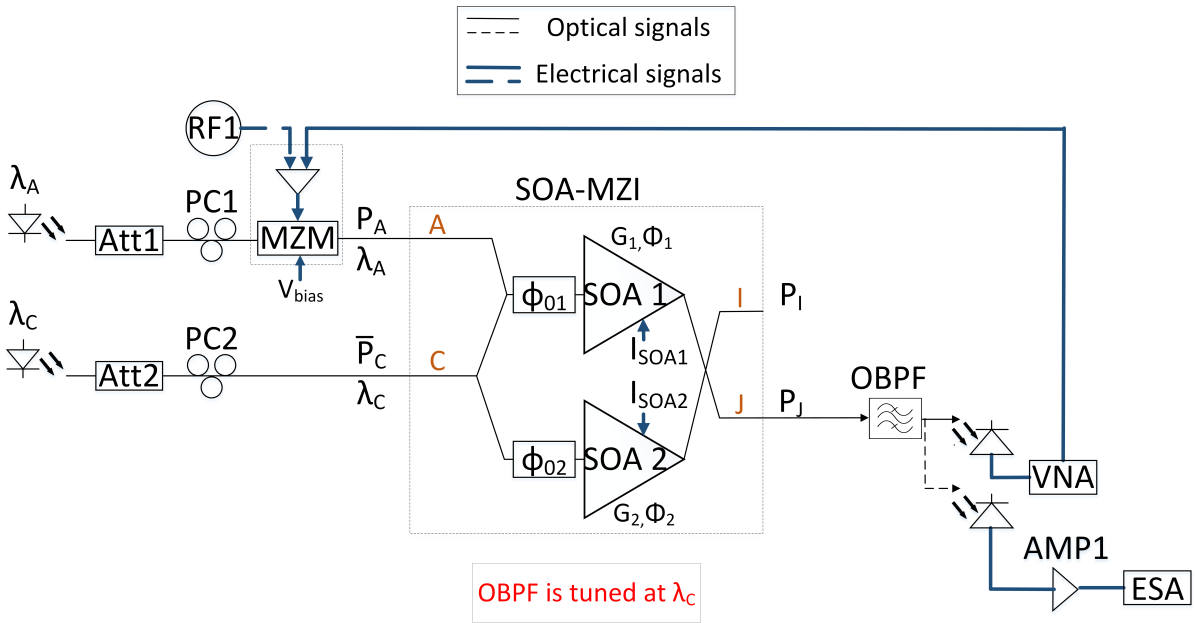

Figure 2.15: Pump-probe experimental setup for the XPM bandwidth measurement. RF: Radio Frequency generator. MZM: Mach-Zehnder Modulator. VNA: Anritsu MS2026C Network Analyzer. AMP: Electrical Amplifier. ESA: Electrical Spectrum Analyzer.

The generation and adjustment of the signal at input C is performed in the same way as for the static characteristic in 2.4.3.2. A CW tunable laser source is configured to emit at wavelength λ_C and subsequently its optical mean power is adjusted by attenuator Att2 so that we have $\overline{P}_C$ at input C. Moreover, the phase-shifters ϕ_{01} and ϕ_{02} in the two arms of the SOA-MZI and the polarization controller (PC2) placed in the path of port C are adjusted, so that the optical power at output port J is minimum when there is no power at input port A.

Another CW tunable laser source is configured to emit at wavelength λ_C and subsequently its optical mean power is adjusted by attenuator Att1 so that we have $\overline{P}_A$ at input A.

The parameter combinations of λ_A, λ_C, $\overline{P}_A$ and $\overline{P}_C$ measured, are given in Table 2.4.

The results of Figure 2.16 and the results for the rest of wavelength and power combinations of Table 2.4 are obtained by a slightly different experimental setup. For the results of Figure 2.16, the optical power P_A is intensity modulated by iXblue MXAN-LN-40 MZM, which is driven by Anritsu MS2026C VNA through the iXblue DR-AN-40-MO MZM driver module. The MZM is biased in the quadrature point with $V_{bias} = 3$ V. The MZM driver module provides 26 dB gain at the RF input of MZM. At the SOA-MZI J output, P_J is optically filtered in order to discard the optical carrier at λ_A. Afterwards, the optically filtered output enters the calibrated photodiode Anritsu MN4665B and subsequently is directed to the electrical port of Anritsu MS2026C VNA. For the results of the rest of wavelength and power combinations of Table 2.4, the optical power P_A is intensity modulated by the MZM, which is driven by an RF generator through the driver module. The electrical power at the output of the RF generator is adjusted at -25 dBm for all measured frequencies. At the SOA-MZI J output, P_J is optically filtered in order to discard the optical carrier λ_A. Afterwards, the optically filtered output is converted to the electrical domain by a photodiode, amplified and measured by an ESA. The experimental measurements were fitted to a first order low-pass filter curve to calculate the 3 dB electrical bandwidth given in Table 2.4.

The form of the experimental result obtained in Figure 2.16 does not present any resonant overshooting and, as such, is qualitatively in the same category with cases $\Gamma g_m L = 1$, 3 and 5 in Figure 2.13 and in Figure 2.14, in which cases no resonant overshooting appears as well.

The significance of the results cited in this Table 2.4 and depicted in Figure 2.16 is that they allow to specify the range of variation of the bandwidth of the XPM phenomenon, which is exploited in the considered SOA-MZI module and hence is critical for their operation and performance. Since there is no significant benefit in choosing a high power, lower average powers can be chosen for the two inputs so as to minimize the power supply requirements.

Table 2.4: XPM frequency conversion response of CIP 40G-2R2-ORP for different operating points.

λ_A (nm)	λ_C (nm)	$\overline{P}_A$ (dBm)	$\overline{P}_C$ (dBm)	XPM Bandwidth (GHz)
1550	1557	0	0	5.6 [Figure 2.16]
»	»	-15	0	5.6
»	»	0	-18	5.9
»	»	-15	-18	5

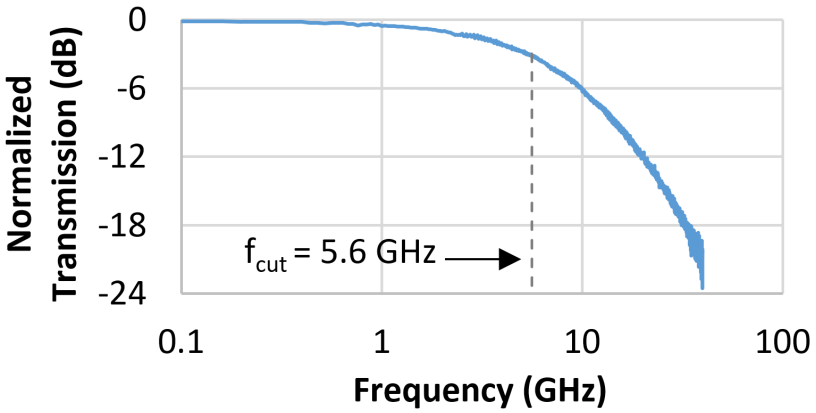

Figure 2.16: SOA-MZI XPM normalized frequency response. The normalized transmission is defined as the electrical power of the signal at the SOA-MZI output normalized to the electrical power at 0.1 GHz.

2.5 Conclusion

General information and important parameters about optical sampling in general were specified. In addition, the principle of operation of more advanced systems were explained in detail, where the photonic sampler can be used as a building block, such as the ADC and the photonic sampler mixers. Moreover, essential information and critical parameters of the SOA are identified. The phenomena of the SOA are concisely presented with XPM being the non-linear phenomenon exploited by the SOA-MZI module. Furthermore, the model of the SOA-MZI were demonstrated, which is used in the following chapters. Last but not least, a theoretical performance analysis of the static and dynamic characteristics of the SOA-MZI in general, as well as the experimental static and dynamic characteristics of the SOA-MZI used in this thesis were illustrated. In the theoretical analysis, the metric of ER was evaluated and found equal to 19.3 dB and 9.73 dB at

SOA-MZI ports J and I, respectively. Moreover, the XPM bandwidth of the SOA-MZI module was evaluated for different wavelength and power combinations and found between 5-5.9 GHz for all the cases examined.

References

[1] W. Kester, "Aperture Time, Aperture Jitter, Aperture Delay Time— Removing the Confusion," Analog devices, Tech. Rep., Jan. 2008. [Online]. Available: https://www.analog.com/media/en/training-seminars/tutorials/MT-007.pdf

[2] J. Kim and F. Kärtner, "Attosecond-precision ultrafast photonics," *Laser & Photonics Reviews*, vol. 4, no. 3, pp. 432–456, Apr. 2010.

[3] R. Hui, "Photodetectors," in *Introduction to Fiber-Optic Communications*. Cambridge, MA, USA: Elsevier, 2020, pp. 125–154.

[4] R. Walden, "Analog-to-digital converter survey and analysis," *IEEE Journal on Selected Areas in Communications*, vol. 17, no. 4, pp. 539–550, Apr. 1999.

[5] R. Vaughan, N. Scott, and D. White, "The theory of bandpass sampling," *IEEE Transactions on Signal Processing*, vol. 39, no. 9, pp. 1973–1984, Sep. 1991.

[6] Y. Liu, L. Chen, T. Xu, J. Mao, S. Zhang, and Y. Liu, "All-optical signal processing based on semiconductor optical amplifiers," *Frontiers of Optoelectronics in China*, vol. 4, no. 3, pp. 231–242, Sep. 2011.

[7] B. Dagens, A. Labrousse, R. Brenot, B. Lavigne, and M. Renaud, "SOA-based devices for all-optical signal processing," in *Proc. OFC 2003 Optical Fiber Communications Conference, 2003.*, Mar. 2003, pp. 582–583 vol.2.

[8] C. Bohémond, T. Rampone, and A. Sharaiha, "Performances of a Photonic Microwave Mixer Based on Cross-Gain Modulation in a Semiconductor Optical Amplifier," *Journal of Lightwave Technology*, vol. 29, no. 16, pp. 2402–2409, Aug. 2011.

[9] S. Bischoff, M. Nielsen, and J. Mork, "Improving the all-optical response of SOAs using a modulated holding signal," *Journal of Lightwave Technology*, vol. 22, no. 5, pp. 1303–1308, May 2004.

[10] S. Nakamura, Y. Ueno, K. Tajima, J. Sasaki, T. Sugimoto, T. Kato, T. Shimoda, M. Itoh, H. Hatakeyama, T. Tamanuki, and T. Sasaki, "Demultiplexing of 168-Gb/s data pulses with a hybrid-integrated symmetric Mach-Zehnder all-optical switch," *IEEE Photonics Technology Letters*, vol. 12, no. 4, pp. 425–427, Apr. 2000.

[11] R. J. Manning, A. D. Ellis, A. J. Poustie, and K. J. Blow, "Semiconductor laser amplifiers for ultrafast all-optical signal processing," *Journal of the Optical Society of America B*, vol. 14, no. 11, p. 3204, Nov. 1997.

[12] M. Osinski and J. Buus, "Linewidth broadening factor in semiconductor lasers–An overview," *IEEE Journal of Quantum Electronics*, vol. 23, no. 1, pp. 9–29, Jan. 1987.

[13] M. J. Connelly, "Semiconductor Optical Amplifiers and their Applications," in *Proc. 3rd Spanish Meeting of Optoelectronics, OPTOEL'03*, Aug. 2003.

[14] M. J. Connelly, *Semiconductor Optical Amplifiers*, 1st ed. Boston, MA, USA: Kluwer Academic Publishers, 2004.

[15] *Preliminary Datasheet SOA-NL-1550 -1.55μm Non-Linear Optical Amplifier (SOA)*, CIP technologies, Ipswich, UK, 2014.

[16] G. P. Agrawal, *Fiber-Optic Communication Systems*. Wiley-Interscience, 2002.

[17] S. Mazzucato, H. Carrère, X. Marie, T. Amand, M. Achouche, C. Caillaud, and R. Brenot, "Gain, amplified spontaneous emission and noise figure of bulk InGaAs/InGaAsP/InP semiconductor optical amplifiers," *IET Optoelectronics*, vol. 9, no. 2, pp. 52–60, Apr. 2015.

[18] G. Agrawal and N. Olsson, "Self-phase modulation and spectral broadening of optical pulses in semiconductor laser amplifiers," *IEEE Journal of Quantum Electronics*, vol. 25, no. 11, pp. 2297–2306, Nov. 1989.

[19] A. Borghesani, N. Fensom, A. Scott, G. Crow, L. Johnston, J. King, L. Rivers, S. Cole, S. Perrin, D. Scrase, G. Bonfrate, A. Ellis, I. Lealman, G. Crouzel, L. H. K. Chun, A. Lupu, E. Mahe, and P. Maigne, "High Saturation Power (>16.5dBm) and Low Noise Figure (<6dB) Semiconductor Optical Amplifier for C-band Operation," in *Proc. Optical Fiber Communication Conference (2003), Paper ThO1*. Optical Society of America, Mar. 2003, p. ThO1.

[20] P. P. Baveja, A. M. Kaplan, D. N. Maywar, and G. P. Agrawal, "Pulse amplification in semiconductor optical amplifiers with ultrafast gain-recovery times," in *Proc. Optical Components and Materials VII*, vol. 7598. International Society for Optics and Photonics, Feb. 2010, p. 759817.

[21] C. Bohémond, T. Rampone, and A. Sharaiha, "Performances of a Photonic Microwave Mixer Based on Cross-Gain Modulation in a Semiconductor Optical Amplifier," *Journal of Lightwave Technology*, vol. 29, no. 16, pp. 2402–2409, Aug. 2011.

[22] M. Spyropoulou, N. Pleros, and A. Miliou, "SOA-MZI-Based Nonlinear Optical Signal Processing: A Frequency Domain Transfer Function for Wavelength Conversion, Clock Recovery, and Packet Envelope Detection," *IEEE Journal of Quantum Electronics*, vol. 47, no. 1, pp. 40–49, Jan. 2011.

[23] H. Termos, T. Rampone, A. Sharaiha, A. Hamié, and A. Alaeddine, "All-Optical Radiofrequency Sampling Mixer Based on a Semiconductor Optical Amplifier Mach–Zehnder Interferometer Using a Standard and a Differential Configuration," *Journal of Lightwave Technology*, vol. 34, no. 20, pp. 4688–4695, Oct. 2016.

[24] S. Singh and Lovkesh, "Ultrahigh Speed Optical Signal Processing Logic Based on an SOA-MZI," *IEEE Journal of Selected Topics in Quantum Electronics*, vol. 18, no. 2, pp. 970–977, Mar. 2012.

[25] *Preliminary Datasheet 40G-2R2-ORP Twin 40G/s 2R Optical Generator*, CIP technologies, Ipswich, UK, 2014.

[26] M. Spyropoulou, N. Pleros, K. Vyrsokinos, D. Apostolopoulos, M. Bougioukos, D. Petrantonakis, A. Miliou, and H. Avramopoulos, "40 Gb/s NRZ Wavelength Conversion Using a Differentially-Biased SOA-MZI: Theory and Experiment," *Journal of Lightwave Technology*, vol. 29, no. 10, pp. 1489–1499, May 2011.

Chapter 3

Experimental characterization of the Semiconductor Optical Amplifier Mach-Zehnder Interferometer (SOA-MZI) photonic sampler

In this chapter, the sampling process with the use of the SOA-MZI photonic sampler is investigated. In this context, the two possible architectures of Switching and Modulation are presented in section 3.1. In section 3.2, experimental results in the quasi-static regime, sampling Continuous Wave (CW) signals, and in dynamic regime, sampling sinusoidal signals, and the accompanying setups are provided. Moreover, the need of a linearization method in order to improve the linearity of sampling process is made apparent. Subsequently, in section 3.3, a post-distortion linearization method is demonstrated in order to enhance the performance of the SOA-MZI sampler. Finally, section 3.4 contains the conclusions reached in this chapter. Extended parts of the content of this chapter are an adapted version of a publication, produced during this thesis work, in the open-access journal Optics Express [1] [1].

3.1 SOA-MZI sampling process

Two possible architectures of the SOA-MZI photonic sampler are possible, namely the Switching and the Modulation architectures depending on which input port the sampling MLL signal and the signal to be sampled are injected in the SOA-MZI. This seemingly insignificant modification alters significantly the behavior of SOA-MZI sampler and each one presents different advantages and disadvantages.

The Modulation architecture of SOA-MZI photonic sampler was proposed and investigated

1. The publisher of Optics Express, Optica Publishing Group, does not endorse in any way this derivative version of the article.

both theoretically and experimentally during the present thesis work [1–6] while the Switching architecture is well established from previous research [7–10].

3.1.1 Switching and Modulation architectures

In this subsection the principle of operation of both architectures is presented in detail. We inject two signals at the SOA-MZI input: the sampling pulse train signal, which consists of ultra-short continuous (clock) pulses with repetition rate f_{ck}, and the signal to be sampled, which consists of a sinusoidal signal at frequency f_{dat} superimposed on a CW signal.

3.1.1.1 Switching Architecture

Figure 3.1 illustrates the Switching architecture, in which the signal to be sampled is switched on and off by the sampling pulse train as follows. The SOA-MZI module in this case acts as a switch, hence the name Switching is given to this specific architecture. The signal to be sampled is divided at the SOA-MZI middle input port into two identical copies by a 3 dB optical coupler. At time instants at which no sampling pulse is present, the signal to be sampled is amplified by the two SOAs and exits from the upper output port. At time instants at which a sampling pulse is present, a non-linear phase shift is induced in the upper copy of the input signal due to XPM phenomenon and a portion of the signal to be sampled appears amplified at lower output port, thus resulting in the sampling of the sinusoidal signal. Provided that the peak power of the pulses causes a differential phase shift of π, the entire signal to be sampled emerges amplified at the lower output port. As we can see from the power spectrum of the sampled signal obtained after optical filtering centered at λ_C, the frequency content of the signal to be sampled is replicated from f_{dat} to $f_{cki} \pm f_{dat}$, where $f_{cki} \equiv i f_{ck}$, $i \in \mathbb{N}$.

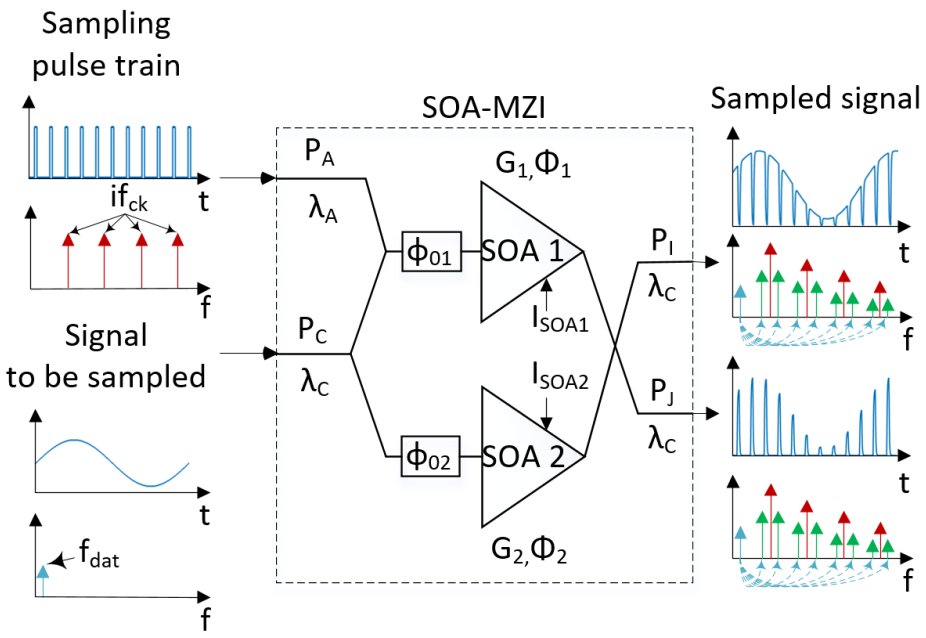

Figure 3.1: SOA-MZI Switching architecture. Reproduced from [6] (© 2020 IEEE).

Switching architecture has the disadvantage of degradation of the sampling process as the repetition rate of the pulse train, f_{ck}, increases due to the limited SOA carrier lifetime, which is reflected to the XPM bandwidth of a few GHz in 2.4.4.2. The degradation of the pulse train signal due to the limited carrier lifetime for the Switching architecture is demonstrated in Figure 3.2. In Figure 3.2 (a), the input signals $P_A(t)$ and $P_C(t)$ are illustrated. The pulse train is injected into SOA1, whereas only a CW signal is fed into SOA2. In Figure 3.2 (b), the temporal evolution of SOA1 and SOA2 gains, $G_1(t)$ and $G_2(t)$, respectively, is depicted. In presence of a pulse, a rapid gain reduction and thus gain saturation is observed in SOA1, whereas in the time period between the pulses, the gain of SOA1 recovers slowly. In Figure 3.2 (c), the temporal evolution of the SOA1 and SOA2 phases, $\Phi_1(t)$ and $\Phi_2(t)$, respectively, is shown and finally, in Figure 3.2 (d), the sampled signal at the output J of SOA-MZI, $P_J(t)$, is depicted. The sampled signal is significantly degraded due to the limited carrier lifetime of the SOA1. A technique that may be considered in order to reduce this degradation is the use of a Switching differential configuration, as in [9], which can increase the maximum repetition rate of the pulse train, by introducing a delayed copy of the pulses into SOA-MZI input D and thus into SOA2, as shown in Figure 3.3 (a). In this case, the temporal evolution of SOA2 gain and phase are delayed copies of the temporal evolution of SOA1 gain and phase, depicted in Figure 3.3 (b) and (c), respectively. Finally, this is translated to the decrease in the width of the sampled signal pulses, which is illustrated by comparing Figure 3.2 (d) and Figure 3.3 (d). The width of the sampled signal pulses is actively adjusted by the delay time between the pulse copies at input A and input

D. Nevertheless, except for the increased complexity of Switching differential configuration, the decrease in the width of the sampled signal pulses, provided by its use, does not lead to a lower harmonic distortion of the sampled signal compared to the Switching standard configuration [2], limiting significantly its potential when high quality sampling with minimum distortion is required.

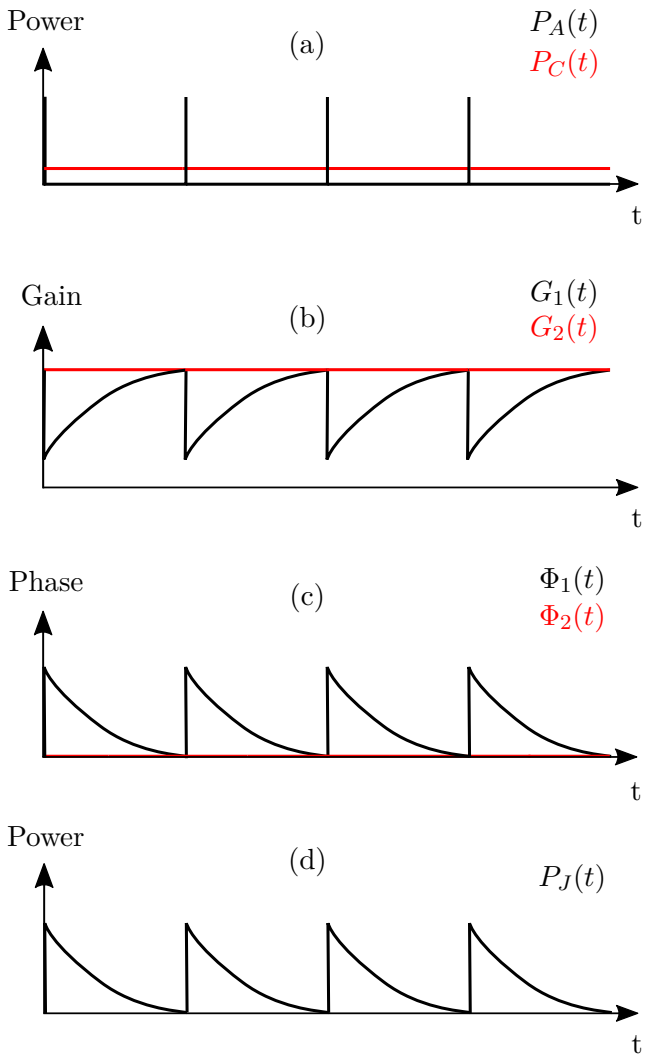

Figure 3.2: Illustrative diagrams of the degradation of the pulse train due to the limited carrier lifetime of SOA for the Switching architecture. The signals at input ports A and C, $P_A(t)$ and $P_C(t)$, respectively, are depicted in (a), the gains of SOA1, $G_1(t)$, and of SOA2, $G_2(t)$, are illustrated in (b), the non-linear phase shifts of SOA1, $\Phi_1(t)$, and of SOA2, $\Phi_2(t)$, are shown in (c) and the sampled signal at output port J, $P_J(t)$, is depicted in (d).

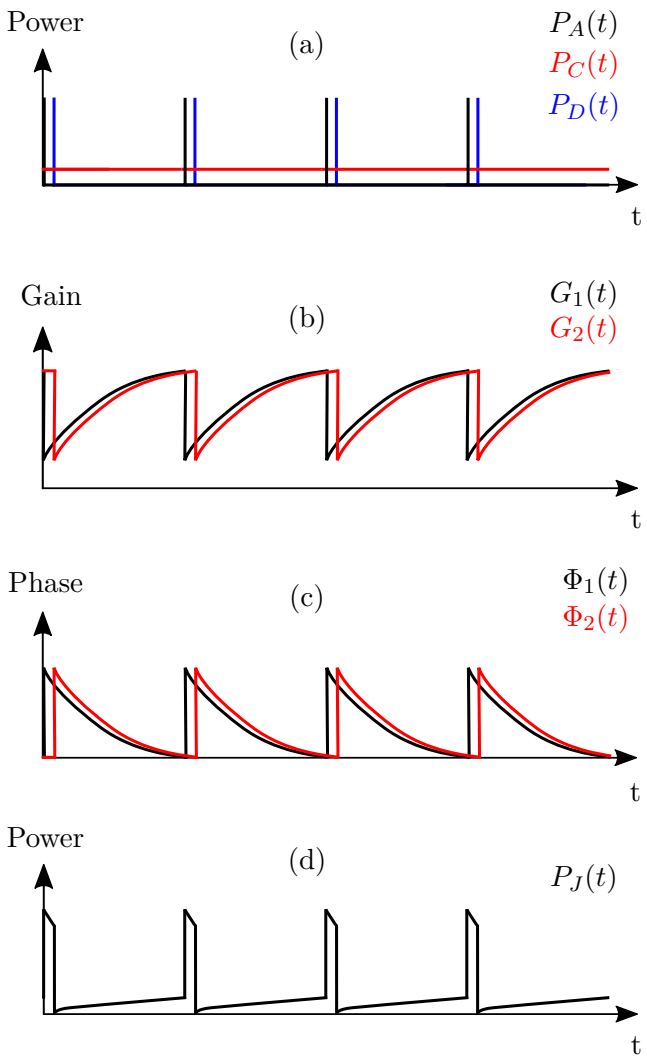

Figure 3.3: Illustrative diagrams of switching architecture with differential configuration which is employed in order to decrease the width of the sampled pulses. However, this decrease does not lead to lower harmonic distortion. The signals at input ports A, C and D, $P_A(t)$, $P_C(t)$ and $P_D(t)$, respectively, are depicted in (a), the gains of SOA1, $G_1(t)$, and of SOA2, $G_2(t)$, are illustrated in (b), the non-linear phase shifts of SOA1, $\Phi_1(t)$, and of SOA2, $\Phi_2(t)$, are shown in (c) and the sampled signal at output port J, $P_J(t)$, is depicted in (d).

3.1.1.2 Modulation Architecture

Figure 3.4 demonstrates the principle of operation for the Modulation architecture in which the sampling pulse train is modulated by the sinusoidal signal to be sampled. The SOA-MZI in this case acts as a modulator, hence the name Modulation is given to the specific architecture. More specifically, it is now the sampling pulsed signal that is divided into two identical copies by the

3 dB optical coupler at the middle input port. In this case, the signal to be sampled causes a phase shift in the upper copy of the sampling pulse train. This results in a continuous variation of the portion of the amplified sampling signal that appears at the upper and lower output, i.e. in a modulation of the sampling pulse train by the signal to be sampled. Again the frequency content of the signal power to be sampled after the optical filtering at λ_C is replicated from f_{dat} to $if_{ck} \pm f_{dat}$.

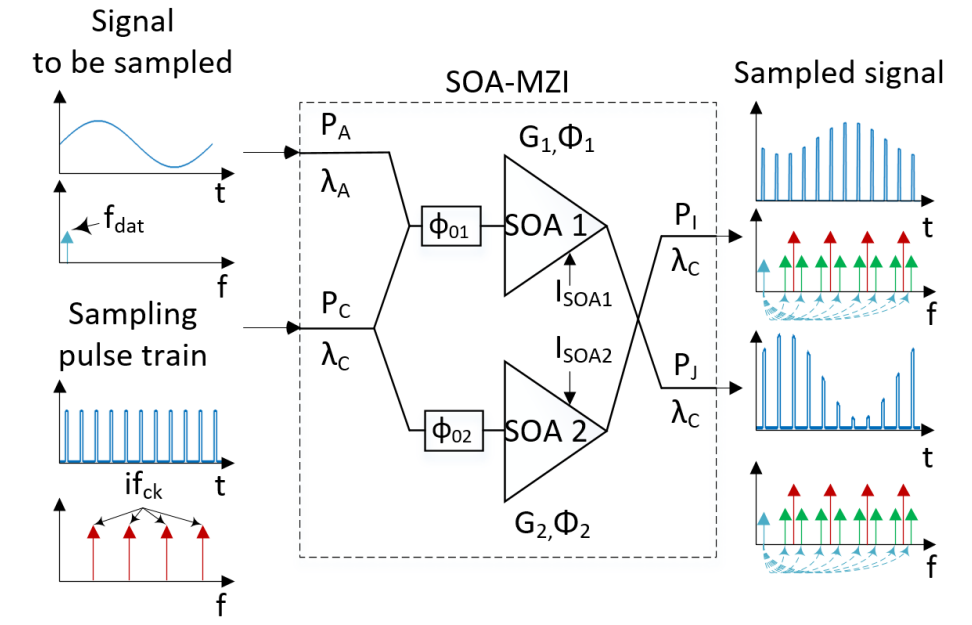

Figure 3.4: SOA-MZI Modulation architecture. Reproduced from [6] (© 2020 IEEE).

The Modulation architecture has the advantage of supporting optical pulse trains of potentially very high sampling rates, as the sampling signal with a repetition frequency f_{ck} is only amplified, so that f_{ck} can be very high due to the high optical amplification bandwidth of the SOA, despite the dynamics of the SOA carriers. On the other hand, the signal to be sampled, at the frequency f_{dat}, must be below the cut-off frequency of the XPM process, which depends on the dynamics of the SOA carriers. As a consequence, the analog bandwidth of the SOA-MZI photonic sampler is limited by the XPM bandwidth, which is between 5 GHz and 6 GHz for the specific operating conditions used in 2.4.4.2. As a result, Modulation architecture is more adapted for the case of oversampling. Furthermore, when the SOA-MZI photonic sampler is used as a photonic frequency converter, Modulation architecture is more adapted for up-conversion from band-pass or intermediate frequencies or low radio frequencies to high radio frequencies, since the frequency of the signal to be up-converted is limited by the XPM bandwidth to some GHz, whereas there is a very high upper bound for the frequency components of the sampling signal, which essentially operate as the local oscillator.

3.2 Response with pulses

3.2.1 Ultra-fast optical pulse source

The ultra-fast optical pulse source (Pritel UOC-E-05-20) which is referred as the Optical Pulse Clock (OPC) is an active mode-locked laser able to produce a train of ultra-short pulses at high pulse-repetition frequencies, nominally between 1 GHz and 20 GHz, with adequate stability and performance to be employed as the sampling source of this thesis SOA-MZI sampler. The Full Width at Half Maximum of the pulses time profile (FWHM) can be selected to be either 1.6 ps or 12.6 ps, making use of the appropriate optical filter provided by Pritel, detailed in Appendix A. In chapter 3, the FWHM of the pulses is selected to be 12.6 ps while in chapter 4, is selected to be 1.6 ps.

3.2.2 Quasi-static response

3.2.2.1 Experimental Setup

Figure 3.5 illustrates the experimental setup for conducting a quasi-static characterization of the SOA-MZI (CIP 40G-2R2-ORP) response in order to choose the average power of $P_A(t)$, $\overline{P}_A$. This type of characterization incorporates the dynamics and the behavioral changes caused to the SOA-MZI response by the utilization of optical pulses, as opposed to a pure static case. The OPC, is driven by a Radio Frequency (RF) generator at a frequency f_{ck} equal to 10 GHz and provides an optical pulse train of 12.6 ps full-width at half-maximum pulse width. The signal produced by the OPC, centered at $\lambda_C = 1557.4$ nm and having its average power adjusted by an optical attenuator to be constant at $\overline{P}_C = -15$ dBm, serves as the sampling signal that enters SOA-MZI port C. The two phase-shifters ϕ_{01} and ϕ_{02}, integrated to the SOA-MZI package, as well as the polarization controller (PC1) are tuned in such a way that the optical power at output port J is minimum when the power at input port A is zero. A CW signal tuned at $\lambda_A = 1550$ nm enters SOA-MZI port A and serves as the signal to be sampled. The average power of the pulses at outputs I and J was measured, after optical filtering centered at λ_C with a 3 dB optical bandwidth equal to 0.7 nm, using an optical power meter.

3.2.2.2 Experimental results

Figure 3.6(a) illustrates the response of the SOA-MZI at outputs I and J as a function of $\overline{P}_A$ in logarithmic scale. Figure 3.6(b) depicts the same response but for a linear scale and for a more limited range of $\overline{P}_A$ values. In this case, we can observe the non-linearity of the SOA-MZI response, which hence underlines the need to improve the linearity of the response as a function of the power $P_A(t)$ of the signal to be sampled. The quasi-static response in Figure 3.6(a) is different from the static response in Figure 2.12. The main difference is that for low $\overline{P}_A$ values,

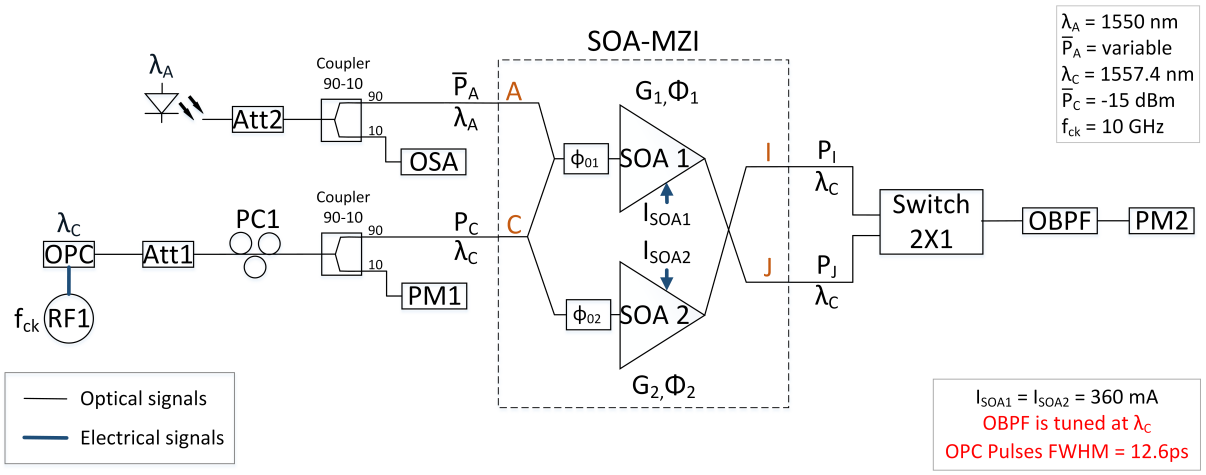

Figure 3.5: Quasi-static characterization experimental setup in order to choose the average power of $P_A(t)$. Att: Optical Attenuator. OSA: Optical Spectrum Analyzer. OPC: Optical Pulse Clock. RF: Radio Frequency generator. PM: Optical Power Meter. OBPF: Optical Bandpass Filter. Reproduced from [1].

$\overline{P}_J$ is approximately 12 dB lower in Figure 2.12 than in Figure 3.6(a). This difference probably stems from the imperfect tuning of PC1, ϕ_{01} and ϕ_{02} in the beginning of the experimental process due to the pulsing nature of the OPC signal.

We are interested in the maximum range of injected $P_A(t)$ values in which the SOA-MZI photonic sampler can be utilized. This lies between a response minimum and maximum (as is the case for the MZM). We choose the first such range between – 30 dBm and – 5 dBm. The obvious choice for $\overline{P}_A$ is at the middle of this range (i.e. – 8 dBm), so that an intensity-modulated signal with an MI of 100% can take power values within the whole permissible range of $P_A(t)$ values and thus, the usable ER of the sampled signal is the highest possible. To ensure that we never surpass, even instantaneously, the maximum in case of an eventual fluctuation due to temperature changes, $\overline{P}_A$ is chosen 1 dB lower than the middle of the specified range, i.e. – 9 dBm or 0.126 mW.

In order to demonstrate that there is not a significant degradation of the pulses when using the Modulation architecture, a visual comparison is made in Figure 3.7 of a pulse at the SOA-MZI input C and SOA-MZI output J for $\overline{P}_A$ = -9 dBm. In this Figure, we observe that the FWHM and the shape of the pulses is practically the same. Both P_C and P_J values are normalized.

An estimation of the Total Harmonic Distortion (THD) as a function of the MI is made based on the quasi-static response of Figure 3.6. $\overline{P}_J$ response are curve-fitted through interpolation to a 12th order polynomial. The THD is estimated assuming an ideal sinusoidal signal at port A with an average optical power equal to – 9 dBm. A Fast-Fourier Transformation (FFT)

is applied on the time domain estimation of P_J in order to produce its electrical spectra and subsequently calculate its THD. The estimated THD is shown in Figure 3.8.

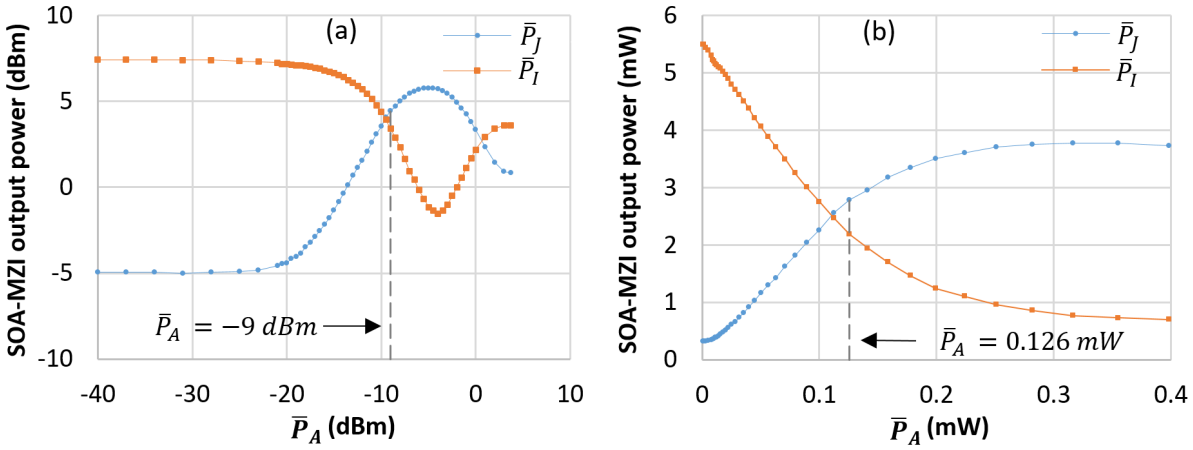

Figure 3.6: Quasi-static response of SOA-MZI in logarithmic (a) and in linear (b) scale. (a) is reproduced from [1].

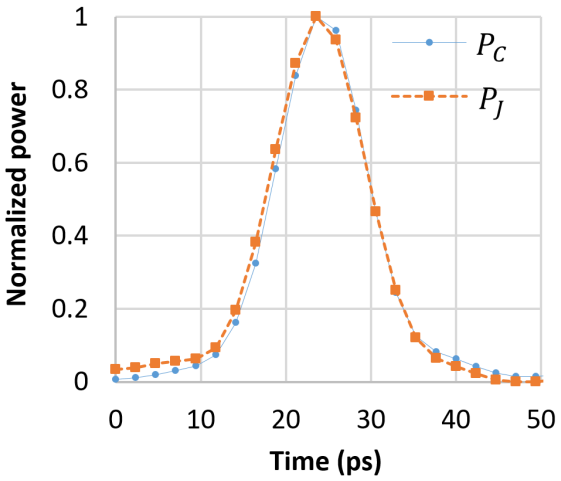

Figure 3.7: Comparison of the normalized values of pulses between the input power P_A, and the output power P_J. The temporal resolution in the Figure, which is equal to that of the DCA oscilloscope, is 2.35 ps.

We observe in Figure 3.8 that the estimated THD of SOA-MZI direct output J as a function of MI, increases from $MI = 5\%$ up to $MI = 80\%$, and subsequently there is a quasi-flat region

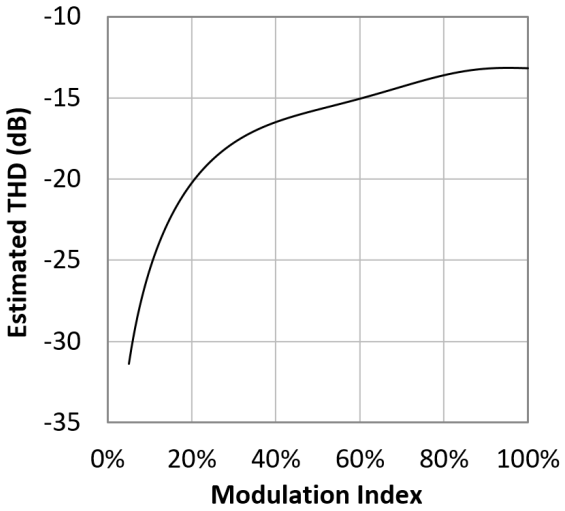

Figure 3.8: THD estimation of SOA-MZI direct output J as a function of the MI of the signal to be sampled. The THD estimation is based on the quasi-static results.

between $MI = 80\%$ and $MI = 100\%$. Except for this quasi-flat region, the shape of the curve is similar to the shape of the log function. The estimated deterioration of the linearity of the sampling process as a function of MI makes pertinent the need of a linearization method in order to decrease the non-linearity of the sampler, especially for high MI values where the usable extinction ratio is also higher. Therefore, a post-linearization method is formulated and experimentally validated in subsection 3.3 aiming at responding to that need.

3.2.3 Dynamic response

3.2.3.1 Experimental Setup

The SOA-MZI sampling pulse signal is produced, and ϕ_{01}, ϕ_{02} and PC1 are adjusted, in the same way as in quasi-static regime measurement. A continuous-wave signal tuned at $\lambda_A = 1550$ nm is intensity-modulated by an MZM, which is biased at the quadrature point with $V_{bias} = 3.1$ V and produces a sinusoidal Double Sideband Full Carrier (DSB-FC) signal whose frequency f_{dat} is provided by an RF generator. The DSB-FC signal serves as the signal to be sampled that enters SOA-MZI port A. $\overline{P}_A$ is chosen at – 9 dBm, as previously mentioned.

The power of the pulses at outputs I and J as well as the power at input A are measured after optical filtering using a sampling oscilloscope (Keysight N1000A DCA-X with N1030A calibrated optical plugin), and the datasets of the three signals are recorded and saved. Additionally, $\overline{G}_2$ is measured optically and found equal to 26 dB.

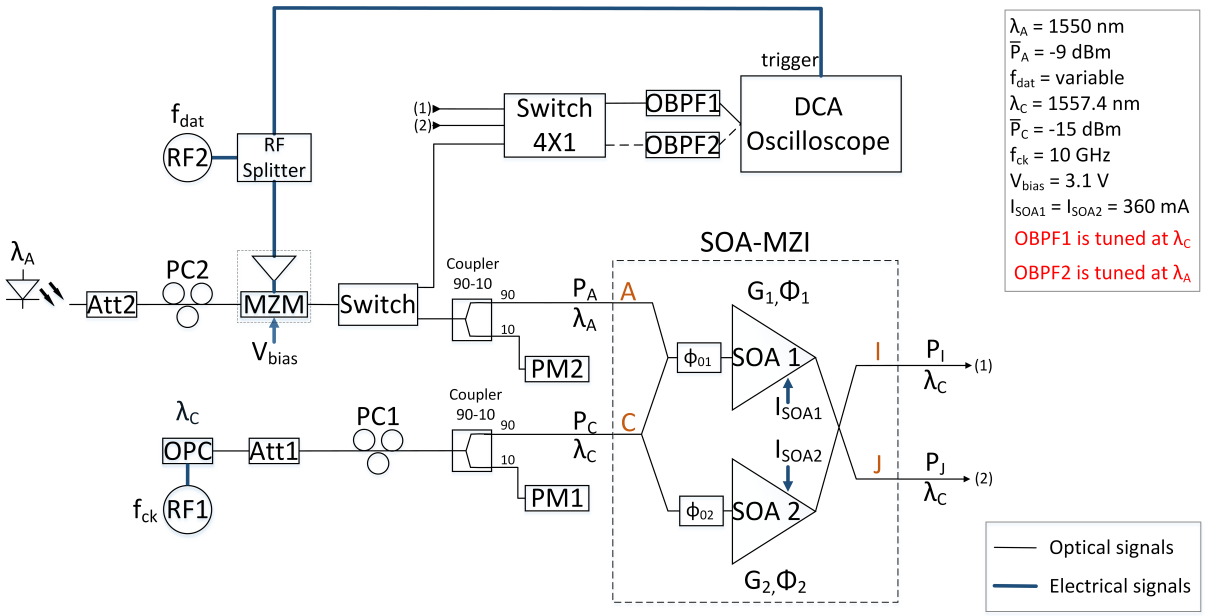

Figure 3.9: Dynamic characterization setup. MZM: Mach-Zehnder Modulator. DCA: Keysight N1000A Digital Communication Analyzer. Reproduced from [1].

3.2.3.2 Experimental results

For the results presented in the following, the MI is defined as the ratio of the difference between the maximum and the minimum value of P_A to their sum.

An example of a signal to be sampled with $f_{dat} = 1$ GHz and $MI = 60\%$ is shown in Figure 3.10(a), and of the sampling signal in Figure 3.10(b). The corresponding sampled signals at port I and J are shown in Figure 3.11(a) and Figure 3.11(b), respectively. Comparing these Figures visually we observe that the average value of P_I peaks is lower than the average value of $P_J(t)$ peaks, and thus we infer that the average value of P_I is also lower than the average value of P_J as expected by the quasi-static response in Figure 3.6(b). Moreover, another observation is that the amplitude variation of $P_I(t)$ is higher than the amplitude variation of $P_J(t)$ which can be verified from the quasi-static response in Figure 3.6(b). More analytically, in Figure 3.6(b), the calculation of an approximate value of $\overline{P}_I(t)$ and $\overline{P}_J(t)$ variations for $\overline{P}_A = 0.126$ mW (or -9 dBm) and $MI = 60\%$ gives a higher absolute variation for $\overline{P}_I$ (≈ 2.75 mW) than for $\overline{P}_J$ (≈ 2.28 mW).

All oscilloscope measurements have been obtained using averaging acquisition mode of 1024 values. The optical plugin RMS noise, which is the main source of error in the oscilloscope, is 45 μW. Due to averaging the measured RMS error of the time domain results is reduced to $45/\sqrt{1024} = 1.41$ μW.

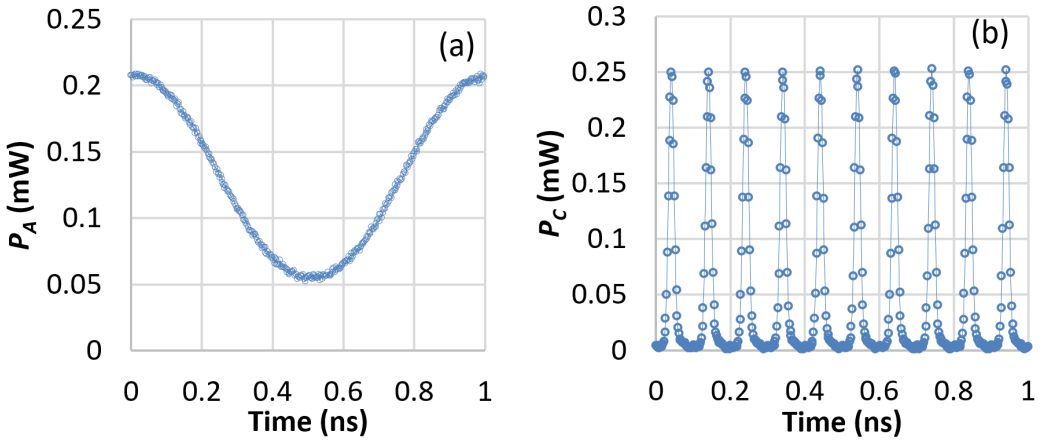

Figure 3.10: Input power at SOA-MZI port A (a) and port C (b) for $f_{dat} = 1$ GHz and $MI = 60\%$. The temporal resolution in the Figures, which is equal to that of the DCA oscilloscope, is 2.35 ps. Reproduced from [1].

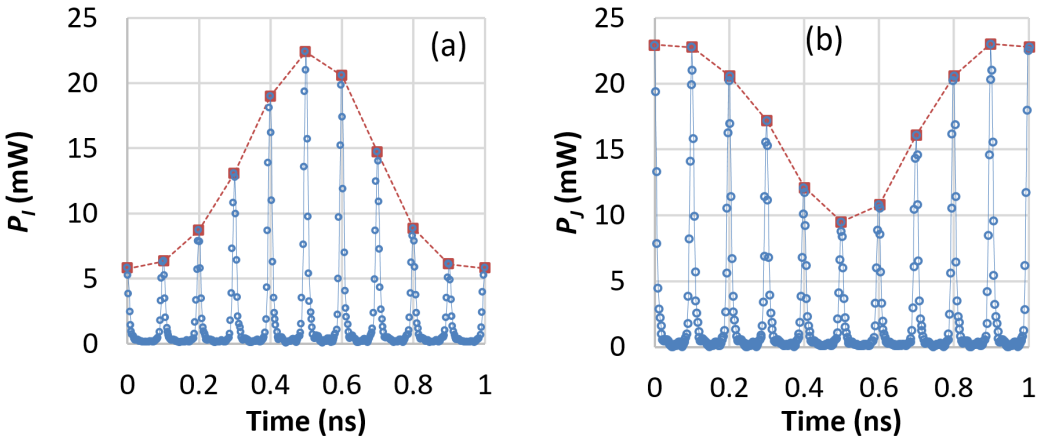

Figure 3.11: Power at port I (a) and port J (b) of the sampled signal for $f_{dat} = 1$ GHz and $MI = 60\%$. The pulses peaks which correspond to the samples are illustrated by the dashed line in (a) for port I and in (b) for port J. All oscilloscope measurements have been obtained using averaging acquisition mode of 1024 values. The temporal resolution in the Figures, which is equal to that of the DCA oscilloscope, is 2.35 ps. Reproduced from [1].

3.3 Linearization model

3.3.1 Introduction

Sampling is a fundamental signal processing function of Analog Radio over Fiber (ARoF) links. Nevertheless, because the sampler characteristic function is not linear, the distortion products that appear at the output degrade the performance of the link, especially for signals with high modulation indices [11–13]. Thus, mitigation of nonlinear distortion i.e., linearization, is the

key in order to improve the performance and expand the exploitable input power range of the photonic sampler [11, 12].

A significant performance improvement of the optical sampling process has been achieved by employing a post-distortion linearization technique and applying it to an MZM [11, 12]. The potential of this technique gave rise to the idea of applying a similar post-distortion linearization method for the first time to a SOA-MZI.

THD is a fundamental metric for almost any communication system, especially in the context of broadband RF systems [14, 15]. High THD may signify interference for other equipment or require elaborate filtering at the expense of increased cost and complexity of the ARoF link. Recently, THD has been evaluated for the SOA-MZI photonic sampler in [13, 16]. Applying the post-distortion linearization technique to this case aims exactly at minimizing THD of the SOA-MZI photonic sampler.

3.3.2 Principle of operation of the post-distortion linearization method

Figure 3.12 illustrates the principle of operation of the post-distortion linearization method in an SOA-MZI. In this method, the function of sampling is obtained using a modulation architecture presented analytically in subsection 3.1.1 of the dissertation and published. In the SOA-MZI, a sampling pulse train of instantaneous power $P_C(t)$, center wavelength λ_C, repetition rate f_{ck} and equal amplitude pulses generated by a mode-locked laser, is applied at input C, while a sinusoidal signal to be sampled of instantaneous power $P_A(t)$, modulation index (MI), center wavelength λ_A and frequency f_{dat} is applied at input A. These signals interact inside the SOA-MZI via Cross-Phase Modulation (XPM), so that the pulse train is amplitude modulated in accordance with the variations of the amplitude of the signal to be sampled. The result of this process at λ_C is obtained at the SOA-MZI outputs I and J, which are complementary, i.e. the outcomes therein exhibit opposite variations. The use of the Modulation architecture [17] means that the sampling signal with a repetition frequency f_{ck} is only amplified, so f_{ck} can be very high due to the high optical amplification bandwidth of the SOA, despite the dynamics of the SOA carriers. On the other hand, the signal to be sampled, at the frequency f_{dat}, must be below the cut-off frequency of the XPM process, which depends on the dynamics of the SOA carriers. As a consequence, the analog bandwidth of the SOA-MZI photonic sampler is limited by the XPM bandwidth, which is between 5 GHz and 6 GHz for the specific operating conditions as presented in detail in 3.2.3. In our photonic sampling architecture, we use a technique referred to as post-distortion linearization that combines at each sampling instant the power at the complementary ports I and J to invert the SOA-MZI transfer function. In order to achieve this, the two signals emerging from ports I and J which have been detected by an oscilloscope and the recorded datasets are stored as presented in subsection 3.2.3. Then, a signal processing unit exploits the mathematical model that is formulated in subsection 3.3.3 and subsequently empirically corrected by a simple

optimization process based on experimental results in subsection 3.3.4. This is done in order to linearize the output and estimate the power of the signal to be sampled, $P_A(t)$, by $\hat{P}_A(t)$ using the stored datasets from ports I and J, the operating parameters of the SOA-MZI as well as the empirical correction coefficients.

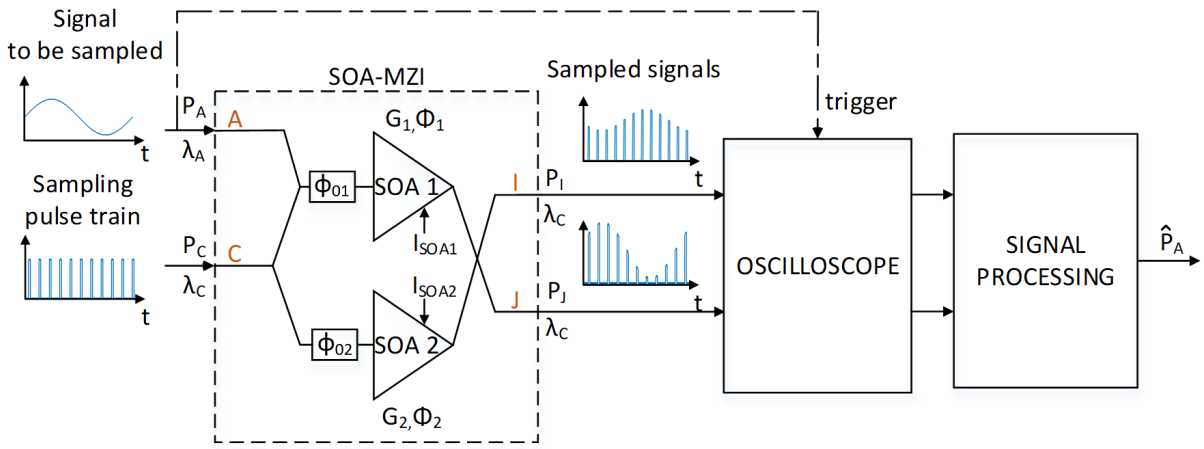

Figure 3.12: Conceptual diagram for application of post-distortion linearization method in an SOA-MZI photonic sampler. Reproduced from [1].

3.3.3 Linearization mathematical model

We develop our model on the assumption of a static SOA regime. Although by making such an approximation it is expected that the SOA and SOA- MZI response will deviate from the real one, still the inevitable discrepancy can be kept acceptable within the considered operating range of use of this device and module, respectively. Furthermore, the model's accuracy can be improved by applying an empirical correction approach, as it will be described in subsection 3.3.4. In this manner, we manage to formulate a sufficiently precise model while preserving its simplicity and its ability to produce analytic solutions.

The SOA-MZI output power emerging from ports I and J at the wavelength λ_C is given by equations (2.48) and (2.49) as developed in chapter 2 and section 2.4. Using Equations (2.48), (2.49) and $\phi_0 = 0$, the difference between P_I and P_J is:

$$P_I(t) - P_J(t) = \frac{1}{2}\sqrt{G_1(t)G_2(t)} \cdot cos(\Delta\Phi(t)) \cdot P_C(t) \tag{3.1}$$

Now we can express the phase difference between the two arms of the SOA-MZI in relation

to the output powers, P_I and P_J, and the input power of the sampling pulse train, P_C:

$$\Delta\Phi(t) = \Phi_1(t) - \Phi_2(t) = cos^{-1}\left(\frac{2}{\sqrt{G_1(t)G_2(t)}}\frac{P_I(t) - P_J(t)}{P_C(t)}\right) \tag{3.2}$$

Calculating the sum of the powers P_I and P_J using Equations (2.48) and (2.49), and subsequently expressing the input power P_C in relation to the output powers P_I, P_J and the gains G_1 and G_2 results in:

$$P_C(t) = 4\frac{P_I(t) + P_J(t)}{G_1(t) + G_2(t)} \tag{3.3}$$

Using Equation (3.3) and solving for G_1 we get the following expression:

$$G_1(t) = 4\frac{P_I(t) + P_J(t)}{P_C(t)} - G_2(t) \tag{3.4}$$

The same analysis and thus Equation (3.4) is also valid for the average value of powers and gains given by [26]:

$$\overline{G}_1 = 4\frac{\overline{P}_I(t) + \overline{P}_J(t)}{\overline{P}_C(t)} - \overline{G}_2(t) \tag{3.5}$$

Substituting the expression for P_C from Equation (3.3) in Equation (3.2) we have:

$$\Delta\Phi(t) = \Phi_1(t) - \Phi_2(t) = cos^{-1}\left(\frac{1}{2}\frac{P_I(t) - P_J(t)}{P_I(t) + P_J(t)} \cdot \frac{G_1(t) + G_2(t)}{\sqrt{G_1(t)G_2(t)}}\right) \tag{3.6}$$

Equation (3.6) is also valid for the average value of phases, powers and gains given by [26]:

$$\Delta\overline{\Phi} = \overline{\Phi}_1 - \overline{\Phi}_2 = cos^{-1}\left(\frac{1}{2}\frac{\overline{P}_I - \overline{P}_J}{\overline{P}_I + \overline{P}_J} \cdot \frac{\overline{G}_1 + \overline{G}_2}{\sqrt{\overline{G}_1\overline{G}_2}}\right) \tag{3.7}$$

In order to couple the phase difference $\Delta\Phi$ with the input signals injected into ports A and C at wavelengths λ_A and λ_C and of power P_A and P_C, respectively, we use the carrier density rate for SOA1 and for SOA2. Carrier density rate for SOA1 is given by Equation (2.23) with $S \in \{A, C\}$ as two signals at wavelengths λ_A and λ_C are injected into the aforementioned SOA:

$$\frac{\partial N_1(t)}{\partial t} = R_{p1} - R_1(t) - R_{A1}(t) - R_{C1}(t) \tag{3.8}$$

where the subscript 1 has been appended to R_p and R, R_A and R_C in order to declare the corresponding parameters of SOA1. Using Equation (2.27) and considering the fact that half of the P_A power gets into $SOA1$, R_{A1} is given by:

$$R_{A1}(t) = \frac{1}{2}\frac{\lambda_A}{hc} \cdot \frac{\Gamma \cdot g_{m1}(N_1(t))}{g_{n1}(N_1(t))} \cdot \frac{G_1(N_1(t)) - 1}{V} \cdot P_A(t) \tag{3.9}$$

where the subscript 1 has been appended to g_m and g_n and G in order to declare the corresponding parameters of SOA1.

Using Equation (2.27) and considering the fact that a quarter of the P_C power gets into $SOA1$, R_C is given by:

$$R_C(t) = \frac{1}{4}\frac{\lambda_A}{hc} \cdot \frac{\Gamma \cdot g_{m1}(N_1(t))}{g_{n1}(N_1(t))} \cdot \frac{G_1(N_1(t)) - 1}{V} \cdot P_C(t) \tag{3.10}$$

Applying Equations (3.9), (3.10) and (2.24) to Equation (3.8) and using the approximation $\frac{\Gamma \cdot g_{m1}(N_1(t))}{g_{n1}(N_1(t))} = 1$, as in [17, 21], we obtain:

$$\frac{\partial N_1(t)}{\partial t} = \frac{I_{SOA1}}{qV} - \frac{N_1(t)}{\tau_{eff}} - \frac{1}{2}\frac{\lambda_A}{hcV}P_A(t) \cdot (G_1(N_1(t)) - 1) - \frac{1}{4}\frac{\lambda_C}{hcV}P_C(t) \cdot (G_1(N_1(t)) - 1) \tag{3.11}$$

We can express the SOA1 carrier density in the static regime, which is defined by $\frac{\partial N_1(t)}{\partial t} = 0$, by the following equation:

$$\overline{N}_1 = \frac{1}{\Gamma\alpha \cdot L \cdot P_{sat}}\left[\frac{hcI_{SOA1}}{q\lambda_C} - \frac{1}{4}\overline{P}_C \cdot (\overline{G}_1 - 1) - \frac{1}{2}\frac{\lambda_A}{\lambda_C}\overline{P}_A \cdot (\overline{G}_1 - 1)\right] \tag{3.12}$$

where P_{sat} is given by:

$$P_{sat} = \frac{hcV}{\lambda_C \Gamma\alpha \cdot L \cdot \tau_{ASE}} \tag{3.13}$$

For SOA2, provided that its physical parameters (Γ, α, L, P_{sat}) are the same as for SOA1, and given the fact that a single optical signal passes through it at λ_C, we have, after following the same analysis as for SOA1:

$$\overline{N}_2 = \frac{1}{\Gamma\alpha \cdot L \cdot P_{sat}}\left[\frac{hc \cdot I_{SOA2}}{q\lambda_C} - \frac{1}{4}\overline{P}_C \cdot (\overline{G}_2 - 1)\right] \tag{3.14}$$

From Equation (3.8) and (3.14) and $I_{SOA1} = I_{SOA2} = I_{SOA}$, we obtain the difference between the SOA1 and SOA2 carrier density by:

$$\overline{N}_1 - \overline{N}_2 = \frac{1}{\Gamma\alpha L P_{sat}}\left[\frac{1}{4}\overline{P}_C \cdot (\overline{G}_2 - \overline{G}_1) - \frac{1}{2}\frac{\lambda_A}{\lambda_C}\overline{P}_A \cdot (\overline{G}_1 - 1)\right] \tag{3.15}$$

The linearized expression of the SOA active zone effective refractive index as a function of carrier density is given by [18]:

$$\overline{n}_{ex} = n_{e0} + \frac{\partial n_e}{\partial N}(\overline{N}_x - N_0),\ x \in \{1, 2\} \tag{3.16}$$

where n_{e0} is the refractive index at transparency. The expression relating the refractive index

and the phase difference is:

$$\overline{\Phi}_x = \frac{2\pi \overline{n}_{ex} L}{\lambda_C},\ x \in \{1, 2\} \tag{3.17}$$

Applying Equations (3.15) and (3.16) to (3.17), we can calculate the phase difference between the SOAs' outputs. This difference at wavelength λ_C is given by:

$$\Delta\overline{\Phi} = \overline{\Phi}_1 - \overline{\Phi}_2 = \frac{\alpha_H}{2P_{sat}} \left[\frac{1}{4} \overline{P}_C \cdot (\overline{G}_1 - \overline{G}_2) + \frac{1}{2} \frac{\lambda_A}{\lambda_C} \cdot \overline{P}_A \cdot (\overline{G}_1 - 1) \right] \tag{3.18}$$

Applying Equation (2.29) and then Equation (2.28 in (2.16), α_H can be expressed as:

$$\alpha_H = -\frac{4\pi}{\lambda_C} \frac{\frac{\partial n_e}{\partial N}}{\frac{\partial \Gamma g_{m,x}}{\partial N}} = -\frac{4\pi}{\lambda_C \Gamma \alpha_C} \frac{\partial n_e}{\partial N} \tag{3.19}$$

Although Equation (3.2) has been derived for the instantaneous phase difference $\Delta\Phi$ using the instantaneous powers P_I, P_J, at ports I and J, and instantaneous gains G_1, G_2 of SOA1 and SOA2, respectively, Equation (3.18) has been derived for the average value of $\Delta\overline{\Phi}$ using the average powers $\overline{P}_C$ and $\overline{P}_A$ and average gains $\overline{G}_1$ and $\overline{G}_2$. Equating Equations (3.2) and (3.18) and using the approximations $\overline{P}_C = P_C(t)$, $\overline{G}_1 = G_1(t)$ and $\overline{P}_A = P_A(t)$ permits us to express the instantaneous power P_A as a function of the instantaneous measured parameters (powers and gains) and thus approximate it empirically by:

$$\hat{P}_A(t) = \frac{\lambda_C}{\lambda_A} \frac{2}{G_1(t) - 1} \left[\frac{2P_{sat}}{\alpha_H} cos^{-1} \left[\frac{1}{2} \frac{P_I(t) - P_J(t)}{P_I(t) + P_J(t)} \cdot \frac{G_1(t) + G_2(t)}{\sqrt{G_1(t) G_2(t)}} \right] - \frac{1}{4} P_C(t) \cdot (G_1(t) - G_2(t)) \right] \tag{3.20}$$

Equation (3.20) is valid also for average values of powers and gains given by:

$$\widehat{\overline{P}}_A = \frac{\lambda_C}{\lambda_A} \frac{2}{\overline{G}_1 - 1} \left[\frac{2P_{sat}}{\alpha_H} cos^{-1} \left[\frac{1}{2} \frac{\overline{P}_I - \overline{P}_J}{\overline{P}_I + \overline{P}_J} \cdot \frac{\overline{G}_1 + \overline{G}_2}{\sqrt{\overline{G}_1 \overline{G}_2}} \right] - \frac{1}{4} \overline{P}_C \cdot (\overline{G}_1 - \overline{G}_2) \right] \tag{3.21}$$

3.3.4 Linearization of sampled continuous-wave signals

3.3.4.1 Linearization and model corrections

The linearization method is applied on the sampling of continuous-wave signals shown in Figure 3.6. First, $\overline{G}_2$ is measured optically and found equal to 26.8 dB. Afterwards, the average values $\overline{P}_I$, $\overline{P}_J$ and $\overline{P}_C$ as well as the previously measured $\overline{G}_2$ are used in order to recover the values of $\overline{G}_1$ from Equation (3.5). With $\overline{G}_1$ at every point in Figure 3.6 known, the nonlinear phase shift $\Delta\Phi$ can also be recovered from Equation (3.6). Finally, the estimated $\hat{P}_A$ is given by Equation

(3.20). The value of the $\frac{P_{sat}}{\alpha_H}$ ratio is 5.82 mW. It is worth noting that the optical gain $\overline{G}_2$, at the lower arm of the SOA-MZI, does not depend on $\overline{P}_A$, therefore $\overline{G}_2$ only needs to be measured once at the beginning of the process.

Observing the results in Figure 3.13(a), we notice that we have an offset error and a slope gain error. These differences are due to the simplifications made throughout the above theoretical development, such as the perfect symmetry between the SOA-MZI arms, the identical physical parameters Γ, α, L and P_{sat} for SOA1 and SOA2, the negligible SOAs internal losses α_{int} compared to Γg_{m1}, i.e. $\Gamma g_{m1} = g_{n1}$ and $\phi_0 = 0$. Thus, to correct the slope and offset of the estimated input power, we apply two empirical correction coefficients denoted by *'gco'* and *'off'*, respectively, which are estimated using the experimental results. To this end, $\overline{P}_A$ can be estimated by $\widehat{\overline{P}}_A$ with the use of the following expression:

$$\widehat{\overline{P}}_A = gco\left[\frac{\lambda_C}{\lambda_A}\frac{2}{\overline{G}_1 - 1}\left(\frac{2P_{sat}}{\alpha_H}\cdot\Delta\overline{\Phi} - \frac{1}{4}\overline{P}_C\cdot(\overline{G}_1 - \overline{G}_2)\right)\right] + off \tag{3.22}$$

The same expression with the instantaneous values of powers and using the static case approximation is given by:

$$\hat{P}_A(t) = gco\left[\frac{\lambda_C}{\lambda_A}\frac{2}{G_1(t) - 1}\left(\frac{2P_{sat}}{\alpha_H}\cdot\Delta\Phi(t) - \frac{1}{4}P_C(t)\cdot(G_1(t) - G_2(t))\right)\right] + off \tag{3.23}$$

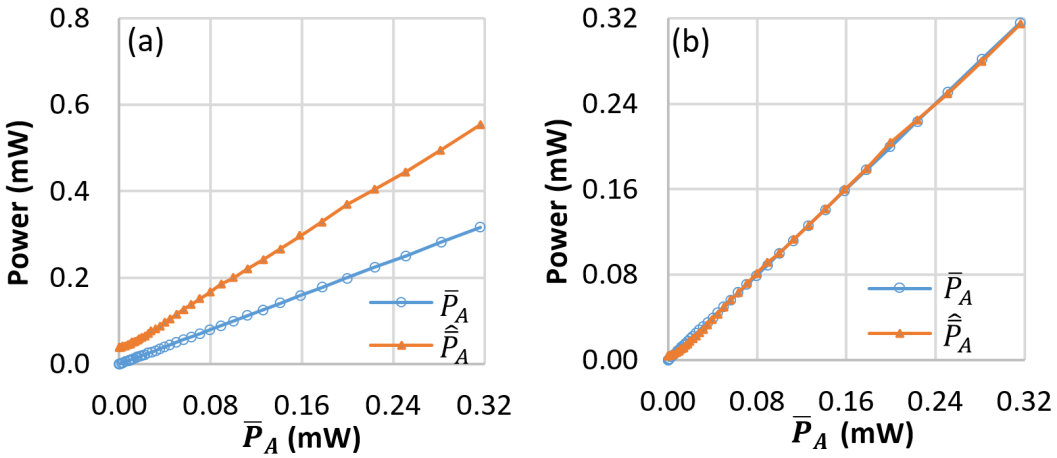

Figure 3.13: Comparison of the estimated $\widehat{\overline{P}}_A$ after the application of the post-distortion linearization method and the injected $\overline{P}_A$ for the quasi-static results in Figure 3.6 without the use of coefficients (a) and with *'gco'* = 0.48 and *'off'* = – 17.9 µW (b) for the range between 0.0001 mW and 0.32 mW or equivalently between – 40 dBm and – 5 dBm. Reproduced from [1].

In Figure 3.13(b), we introduce *'gco'* and *'off'* coefficients as in Equation (3.22), and then

we optimize their values by using a least squares approximation in order to minimize the error between $\widehat{\overline{P}}_A$ and $\overline{P}_A$. The optimized values are equal to 0.48 for *'gco'* and equal to – 17.9 μW for *'off'*.

Utilizing the linearization technique for continuous-wave signals, while employing the *'gco'* and *'off'* empirical correction coefficients as in Figure 3.13(b), we obtain an estimated percentage of the absolute error between P_A and $\hat{P}_A$, $APE_{\hat{A}}$, as low as 9.1% for the whole range between 0.0001 mW and 0.32 mW or equivalently between – 40 dBm and – 5 dBm. Moreover, $APE_{\hat{A}} =$ 7.2% for a signal with -9 dBm average power and $MI = 100\%$.

3.3.4.2 Estimation of THD improvement

In order to establish the potential improvement in the performance of SOA-MZI photonic sampler provided by the method, we can make an estimation of the THD of the linearized response $\hat{P}_A$, based on the quasi-static results in Figure 3.13(b) and compare it to the estimated THD of $\overline{P}_J$ presented in Figure 3.6. $\hat{P}_A$ response is curve-fitted through interpolation to a 12th order polynomial and the THD is estimated assuming an ideal sinusoidal signal at port A with an average optical power equal to – 9 dBm. An FFT is applied on its time domain estimation in order to produce their electrical spectra and subsequently calculate its THD and the THD improvement provided by the technique. THD for the quasi-static regime is defined as the ratio of the estimated output electrical power at the frequency of the ideal input signal f_{dat} divided by the sum of the powers of the first 3 Harmonic Distortions at $2f_{dat}$, $3f_{dat}$ and $4f_{dat}$.

Figure 3.14 shows a comparison between the estimated THD of the signal after the application of the linearization method, denoted as 'THD post-pr' to distinguish it from that at the SOA-MZI direct output J, denoted as 'THD PJ', as a function of MI of the signal to be sampled.

The estimated THD improvement in Figure 3.14 is extremely high for the range of MI values between 5% and 100% and it is always between approximately 20 dB and 24 dB. The ripple in the THD improvement curve is caused by rippling in the THD post-pr curve mostly due to the somewhat increased effectiveness of the linearization method around a peak at $MI = 76.4\%$. The highest THD improvement observed for this peak is equal to 23.8 dB.

It should be noted that the THD estimation of the quasi-static regime does not take into account the dynamic phenomena that take place into the SOA-MZI, and this estimation is valid only for low frequencies, while it is compromised at high frequencies. Also, it should be emphasized that the quasi-static regime results are based on measurements using an optical power meter, whereas the dynamic regime results presented in 3.3.5 are based on measurements using a wide bandwidth oscilloscope.

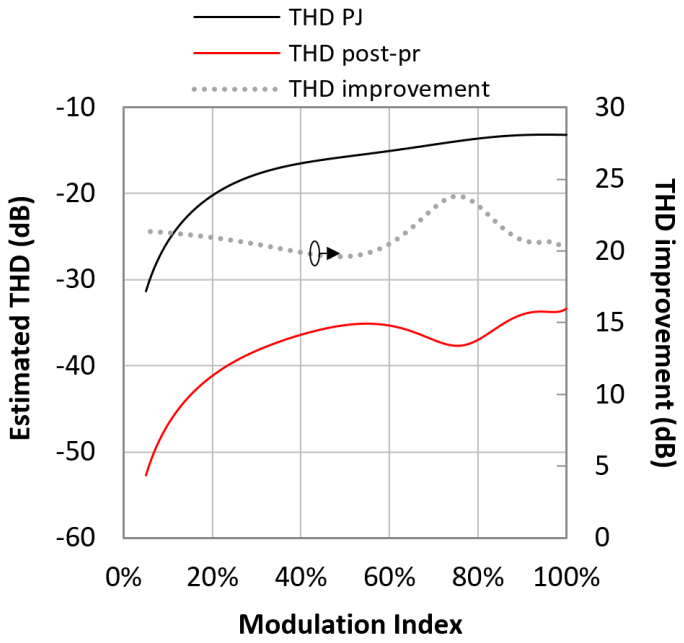

Figure 3.14: Comparison between estimated THD of linearized and SOA-MZI's direct output J as a function of the MI of the signal to be sampled. The THD estimation is based on the quasi-static results.

3.3.5 Linearization of sampled sinusoidal signals

3.3.5.1 Experimental Setup and Conditions

The linearization measurement setup in the dynamic regime is shown in Figure 3.15. The only difference with Figure 3.9 is that a signal processing procedure has been added which apply the equations of the post-distortion linearization method to the datasets already saved by the DCA oscilloscope. Also, the P_C value that is used corresponds to the peak power of the pulses.

The first step of the signal's treatment is the isolation of pulses' peaks for port I and port J depicted by the dashed line curves in Figure 3.11(a) and Figure 3.11(b), respectively. The signal processing that follows is performed on the pulse peaks which are the samples that result from the sinusoidal signals' sampling. The peak power of P_C input pulses, $P_{C,peak}$, is approximately calculated from:

$$P_{C,peak} = \frac{\overline{P}_C}{f_{ck} \cdot t_{FWHM}} \tag{3.24}$$

where f_{ck} is the sampling rate and t_{FWHM} is the Full Width at half maximum of the pulses. In our case, $\overline{P}_C$ = - 15 dBm, f_{ck} = 10 GHz and t_{FWHM} = 12.6 ps, and thus $P_{C,peak}$ is approximately 0.25 mW or -6 dBm.

The next step is the recovery of dynamic gain G_1 using Equation (3.4) and of the dynamic nonlinear phase shift $\Delta\Phi$ from Equation (3.6), corresponding to every pulse peak or sample.

Finally, $\hat{P}_A$ is calculated using Equation (3.23), while the linearization model parameters and *'gco'* and *'off'* empirical correction coefficients are optimized to minimize the mean squared error between P_A and $\hat{P}_A$.

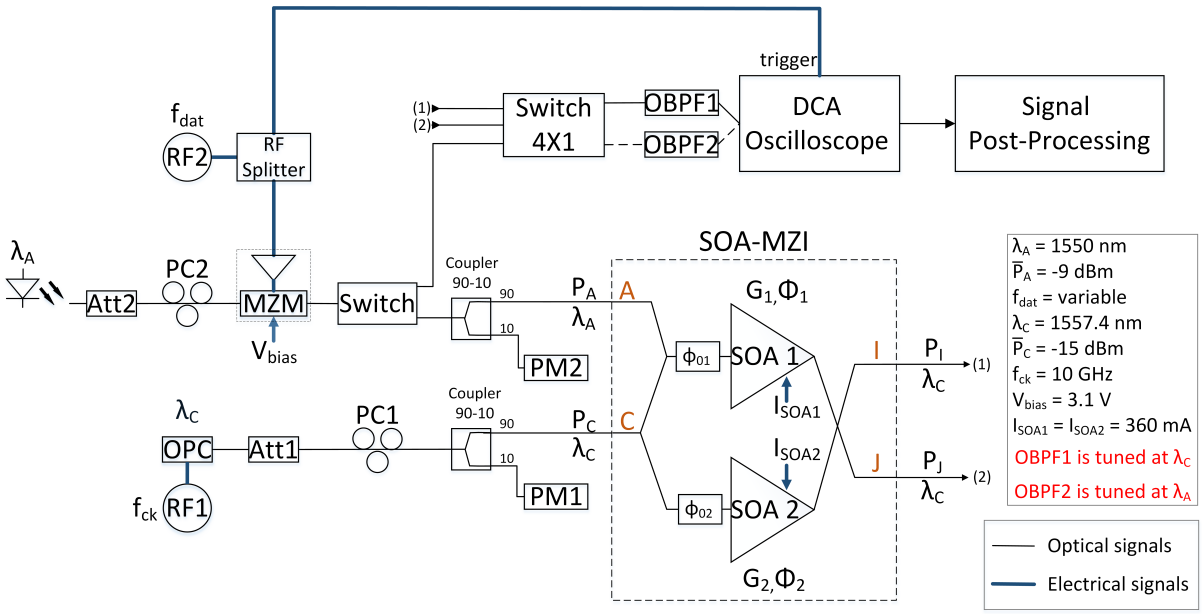

Figure 3.15: Linearization measurement setup. Reproduced from [1].

3.3.5.2 Time domain results

A visual comparison between P_A and $\hat{P}_A$ for $f_{dat} = 1$ GHz with $MI = 40\%$, for $f_{ck} = 1$ GHz with $MI = 60\%$, for $f_{ck} = 0.25$ GHz with $MI = 80\%$ and for $f_{dat} = 0.5$ GHz with $MI = 80\%$, is shown in Figure 3.16(a), (b), (c) and (d), respectively. The average percentage of the absolute error in Figure 3.16(a) before the application of the linearization method (APE_J) is 15.3% , whereas after the application ($APE_{\hat{A}}$) it is 12.3%. Similarly, APE_J in Figure 3.16(b) is 31.9%, whereas $APE_{\hat{A}}$ is 8.1%. The corresponding values before and after the application of the linearization method are $APE_J = 52.7\%$ and $APE_{\hat{A}} = 8\%$ in Figure 3.16(c), and $APE_J = 34.3\%$ and $APE_{\hat{A}} = 13\%$ in Figure 3.16(d). A conclusion that can be drown from the APE values listed above is that the linearization works more efficiently for high MI values where APE_J values are also high due to the sampled signal significant degradation by the non-linearity of SOA-MZI photonic sampler.

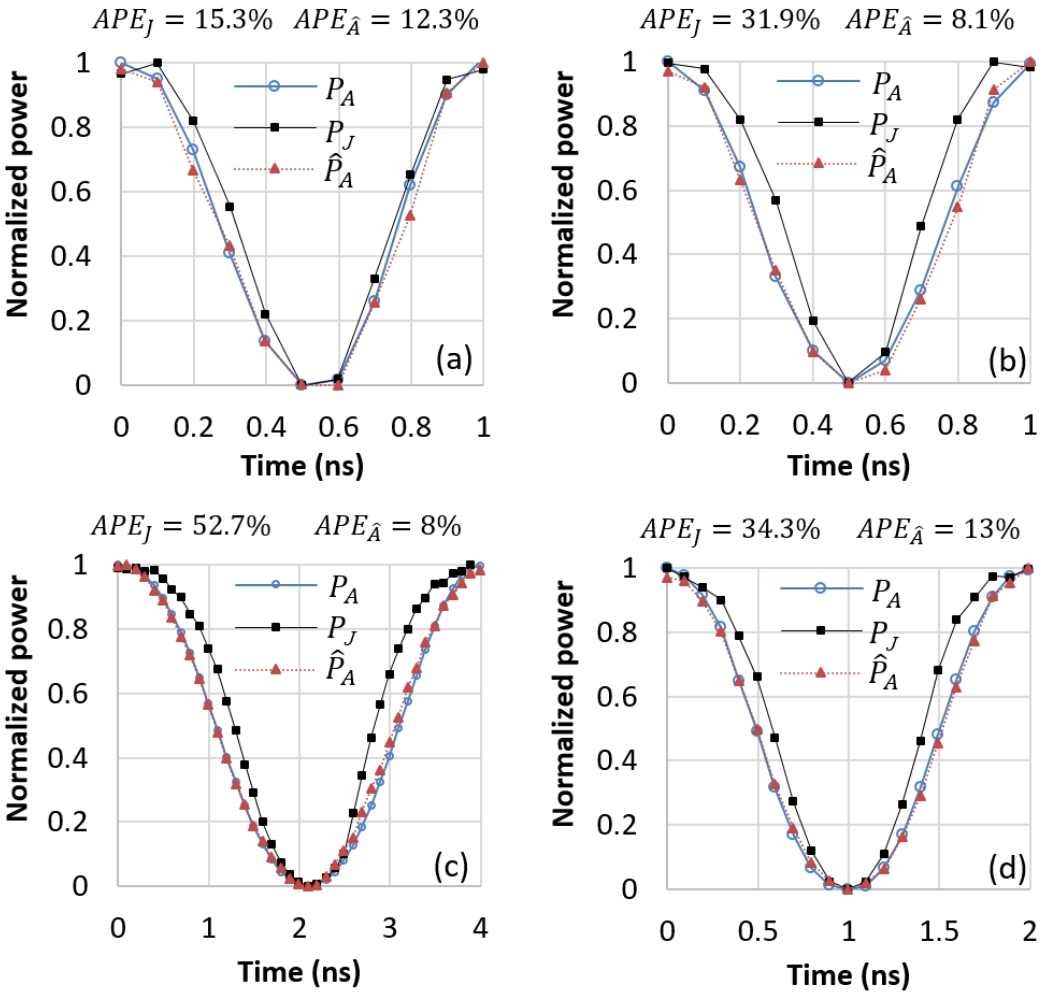

Figure 3.16: Comparison of the normalized values between the estimated $\hat{P}_A$, the injected P_A and the direct SOA-MZI output P_J. (a) $f_{dat} = 1$ GHz and $MI = 40\%$. (b) $f_{dat} = 1$ GHz and $MI = 60\%$. (c) $f_{dat} = 0.25$ GHz and $MI = 80\%$. (d) $f_{dat} = 0.5$ GHz and $MI = 80\%$. The temporal resolution in the Figures is equal to $1/f_{ck} = 100$ ps. Reproduced from [1].

3.3.5.3 THD linearization performance

In order to obtain the electrical spectrum of P_J, $\hat{P}_A$ and P_A, an FFT is performed on the respective time domain signals. An example of the electrical spectrum of P_J, $\hat{P}_A$ and P_A for the case of $f_{dat} = 1$ GHz and $MI = 60\%$ is shown in Figure 3.17(a), (b) and (c), respectively. We observe a clear improvement in terms of harmonic distortion comparing the electrical spectra after (Figure 3.17(b)) and before (Figure 3.17(a)) the application of the post-distortion method. The improvement is mostly attributed to the reduction of Harmonic Distortion 2 (HD2) at 2 GHz. The linearity of the photonic sampling mixer is assessed using THD as performance metric. For the results presented in the following, the THD is defined for the cases of f_{dat} equal to 0.25

GHz, 0.5 GHz and 1 GHz as the sum of harmonic distortion frequency components of order 2 to 4 (HD2-4) divided by the fundamental target frequency component. However, for the case of f_{dat} equal to 2 GHz the THD is defined as the HD2, which is the most significant distortion product, divided by the fundamental target frequency component. This discrepancy is due to the sampling frequency f_{ck}, which is 10 GHz, meaning that as we consider exclusively the pulses' peaks and for a Nyquist sampling rate equal to 10 GHz, the highest frequency provided by FFT is 5 GHz.

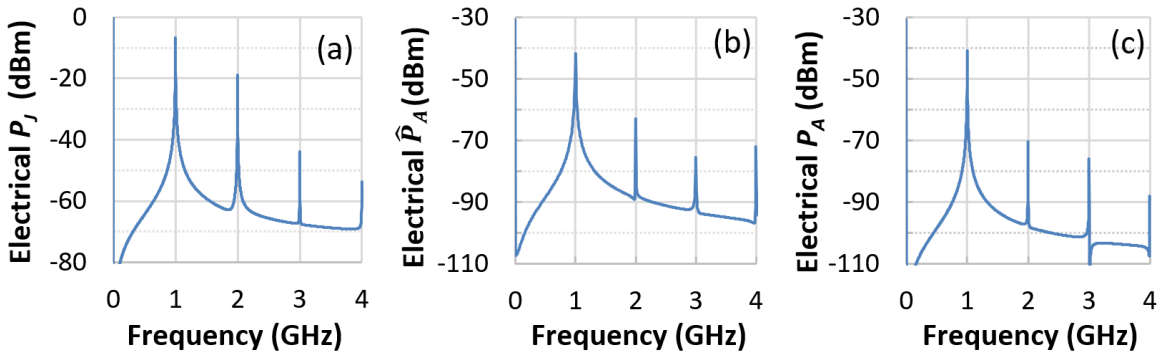

Figure 3.17: Electrical spectrum of P_J(a), $\hat{P}_A$(b) and P_A(c) calculated with Fast Fourier Transform (FFT) for $f_{dat} = 1$ GHz and $MI = 60\%$. Reproduced from [1].

3.3.5.3.1 THD results as a function of MI

Figure 3.18(a) shows a comparison between the THD of the signal after the application of the linearization method, the SOA-MZI direct output J and the signal to be sampled at the input of the SOA-MZI, denoted as 'THD modulator', as a function of the MI of the signal to be sampled. The carrier frequency f_{dat} is equal to 250 MHz. We observe that the THD improvement achieved by the linearization technique is moderate for a MI equal to 20%, significant for a MI equal to 40% and to 60%, and extremely high and equal to 23.9 dB for a MI equal to 80%.

Figure 3.18(b) depicts the same comparison as in Figure 3.18(a) but for f_{dat} equal to 1 GHz. In this figure, we notice that the maximum THD improvement provided by the method is significant and equal to 9.1 dB for MI equal to 60%. It should be noted that the error bars in the THD lines correspond to the variation in the THD values that could be caused by small random fluctuations of the order of 5% in the P_J, $\hat{P}_A$ and P_A time domain results. This error is equivalent to ± 1.5 dB for the THD post-pr, THD PJ and THD modulator lines and equivalent to ± 3 dB for the THD improvement line. Moreover, it is worth noting that from a theoretical point of view the THD results at the complementary output I are expected to be similar to that

at direct output J. Therefore, we have made the choice to compare the linearized results to the results at port J.

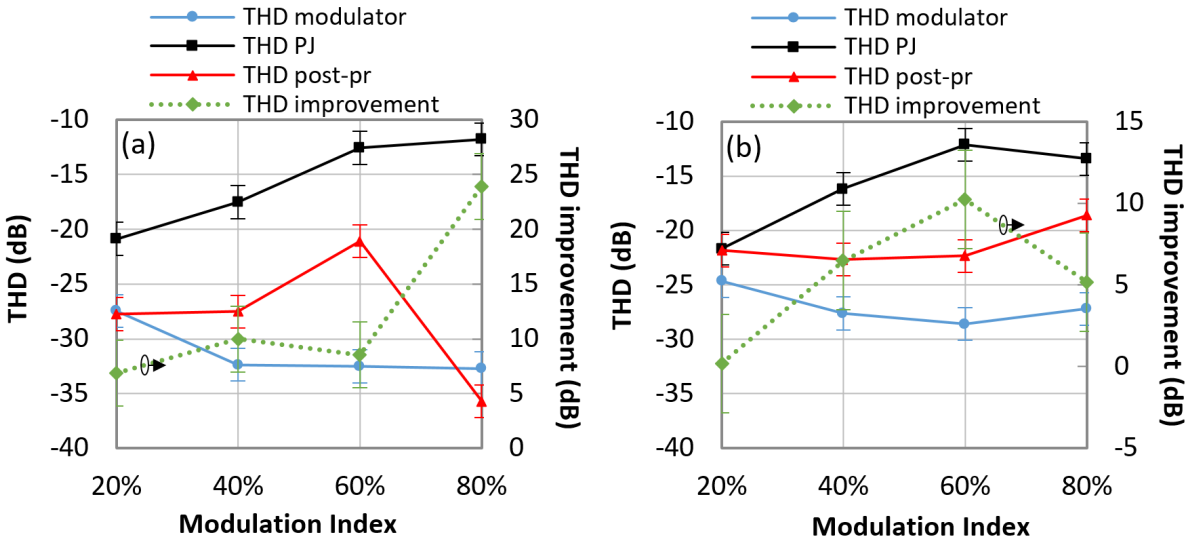

Figure 3.18: Comparison between THD of linearized and SOA-MZI's direct output as a function of the MI of the signal to be sampled. (a) f_{dat} = 250 MHz. (b). f_{dat} = 1 GHz. Reproduced from [1].

Comparing the THD response for f_{dat} equal to 250 MHz in Figure 3.18(a) with the THD quasi-static response in Figure 3.14, there is a matching between the THD post-pr, THD PJ and THD improvement values for MI equal to 80% when we take into account the 5% error bars' lower limit. However, for MI equal to 20%, 40% and 60% the THD post-pr, THD PJ and THD improvement values in Figure 3.14 compared to those in Figure 3.18(a) are significantly different even if we take into account the error bars. A possible explanation for this difference is that as the MI of the signal to be sampled decreases from 80%, the RMS error of the oscilloscope becomes more significant compared to the variation of P_J, P_I and P_A signals, thus inducing an additional error in the linearization process.

3.3.5.3.2 THD results as a function of the frequency of the signal to be sampled

Figure 3.19(a), (b) and (c) show the THD of the signal after the application of the linearization method, in comparison to that at the SOA-MZI direct output J and the THD of the signal to be sampled, as a function of the frequency f_{dat} of the signal to be sampled, for different modulation indices 40%, 60% and 80%, respectively. As a general rule, the effectiveness of the method decreases as the frequency increases due to the fact that the model's equations presented in subsection 3.3.3 are based on the assumption that $\partial N_1/\partial t = 0$. In other words, the linearization

equations are best adapted for a static or a quasi-static regime, whereas in a dynamic regime there is a growing error as the frequency increases. However, this error is not prohibiting for the application of the linearization equations on dynamic signals and, as a matter of fact, a significant THD improvement of at least 5.5 dB, taking into account the error bars' lower limit, is observed for $f_{dat} = 250$ MHz and for $f_{dat} = 500$ MHz with $MI = 40\%$, 60% and 80%, as well as for $f_{dat} = 1$ GHz and for $f_{dat} = 2$ GHz with $MI = 60\%$. For all the other cases, the benefit of using the linearization technique is always tangible but not so pronounced. The upper frequency limit that the static regime assumption seems plausible is the bandwidth of XPM, which is measured between 5 GHz and 6 GHz in 2.4.4.2 for the specific SOA-MZI.

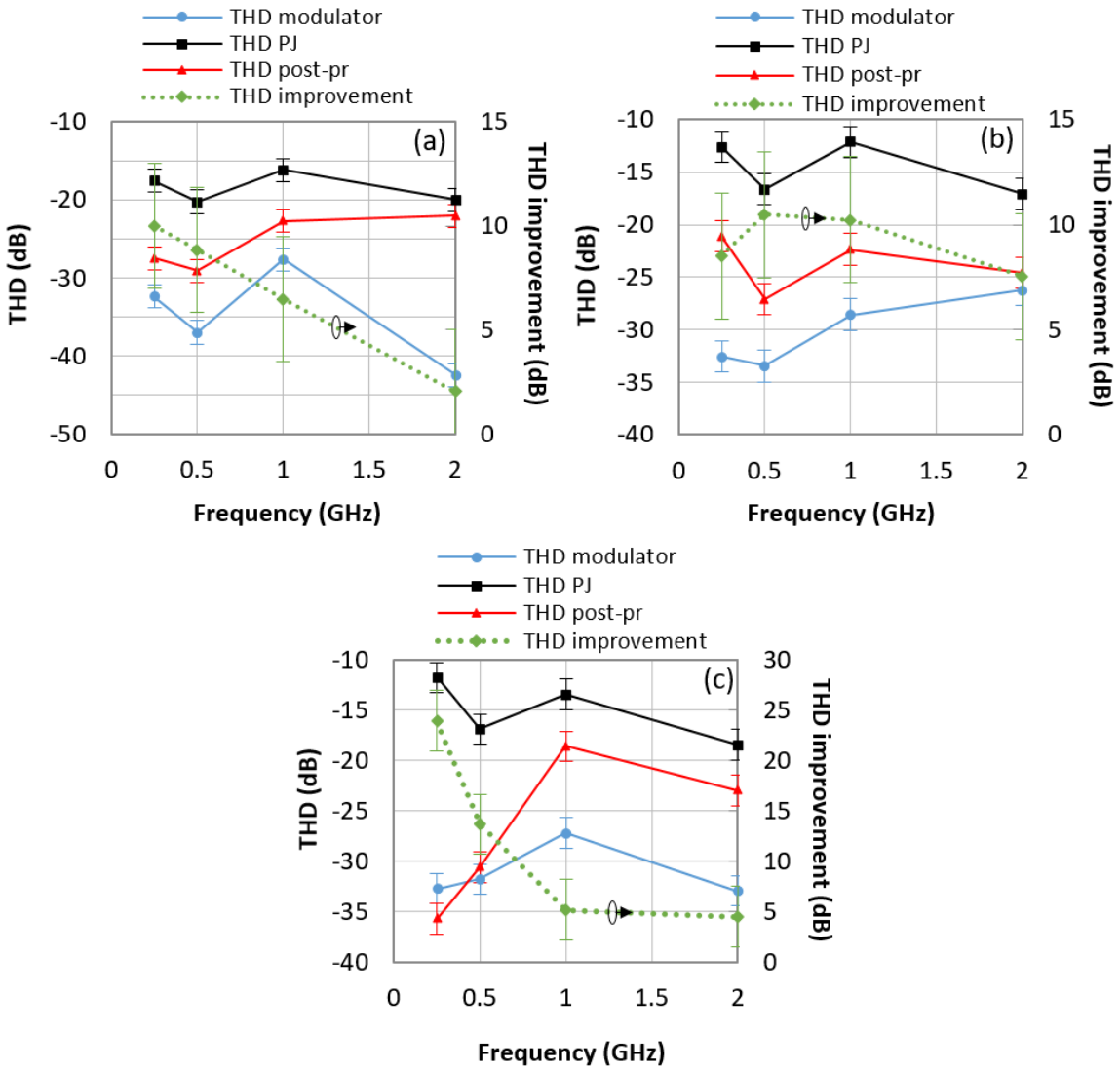

Figure 3.19: Comparison between THD of linearized and SOA-MZI's direct output as a function of the frequency f_{dat} of the signal to be sampled. (a) $MI = 40\%$. (b) $MI = 60\%$. (c) $MI = 80\%$. Reproduced from [1].

3.4 Conclusion

The quasi-static and the dynamic response of the SOA-MZI photonic sampler with pulses were studied and the deterioration of the linearity provided by the SOA-MZI photonic sampler as the MI increases was established. In order to resolve the above problem a post-distortion linearization method was formulated. The feasibility, potential and effectiveness of the post-distortion

linearization method was illustrated through theory and experiment for a SOA-MZI photonic sampler. Through application of the method to a quasi-static measurement, the estimated potential THD improvement was found to be higher than 19.6 dB for sinusoidal signals with MI between 20% and 80%. This high potential THD improvement is verified through sampling and application of the method to a sinusoidal signal at 250 MHz with MI equal to 80%. The linearization model is based on the static regime SOA equations, and thus it has the advantage of lower complexity compared to a model based on dynamic SOA equations. This approach, however, is limited by the fact that the effectiveness of the method decreases as the frequency of the signal to be sampled increases. Nevertheless, a significant THD improvement is observed for sinusoidal signals to be sampled, at 250 MHz and 500 MHz for MI equal to 40%, 60% and 80%, and at 1 GHz and at 2 GHz for MI equal to 60%, while a tangible THD improvement is observed for the rest of frequency and MI combinations.

The quality of the sampling process depends on the signal to be sampled at the SOA-MZI input A, which acts as a reference signal and sets a hard limit on the maximum achievable performance by the SOA-MZI photonic sampler as well as on the efficiency of the post-distortion technique. Furthermore, adapting the SOAs design for specific use in an SOA-MZI photonic sampler so as to ensure stronger dependence of the SOA carrier density on the input power and higher saturation power for a wider range of acceptable input powers could also lead to performance improvements.

References

[1] D. Kastritsis, T. Rampone, M. Franco, K. E. Zoiros, and A. Sharaiha, "SOA-MZI photonic sampler with a post-distortion linearization technique," *Optics Express*, vol. 29, no. 15, pp. 23 736–23 751, Jul. 2021.

[2] D. Kastritsis, T. Rampone, K. E. Zoiros, and A. Sharaiha, "Comparison of two photonic sampling mixer architectures based on SOA-MZI for all-optical frequency up-conversion," in *Proc. 2018 IEEE International Topical Meeting on Microwave Photonics (MWP)*. Toulouse, France: IEEE, Oct. 2018, pp. 1–4.

[3] D. Kastritsis, T. Rampone, K. E. Zoiros, and A. Sharaiha, "Échantillonnage par modulation tout-optique d'un train d'impulsions courtes dans un SOA-MZI appliqué à la transposition de fréquence," presented at the Journée du Club Optique-Microondes (JCOM 2018), Toulouse, France, Jul. 2018.

[4] D. Kastritsis, K. E. Zoiros, T. Rampone, and A. Sharaiha, "SOA-MZI All-Optical RoF Signal Mixing," in *Proc. 2019 IEEE 21st International Conference on Transparent Optical Networks (ICTON)*. Angers, France: IEEE, Jul. 2019, pp. 1–4.

[5] D. Kastritsis, T. Rampone, K. E. Zoiros, and A. Sharaiha, "Technique de linéarisation pour un SOA-MZI dans un contexte d'échantillonnage tout-optique," presented at the Journée du Club Optique-Microondes (JCOM 2019), Brest, France, Jun. 2019.

[6] D. Kastritsis, T. Rampone, K. E. Zoiros, and A. Sharaiha, "Modulation and Switching Architecture Performances for Frequency Up-Conversion of Complex-Modulated Data Signals Based on a SOA-MZI Photonic Sampling Mixer," *Journal of Lightwave Technology*, vol. 38, no. 19, pp. 5375–5385, Oct. 2020.

[7] T. Rampone, A. Lagrost, A. Sharaiha, and A. Kabalan, "Optical Radiofrequency Signal Mixing by All-Optical Sampling Based on a Semiconductor Optical Amplifier Mach–Zehnder Interferometer," *Journal of Lightwave Technology*, vol. 31, no. 23, pp. 3597–3602, Dec. 2013.

[8] H. Termos, T. Rampone, A. Sharaiha, A. Hamié, and A. Alaeddine, "All-Optical Radiofrequency Sampling Mixer Based on a Semiconductor Optical Amplifier Mach–Zehnder Interferometer Using a Standard and a Differential Configuration," *Journal of Lightwave Technology*, vol. 34, no. 20, pp. 4688–4695, Oct. 2016.

[9] H. Termos, "Study of up & down conversion technique by all-optical sampling based on SOA-MZI All-optical radiofrequency sampling mixer based on a Semiconductor Optical Amplifier Mach-Zehnder Interferometer using a standard and a differential configuration," Ph.D. dissertation, École Nationale d'Ingénieurs de Brest, Brest, France, Feb. 2017.

[10] H. Termos, T. Rampone, and A. Sharaiha, "Sampling rate influence in up and down mixing of QPSK and OFDM signals using an SOA-MZI in a differential configuration," *Electronics Letters*, vol. 54, no. 16, pp. 990–991, Aug. 2018.

[11] P. W. Juodawlkis, J. C. Twichell, G. E. Betts, J. J. Hargreaves, R. D. Younger, J. L. Wasserman, F. J. O'Donnell, K. G. Ray, and R. C. Williamson, "Optically sampled analog-to-digital converters," *IEEE Transactions on Microwave Theory and Techniques*, vol. 49, no. 10, pp. 1840–1853, Oct. 2001.

[12] J. H. Wong, S. Aditya, H. Q. Lam, P. H. Lim, K. E. K. Lee, and P. S. Ping, "Linearization of an optically sampled analog-to-digital converter," in *Proc. 2012 IEEE International Topical Meeting on Microwave Photonics (MWP)*, Sep. 2012, pp. 204–207.

[13] D. Kastritsis, T. Rampone, K. Zoiros, and A. Sharaiha, "Comparison of two photonic sampling mixer architectures based on SOA-MZI for all-optical frequency up-conversion," in *Proc. 2018 IEEE International Topical Meeting on Microwave Photonics (MWP)*, Oct. 2018, pp. 1–4.

[14] I. V. Blagouchine and E. Moreau, "Analytic Method for the Computation of the Total Harmonic Distortion by the Cauchy Method of Residues," *IEEE Transactions on Communications*, vol. 59, no. 9, pp. 2478–2491, Sep. 2011.

[15] R. Zhu, "Broadband Linearization Technologies for Broadband Radio-over-Fiber Transmission Systems," Ph.D. Dissertation, Concordia University, Aug. 2015.

[16] D. Kastritsis, K. E. Zoiros, T. Rampone, and A. Sharaiha, "SOA-MZI All-Optical RoF Signal Mixing," in *Proc. 2019 IEEE 21st International Conference on Transparent Optical Networks (ICTON)*, Jul. 2019, pp. 1–4.

[17] D. Kastritsis, T. Rampone, K. E. Zoiros, and A. Sharaiha, "Modulation and Switching Architecture Performances for Frequency Up-Conversion of Complex-Modulated Data Signals Based on a SOA-MZI Photonic Sampling Mixer," *Journal of Lightwave Technology*, vol. 38, no. 19, pp. 5375–5385, Oct. 2020.

[18] P. Morel and A. Sharaiha, "Wideband Time-Domain Transfer Matrix Model Equivalent Circuit for Short Pulse Propagation in Semiconductor Optical Amplifiers," *IEEE Journal of Quantum Electronics*, vol. 45, no. 2, pp. 103–116, Feb. 2009.

Chapter 4

Semiconductor Optical Amplifier Mach-Zehnder Interferometer sampler (SOA-MZI) Photonic Sampling Mixer

In this chapter, SOA-MZI photonic sampler is investigated for the application of frequency mixing while employing both Switching and Modulation architectures. In this context, a small-signal analysis of the SOA-MZI sampler is provided where an analytical expression for the Conversion Gain (CG) is derived and a qualitative insight into the trends of CG results for the two architectures is presented. The performance in terms of CG is evaluated and the analytical expression is validated by comparison to measured CG values. The highest, compared to the state-of-the-art, CG, is achieved with the Modulation architecture of the SOA-MZI photonic mixer for up-conversion of a signal from 1 GHz to 39 GHz, which is adjacent to the 4^{th} harmonic of the mode locked laser. Moreover, the performance of up-conversion has been evaluated using Quadrature Phase Shift Keying (QPSK) and 16 states Quadrature Amplitude Modulation (16-QAM) complex modulated signals which is done for the first time for the Modulation architecture. The content of the chapter is organized as follows. In section 4.1, a small-signal analysis of the SOA-MZI sampling mixer is provided. In section 4.2, the conditions of the conducted experiments are defined and the static and CG experimental results are given. In section 4.3, the results for the frequency up-conversion of complex-modulated data are presented by comparing the two architectures against the Error Vector Magnitude (EVM). Finally, section 4.4 contains the conclusions reached in this chapter. Extended parts of this chapter are an adapted version of a publication, produced during this thesis work, in the Journal of Lightwave Technology [1] [1].

1. © 2020 IEEE. Reprinted, with permission, from [1]. IEEE does not endorse any of the additions and modifications of the published article made in the adapted version of this chapter.

4.1 Small-signal analysis of SOA-MZI sampling mixer

Small-signal analysis is a powerful analysis technique for obtaining approximate analytical solutions to a problem A small-signal analysis of the SOA-MZI sampling mixer is formulated by expressing each time-dependent parameter as the sum of a steady state term $\overline{X}$ and a first-order perturbation term δx at one or more angular frequencies [2–5]:

$$X(t) = \overline{X} + \delta x(t) \tag{4.1}$$

In our case one input is a sampling pulse train that is modeled as an infinite sum of harmonics.

4.1.1 Modeling in presence of a sampling pulse train

Using the notation of Equation (4.1) and the index $\alpha \in \{s, m\}$ to discriminate between the (s)witching and (m)odulation architectures, the power of the sampling signal can be written as the sum of the average power $\overline{P}_{ck,\alpha}$ and the perturbation term $\delta p_{cki,\alpha}$, which represents the sinusoidal variation of the i^{th} harmonic at angular frequency ω_{cki}:

$$P_{ck,\alpha}(t) = \overline{P}_{ck,\alpha} + \delta p_{cki,\alpha}(t) = \overline{P}_{ck,\alpha} + \frac{1}{2}\sum_{i\in\mathbb{N}^*}\left(p_{cki,\alpha}\, e^{j\omega_{cki}t} + p^*_{cki,\alpha}\, e^{-j\omega_{cki}t}\right) \tag{4.2}$$

Likewise, the input power of the signal to be sampled, $P_{dat,\alpha}$, is the sum of an average power $\overline{P}_{dat,\alpha}$ and a sinusoidal variation $\delta p_{dat,\alpha}$ at the angular frequency ω_{dat}:

$$P_{dat,\alpha}(t) = \overline{P}_{dat,\alpha} + \delta p_{dat,\alpha}(t) = \overline{P}_{dat,\alpha} + \frac{1}{2}\left(p_{dat,\alpha}\, e^{j\omega_{dat}t} + p^*_{dat,\alpha}\, e^{-j\omega_{dat}t}\right) \tag{4.3}$$

Figure 4.1 depicts the layout of the SOA-MZI (CIP, model 40G-2R2-ORP) used in the experiments. P_C and P_A enter the interferometric module from port C and A, while P_I and P_J emerge from ports I and J, respectively. Ports B and D have not been used in this work.

At SOA-MZI input port C, the incoming power is decomposed as:

$$P_C = \overline{P}_C + \delta p_C(t) \tag{4.4}$$

Similarly, introducing the index $k \in \{1, 2\}$ to discriminate between SOA1 and SOA2, we get the following equation for the carrier density, N_k (the SOA is modelled as a one section device):

$$N_k(t) = \overline{N}_k + \delta n_k(t) = \overline{N}_k + \frac{1}{2}\sum_{F}\left(n_{k,\omega_F}\, e^{j\omega_F t} + n^*_{k,\omega_F}\, e^{-j\omega_F t}\right) \tag{4.5}$$

where ω_F represents the linear combination of the angular frequency components of all optical signals traversing SOAk. In case of SOA1, these include the sampling signal and the signal to be sampled. In case of SOA2, only one of the two optical signals passes through, i.e. either the

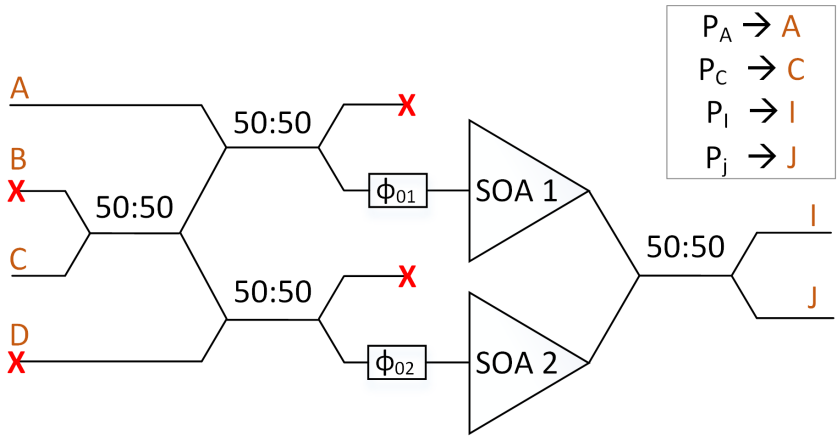

Figure 4.1: SOA-MZI layout of CIP 40G-2R2-ORP module and the name correspondence between powers and ports. Reproduced from [1] (© 2020 IEEE).

signal to be sampled, thus $\omega_F = \omega_{dat}$ for the Switching architecture, or the sampling signal, thus $\omega_F = \omega_{cki}$ for the Modulation architecture.

The SOAs time-dependent gain and phase properties can be developed as follows:

$$G_k(t) = \overline{G}_k + \delta g_k(t) = \overline{G}_k + \delta n_k(t)\frac{\partial G_k}{\partial N} \tag{4.6}$$

$$\Phi_k(t) = \overline{\Phi}_k + \delta\phi_k(t) = \overline{\Phi}_k + \delta n_k(t)\frac{\partial \Phi_k}{\partial N} \tag{4.7}$$

At SOA-MZI output port J, the optical power is given by Equation (2.49). Now applying to Equation (2.49) a first-order Taylor series approximation around $[\delta g_1, \delta g_2, \delta\phi_1, \delta\phi_2] = [0, 0, 0, 0]$ and introducing, Equations (4.6) and (4.7), we get Equation (4.8):

$$\begin{aligned} P_J(t) = \overline{P}_J + \delta p_j(t) = \frac{1}{8}\left(\overline{P}_C + \delta p_C(t)\right) \cdot \\ \cdot \left[\overline{G}_1 + \overline{G}_2 - 2\sqrt{\overline{G}_1\overline{G}_2}\,\cos(\overline{\Phi}_1 - \overline{\Phi}_2) + \left(1 - \frac{\overline{G}_2}{\sqrt{\overline{G}_1\overline{G}_2}}\cos(\overline{\Phi}_1 - \overline{\Phi}_2)\right)\delta g_1(t) + \right. \\ \left. + \left(1 - \frac{\overline{G}_1}{\sqrt{\overline{G}_1\overline{G}_2}}\cos(\overline{\Phi}_1 - \overline{\Phi}_2)\right)\delta g_2(t) + 2\sqrt{\overline{G}_1\overline{G}_2}\,(\delta\phi_1(t) - \delta\phi_2(t))\,\sin(\overline{\Phi}_1 - \overline{\Phi}_2)\right] \end{aligned} \tag{4.8}$$

Developing Equation (4.8), we get the average output power $\overline{P}_J$ and variation power δp_J:

$$\overline{P}_J = \frac{1}{8}\overline{P}_C\left(\overline{G}_1 + \overline{G}_2 - 2\sqrt{\overline{G}_1\overline{G}_2}\cos(\overline{\Phi}_1 - \overline{\Phi}_2)\right) \tag{4.9}$$

$$\delta p_J(t) = \delta p_C(t)\,\frac{\overline{P}_J}{\overline{P}_C} + \overline{P}_C\,\delta g\phi(t) + \delta p_C(t)\,\delta g\phi(t) \tag{4.10}$$

where $\delta g\phi$ is given by:

$$\delta g\phi(t) = \frac{1}{8}\Big[\delta g_1(t) + \delta g_2(t) - \sqrt{\overline{G}_1\overline{G}_2}\Big(\frac{\delta g_1(t)}{\overline{G}_1} + \frac{\delta g_2(t)}{\overline{G}_2}\Big)\cos(\overline{\Phi}_1 - \overline{\Phi}_2) + 2\sqrt{\overline{G}_1\overline{G}_2}(\delta\phi_1(t) - \delta\phi_2(t))\sin(\overline{\Phi}_1 - \overline{\Phi}_2)\Big] \quad (4.11)$$

4.1.2 Up-converted small-signal terms

Equation (4.10) for the Modulation and Switching architectures is going to be developed in the following way. Exclusively the combination of terms in (4.10) that are generating intermodulation products at frequencies $f_{cki} \pm f_{dat}$ are retained, while all other terms are eliminated. For this purpose, firstly the first term of (4.10) is eliminated since it contains no intermodulation products but only the frequencies of the input signal at port C.

Secondly, δg_2 and $\delta\phi_2$ perturbation terms induced by SOA2 are eliminated as they do not participate in the generation of $f_{cki} \pm f_{dat}$ intermodulation frequencies.

More analytically, for the Switching architecture, the only signal traversing SOA2 is P_{dat}, therefore δg_2 and $\delta\phi_2$ variations are induced at frequency f_{dat}. As a result, for the second term of (4.10), the product of δg_2 and $\overline{P}_C$ as well as the product of $\delta\phi_2$ and $\overline{P}_C$ correspond to variations at frequency f_{dat}. For the third term of (4.10), the product of δg_2 and of δp_C as well as the product of $\delta\phi_2$ and of δp_C correspond to variations at frequency $2f_{dat}$.

Similarly, for the Modulation architecture, the only signal that passes through SOA2 is P_{ck}, therefore δg_2 and $\delta\phi_2$ variations are induced at frequencies f_{cki}. As a result, for the second term of (4.10), the product of δg_2 and $\overline{P}_C$ as well as the product of $\delta\phi_2$ and $\overline{P}_C$ correspond to variations at frequencies f_{cki}. For the third term of (4.10), the product of δg_2 and δp_C as well as the product of $\delta\phi_2$ and δp_C correspond to variations at frequencies $2f_{cki}$.

Therefore, based on (4.10) and the previous analysis we can write for the intermodulation products at frequencies $f_{cki} \pm f_{dat}$:

$$\delta p_{J,cki\pm dat,\alpha} = \frac{1}{8}\Big(\overline{P}_C\,\delta g\phi_1(t) + \delta p_C(t)\,\delta g\phi_1(t)\Big) \quad (4.12)$$

where $\delta g\phi_1$ is given by:

$$\delta g\phi_1(t) = \delta g_1(t) - \frac{\sqrt{\overline{G}_1\overline{G}_2}}{\overline{G}_1}\cos(\overline{\Phi}_1 - \overline{\Phi}_2)\delta g_1(t) + 2\sqrt{\overline{G}_1\overline{G}_2}\sin(\overline{\Phi}_1 - \overline{\Phi}_2)\delta\phi_1(t) \quad (4.13)$$

Substituting δg_1, $\delta\phi_1$ from Equations (4.6) and (4.7) and δn_k from (4.5), while taking into account that $P_C = P_{dat}$ for Switching and $P_C = P_{ck}$ for Modulation architectures, the optical

powers at the up-conversion frequency $f_{cki-dat}$ are given by:

$$p_{J,cki-dat,s} = \frac{C_{OP_s}}{16}\left[p^*_{dat,s} n_{1,\omega_{cki},s} + \overline{P}_{dat,s}\, 2n_{1,\omega_{cki-dat,s}}\right] \tag{4.14}$$

$$p_{J,cki-dat,m} = \frac{C_{OP_m}}{16}\left[p_{cki,m} n^*_{1,\omega_{dat},m} + \overline{P}_{ck,m}\, 2n_{1,\omega_{cki-dat,m}}\right] \tag{4.15}$$

where $n_{1,\omega_{cki-dat},s}$ is given by expression (B.6) in the Appendix B and C_{OP_α} is a constant at a given operating point defined by:

$$C_{OP_\alpha} = \frac{\partial G_{1,\alpha}}{\partial N} - \frac{1}{\overline{G}_{1,\alpha}}\frac{\partial G_{1,\alpha}}{\partial N}\sqrt{\overline{G}_{1,\alpha}\overline{G}_{2,\alpha}}\cos(\overline{\Phi}_{1,\alpha} - \overline{\Phi}_{2,\alpha}) + 2\frac{\partial \Phi_{1,\alpha}}{\partial N}\sqrt{\overline{G}_{1,\alpha}\overline{G}_{2,\alpha}}\sin(\overline{\Phi}_{1,\alpha} - \overline{\Phi}_{2,\alpha}) \tag{4.16}$$

Equations (4.14) and (4.15) can be further simplified given that both SOAs are not operating in the high saturation region. In this case, the first term in the brackets is the most significant one, similar to [3, 6], since $n_{1,\omega_{cki-dat},\alpha}$ is a second-order perturbation term of the carrier density variation [4].

$$p_{J,cki-dat,s} \approx \frac{C_{OP_s}}{16} p^*_{dat,s} n_{1,\omega_{cki},s} \tag{4.17}$$

$$p_{J,cki-dat,m} \approx \frac{C_{OP_m}}{16} p_{cki,m} n^*_{1,\omega_{dat},m} \tag{4.18}$$

By replacing in (4.17) and (4.18) $n_{1,\omega_{cki},s}$ and $n^*_{1,\omega_{dat},m}$ by their expressions (B.10) and (B.11) given in the Appendix B, we get:

$$p_{J,cki-dat,s} = -K_s \frac{p^*_{dat,s} p_{cki,s} \overline{G}_{1,s}\tau_d}{1 + j\omega_{cki}\tau_d} \tag{4.19}$$

$$p_{J,cki-dat,m} = -K_m \frac{p^*_{dat,m} p_{cki,m} \overline{G}_{1,m}\tau_d}{1 - j\omega_{dat}\tau_d} \tag{4.20}$$

where τ_d is the SOAs differential carrier lifetime. Constant K_α with $\alpha \in \{s, m\}$ depends both on the SOAs structural parameters and the operating point of the SOA-MZI and is given by:

$$K_\alpha = \frac{\overline{G}_{1,\alpha}}{32 P_{sat}\tau_{ASE}}\left[1 - \sqrt{\frac{\overline{G}_{2,\alpha}}{\overline{G}_{1,\alpha}}}\left[\cos\left(-\frac{\alpha_H}{2}\ln\frac{\overline{G}_{1,\alpha}}{\overline{G}_{2,\alpha}}\right) + \alpha_H \sin\left(-\frac{\alpha_H}{2}\ln\frac{\overline{G}_{1,\alpha}}{\overline{G}_{2,\alpha}}\right)\right]\right] \tag{4.21}$$

A detailed development to arrive at the form of Equation (4.21) is presented in Appendix B.

4.1.3 Conversion Gain

In order to quantify the performances of the photonic microwave mixer the electrical CG, $CG_{cki-dat,\alpha}$, has been evaluated. The use of electrical CG instead of optical one permits us to easily compare the small-signal analysis results with the experimental ones. The electrical CG is defined as the ratio between the squared modulus of $p_{J,cki-dat,\alpha}$, i.e. the optical output modulation power at frequency $f_{cki-dat}$ of the optical carrier at wavelength λ_C, and the squared modulus of $p^*_{dat,\alpha}$, i.e. the optical input modulation power at frequency f_{dat}.

$$CG_{cki-dat,\alpha} = \left| \frac{p_{j,cki-dat,\alpha}}{p^*_{dat,\alpha}} \right|^2 \tag{4.22}$$

Applying (4.17) and (4.18) to (4.22), the electrical CG for the Switching and Modulation architectures is given by (4.23) and (4.24), respectively:

$$CG_{cki-dat,s} = \left| K_s \frac{p_{cki,s} \overline{G}_{1,s} \tau_d}{1 + j\omega_{cki}\tau_d} \right|^2 \tag{4.23}$$

$$CG_{cki-dat,m} = \left| K_m \frac{p_{cki,m} \overline{G}_{1,m} \tau_d}{1 - j\omega_{dat}\tau_d} \right|^2 \tag{4.24}$$

Equations (4.23) and (4.23) indicate that the CGs exhibit a low-pass filter response, whose cut-off frequency occurs at $f_{cut} = \frac{1}{2\pi\tau_d}$ [3, 7]. In case where ω_{ck1} is much higher than $\omega_{cut} = 2\pi f_{cut}$, while ω_{dat} is lower than ω_{cut}, the projection that for the Switching architecture, as the order 'i' of ω_{cki} increases, the CG will decrease rapidly following the low-pass filter response of the carrier density can be made. On the other hand, for the Modulation architecture, as 'i' increases, the CG is not subject to this drop. The derived small-signal equations show the advantage of the Modulation architecture for frequency up-conversion around higher harmonics of the sampling signal compared to the Switching one.

4.2 Conversion Gain Results

4.2.1 Experimental conditions

This section describes the experimental conditions of this work and presents the static experimental results.

The setting of the SOA-MZI operating point, which is defined by the bias current I_{SOAk} of SOAs, the center wavelength λ_{ck} of the sampling signal, the wavelength λ_{dat} of the signal to be sampled and the average input powers $\overline{P}_A$ and $\overline{P}_C$, is very critical for both architectures.

Firstly, the current I_{SOAk} is chosen to be the same for both SOAs, i.e. 360 mA. This value is somewhat lower than that used previously [8], since it helps to better control the temperature

and consequently obtain a more stable response of the SOA-MZI. Furthermore, the wavelength of the signals at the SOA-MZI inputs is selected to be the same for both architectures, so as to ensure a fair comparison between them. Therefore, the signal injected at SOA-MZI input port A and the one injected at input port C are chosen and kept fixed: λ_A at 1550 nm and λ_C at 1557.4 nm, respectively. Finally, the mean power of the signal at port C, $\overline{P}_C$, is -15 dBm.

An Optical Pulse Clock (OPC) source, which is an active mode-locked laser (Pritel model UOC-E-05-20), is driven by a Radio Frequency (RF) generator at a frequency f_{ck} equal to 10 GHz and provides an optical pulse train of 1.6 ps Full Width at Half Maximum (FWHM) pulses. It should be noted that the FWHM in this chapter is different from the one in chapter 3 which was 12.6 ps. This modification significantly alters the behavior of the SOA-MZI both in the quasi-static and in the dynamic regime. Experimentally the modification of the sampling pulses width is performed by changing the tunable filter inside OPC. The use of the tunable filter is detailed in Appendix A.

The center frequency of the Optical Band-Pass Filter (OBPF) placed at each SOA-MZI output is tuned at 1557.4 nm to select the sampled signal produced by the interferometer, while removing the optical signal centered at 1550 nm. The OBPF bandwidth is chosen to be 0.7 nm in order to filter the Amplified Spontaneous Emission (ASE) noise while permitting the harmonics needed for the 39 GHz up-conversion to pass.

The phase-shifters ϕ_{01} and ϕ_{02} in the two arms of the SOA-MZI and the polarization controller (PC2) placed in the path of port C are adjusted so that the optical power at output port J is minimum for both architectures when there is no power at input port A.

Secondly, in order to find the $\overline{P}_A$ power that provides the highest possible linearity, a quasi-static characterization with pulses is performed for both architectures. The procedure is similar to the quasi-static characterization of Modulation architecture in chapter 3 with the difference that the FWHM of the pulses is 1.6 ps in this setup instead of 12.6 ps in chapter 3. This new characterization incorporates the dynamics and the behavioral changes caused to the SOA-MZI response by the utilization of pulses of reduced FWHM compared to chapter 3 case for Modulation architecture and completes it with a quasi-static characterization of Switching architecture.

The different principle of operation between Switching and Modulation architectures is the reason for the change of the device that performs the output measurement in the quasi-static regime. For the Switching architecture, OPC switches on and off a Continuous Wave (CW) signal, and thus reproduces its frequency content, albeit filtered, at the output through Cross-Phase Modulation (XPM). In order to faithfully observe the effect of XPM in RF frequencies, an Electrical Spectrum Analyzer (ESA) is used to measure the reproduced content at 10 GHz in the electric domain. For Modulation architecture, a CW signal modulates the OPC signal. In order to observe the effect of XPM in a CW signal, an optical Power Meter (PM) measuring the average output power is sufficient, as there are no reproduced frequencies at the output in the

quasi-static regime.

The experimental setup of this quasi-static characterization for the Switching architecture is shown in Figure 4.2. A CW laser source provides a constant signal at the optical carrier λ_C = 1557.4 nm, whose power is set by an optical attenuator (Att1) at $P_C(t) = \overline{P}_C$ = -15 dBm at SOA-MZI input port C. The average power $\overline{P}_A$ is controlled by Att2. At both SOA-MZI inputs A and C, powers $\overline{P}_A$ and $\overline{P}_C$ are monitored by (PM1) and by an Optical Spectrum Analyzer (OSA), respectively, through the 10% output ports of a pair of 90%-10% couplers at each input. At the SOA-MZI output using a 2X1 switch the power of ports I and J is alternately filtered by the OBPF which is tuned at wavelength λ_C with a bandwidth of 0.7 nm as previously mentioned. Subsequently, the optical power is converted to the electrical domain by a 75 GHz PIN photodiode whose responsivity is 0.71 A/W. The electrical output signal is then amplified by a 33 dB low noise amplifier (AMP 1). Finally, the electrical power at 10 GHz is measured by an ESA while the average power of the optical carrier, $\overline{P}_A$, centered at λ_A = 1550 nm is swept.

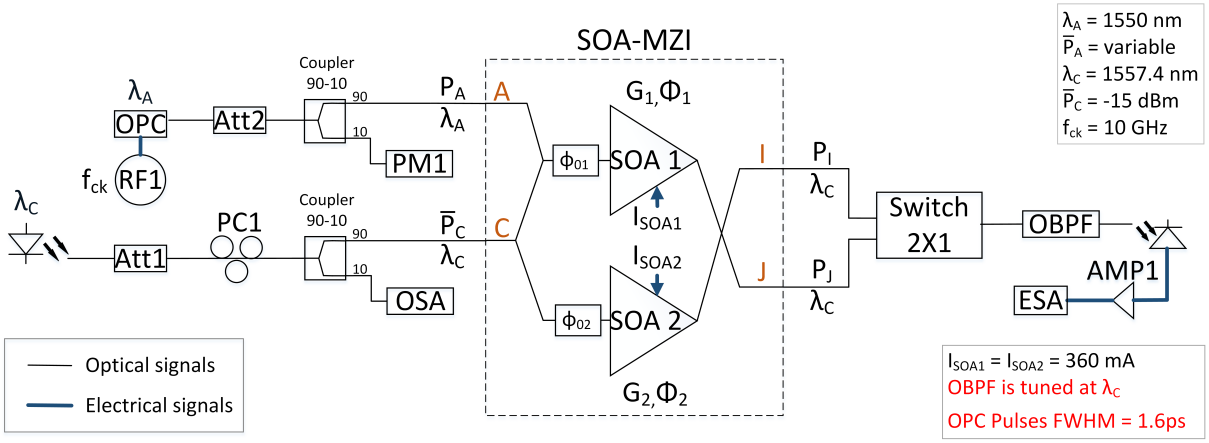

Figure 4.2: Experimental setup for the quasi-static characterization with pulses of Switching architecture. OPC: Optical Pulse Clock. RF: Radio Frequency generator. Att: Optical Attenuator. PC: Polarization Controller. PM: Optical Power Meter. OSA: Optical Spectrum Analyzer. OBPF: Optical Bandpass Filter. AMP1: Electrical Low Noise Amplifier. ESA: Electrical Spectrum Analyzer. Reproduced from [1] (© 2020 IEEE).

Afterwards, the second derivative (SD) of the optical modulation power (OMP) of the signal at 10 GHz at SOA-MZI output ports I and J is calculated from a 5th order polynomial data fitting with respect to the average optical power, $\overline{P}_A$, as shown in Figure 4.5. OMP is defined as the optical equivalent of electrical power in a specific frequency (in this case at 10 GHz) given by Equation (B.17) in Appendix B. When the second derivative of OMP is zero, the first derivative is in turn constant and so the SOA-MZI response is linear. The linearity of the operating point is important as it is associated to lower distortion of the sampled signal and therefore of the

up-converted signal. The $\overline{P}_A$ power used for conducting the measurements that follow is chosen close to the curves' intersection point in Figure 4.5 and amounts to 0.114 mW (≈ -9.5 dBm). The point where the curves of port J and port I pass closer to zero is at 0.141 mW (≈ -8.5 dBm) and 0.126 mW (≈ -9 dBm), respectively. Although a different choice for $\overline{P}_A$ either at ≈ -8.5 dBm or ≈ -9 dBm would possibly change the results by a limited amount, the intersection point is chosen in order to retain the possibility to compare the results of the two ports with the same initial conditions of low linearity.

A photo of the experimental bench during the CG measurements is shown in Figure 4.3 where some of the laboratory devices are identified.

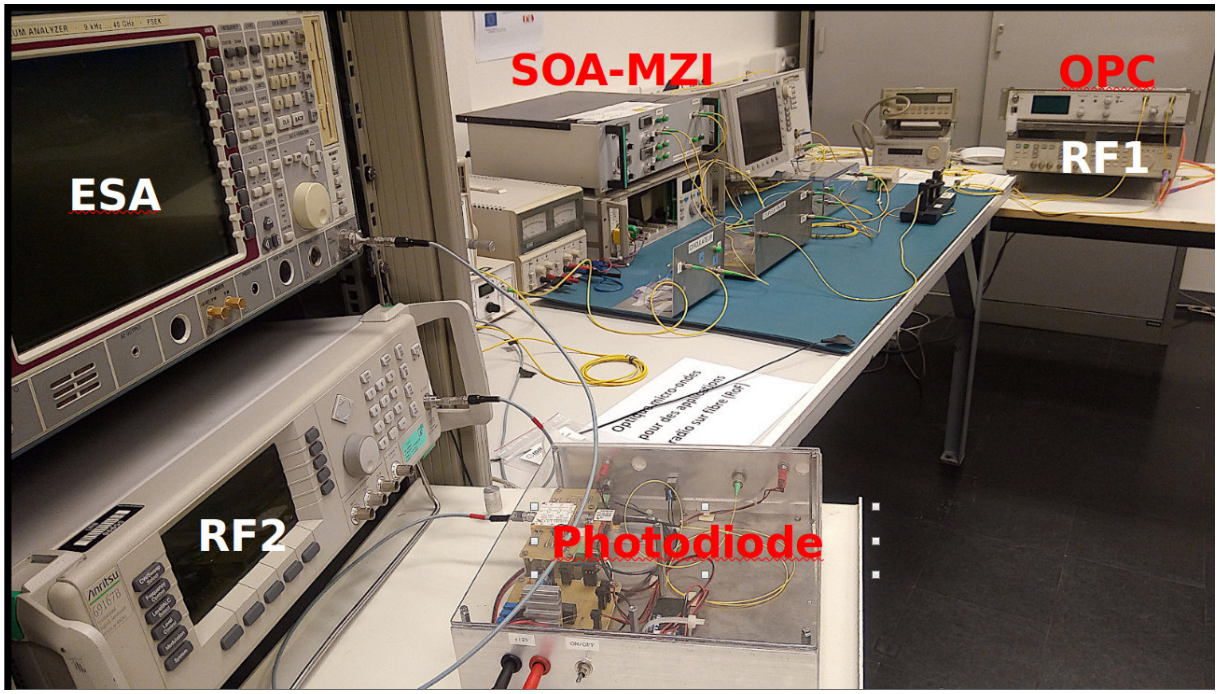

Figure 4.3: Photo of the experimental bench during conversion gain measurements. Some devices used in the experiments such as the ESA, RF1, RF2, OPC, the photodiode and the SOA-MZI are identified.

The experimental setup of this quasi-static characterization for the Modulation architecture is shown in Figure 4.4. In this characterization, the OPC source generates a signal at $\lambda_C = 1557.4$ nm, whose average power is adjusted by Att1 at $\overline{P}_C$ = -15 dBm at SOA-MZI input port C. A CW laser source provides a signal at the optical carrier $\lambda_A = 1550$ nm, whose power is controlled by Att2. At both SOA-MZI inputs A and C, powers $\overline{P}_A$ and $\overline{P}_C$ are monitored by OSA and PM1, respectively, through the 10% output ports of a pair of 90%-10% couplers at each input. At the SOA-MZI output using a 2X1 switch, the power of ports I and J is alternately filtered by the OBPF which is tuned at λ_C. Finally, for the quasi-static characterization of modulation

architecture the optical power is measured by PM2 while power $\overline{P}_A$ at $\lambda_A = 1550$ nm is swept.

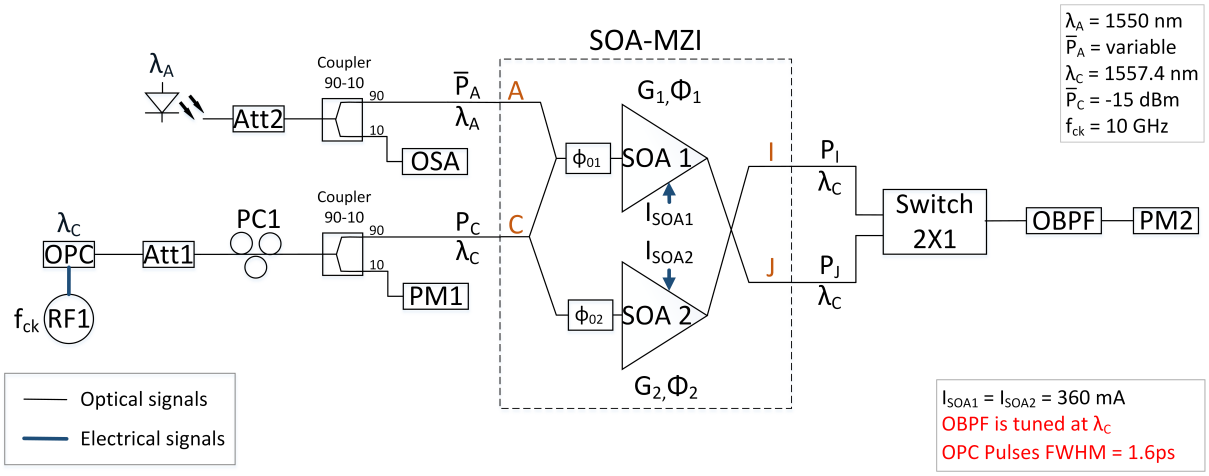

Figure 4.4: Experimental setup for the quasi-static characterization with pulses of Modulation architecture. Reproduced from [1] (© 2020 IEEE).

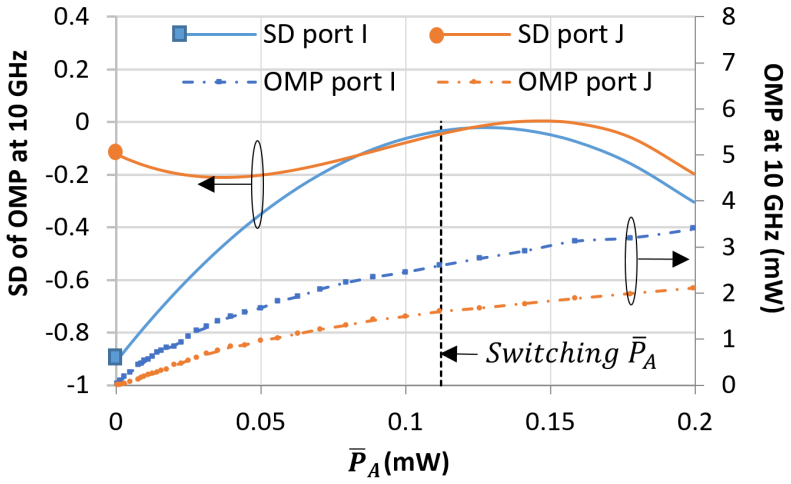

Figure 4.5: Optical Modulation Power (OMP) (right) and its Second Derivative (SD) (left) at 10 GHz at SOA-MZI output ports I and J as a function of the optical power at input port A. Reproduced from [1] (© 2020 IEEE).

According to Figure 4.6, the point at which the SD of the SOA-MZI output power at port J crosses zero occurs at 0.04 mW (-14 dBm), which hence is chosen as the $\overline{P}_A$ power for the measurements taken below with the Modulation architecture.

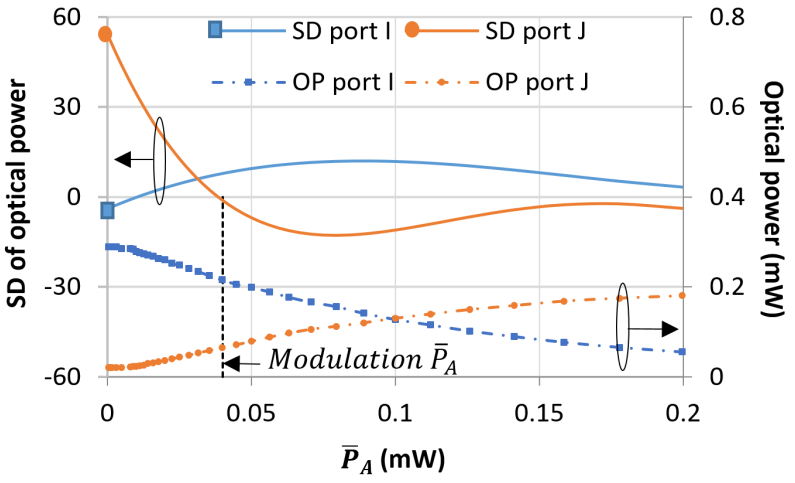

Figure 4.6: Optical power (right) and its Second Derivative (SD) at SOA-MZI output ports I and J as a function of the optical power at input port A. Reproduced from [1] (© 2020 IEEE).

Switching architecture electrical spectra of the pulsed signal at input A and output signal at port J after optical filtering are depicted in Figure 4.7. Also, Modulation architecture electrical spectra of the pulsed signal at input C and the output signal at port J after optical filtering are depicted in Figure 4.8. The measurements are made in an ESA after photodetection and amplification (AMP1). It can be observed that for Switching architecture the power difference between the 10 GHz and 40 GHz frequency components is 3 dB at the SOA-MZI input and 20 dB at the SOA-MZI output after optical filtering, whereas for Modulation architecture is 6 dB at the SOA-MZI input and 10 dB at the SOA-MZI output after optical filtering. The power difference between the SOA-MZI input and output after optical filtering is significantly higher for the Switching architecture than for the Modulation architecture due to the limited carrier lifetime of the SOA, as explained in 3.2. Also, a part or even the entire difference between the SOA-MZI input and output for Modulation architecture (and to a much lesser degree for Switching architecture) is due to the optical filtering by OBPF at the output of the SOA-MZI.

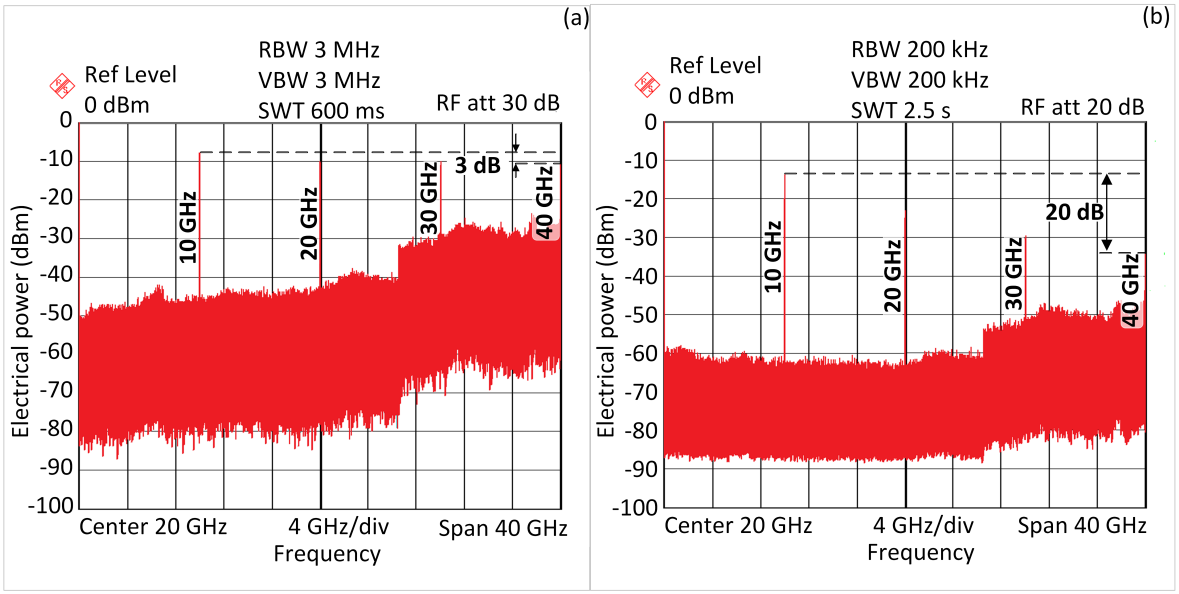

Figure 4.7: Electrical spectra of the pulsed signal at input A (a) and the SOA-MZI output port J (b) for $P_C(t) = \overline{P}_C$. The difference of spectral component between the first harmonic at 10 GHz and the fourth harmonic at 40 GHz is 3 dB.

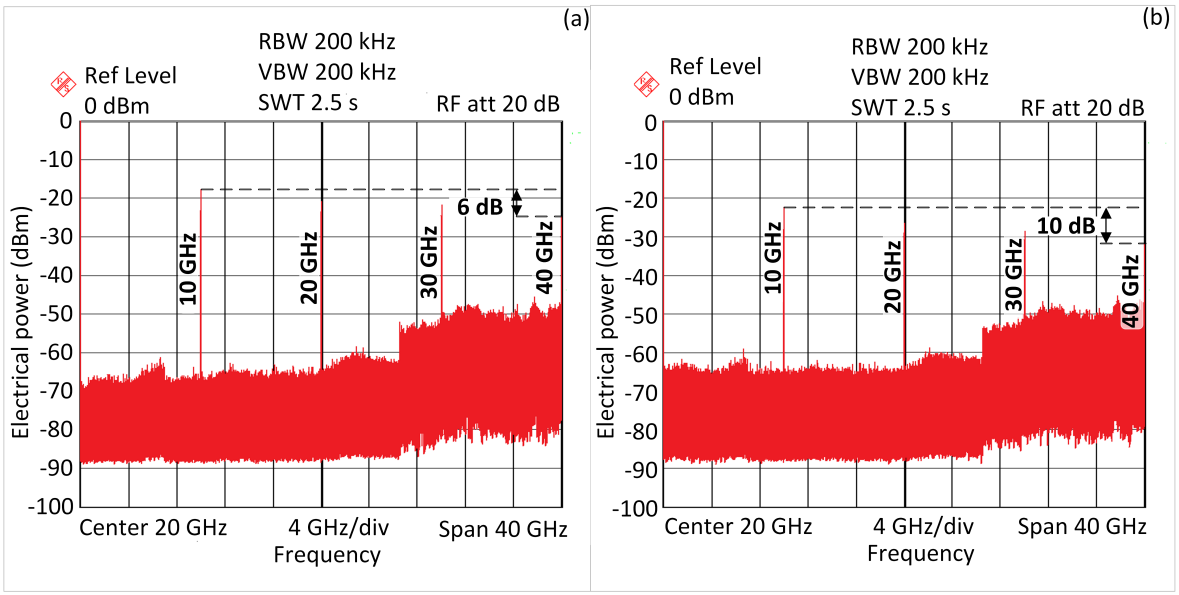

Figure 4.8: Electrical spectra of the pulsed signal at input C (a) and the SOA-MZI output port J (b) for $P_A(t) = \overline{P}_A$. The difference of spectral component between the first harmonic at 10 GHz and the fourth harmonic at 40 GHz is 6 dB.

4.2.2 Conversion Gain Estimation and Measurement

The CG has been calculated using the small-signal Equations (4.23) and (4.24) and subsequently has been measured for the frequency up-conversions from $f_{dat} = 1$ GHz to $f_{ck} - f_{dat} = 9$ GHz (CG_{9GHz}) and to $4f_{ck} - f_{dat} = 39$ GHz (CG_{39GHz}).

The experimental setup used to measure the CG is shown in Figure 4.9 and Figure 4.10 for the Switching and Modulation architectures, respectively. An example of the optical spectrum of the sampling signal produced by the OPC and the sampled signal at the 10% output port of the 10-90 output coupler are shown for the Switching architecture in Figure 4.11 and in Figure 4.12, respectively, while for the Modulation architecture are shown in Figure 4.13 and in Figure 4.14, respectively.

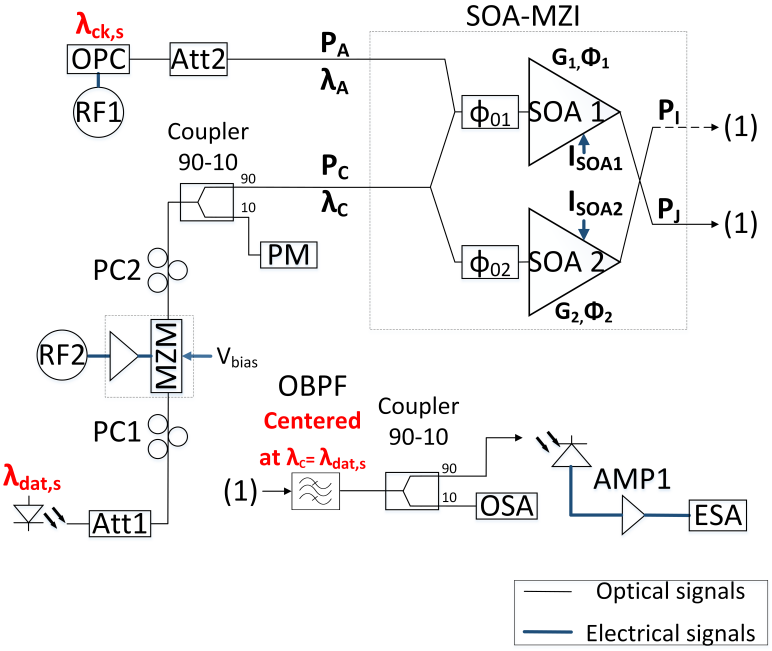

Figure 4.9: CG measurement setup for Switching architecture. (1) denotes the direction of transmission from SOA-MZI output ports I and J alternately to the ESA. Reproduced from [1] (© 2020 IEEE).

The signal to be up-converted is produced for both architectures by a CW laser source that is intensity modulated by an MZM, which is driven by an RF generator RF2 at $f_{dat} = 1$ GHz through the MZM driver module which amplifies it by 23 dB. The MZM operates in the quadrature point and the V_{bias} is 2.9 V. This optically carried RF signal is then frequency converted around f_{cki} frequencies. The optical signal emerging from the SOA-MZI I and J outputs is optically filtered by the previously mentioned OBPF. The filtered optical signal is monitored in an Optical Spectrum Analyzer (OSA) using the 10% port of a 90/10 coupler.

From the 90% port of the coupler, the signal is subsequently photodetected by the 75 GHz PIN photodiode. The combined optical loss of the OBPF and the coupler (90% output) is 7.5 dB. The electrical output signal is then amplified by the AMP 1.

The CG is defined as the difference between the electrical power in dBm referenced at the SOA-MZI output at $f_{cki} - f_{dat}$, and the electrical power in dBm referenced at the SOA-MZI input at f_{dat}.

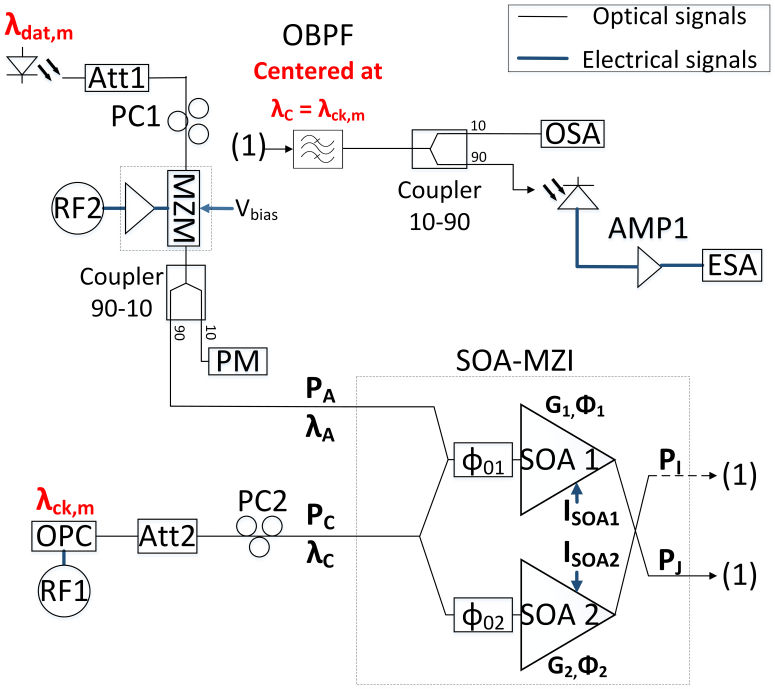

Figure 4.10: CG measurement setup for Modulation architecture. (1) denotes the direction of transmission from SOA-MZI output ports I and J alternately to the ESA. Reproduced from [1] (© 2020 IEEE).

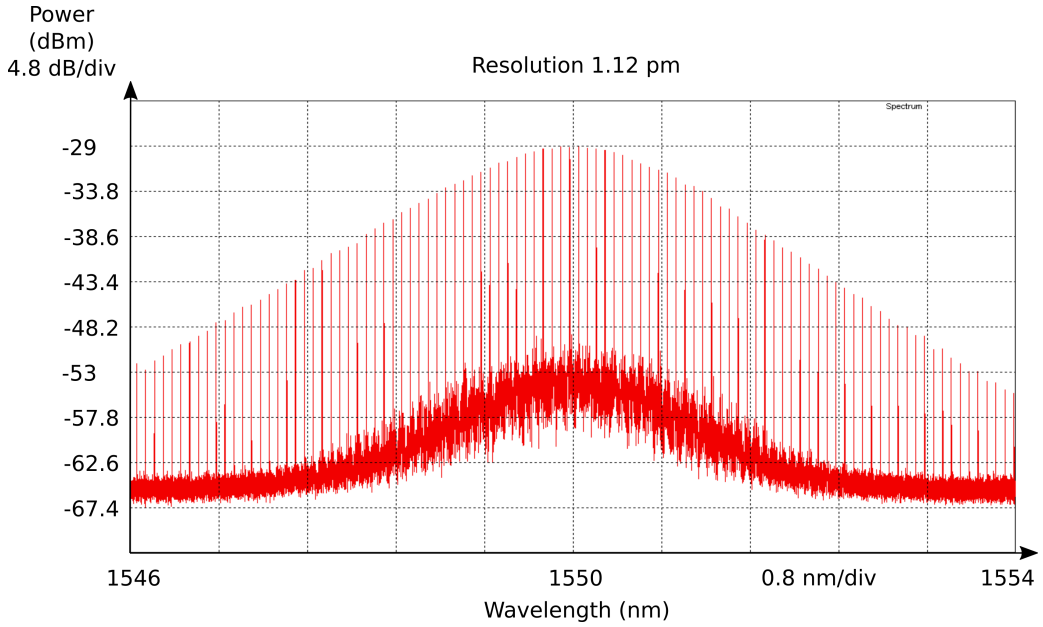

Figure 4.11: Optical spectrum of sampling signal produced by the OPC for the Switching architecture.

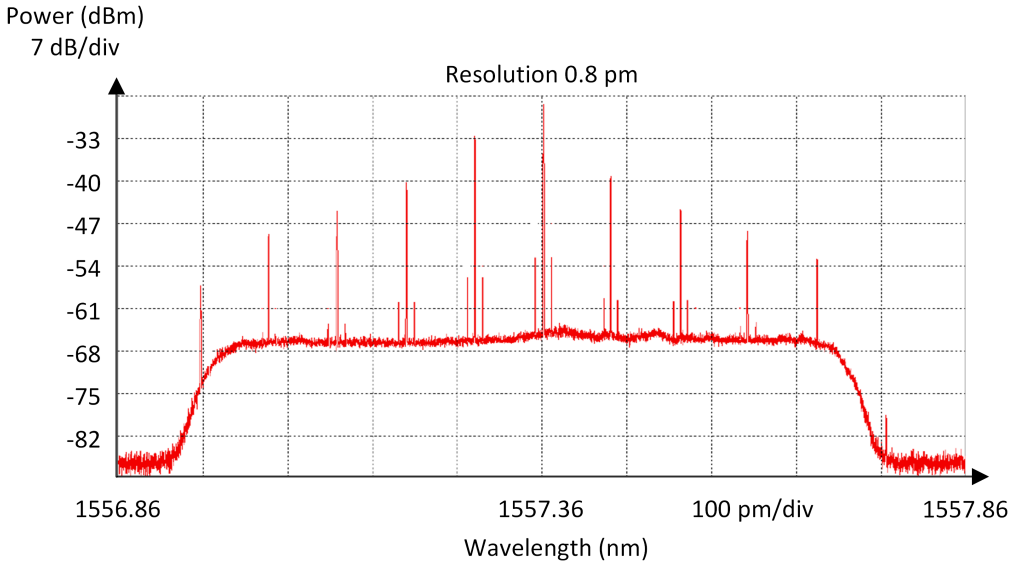

Figure 4.12: Optical spectrum of the filtered sampled signal at the 10% output port of the 10-90 output coupler for the Switching architecture. Reproduced from [1] (Copyright 2020, IEEE).

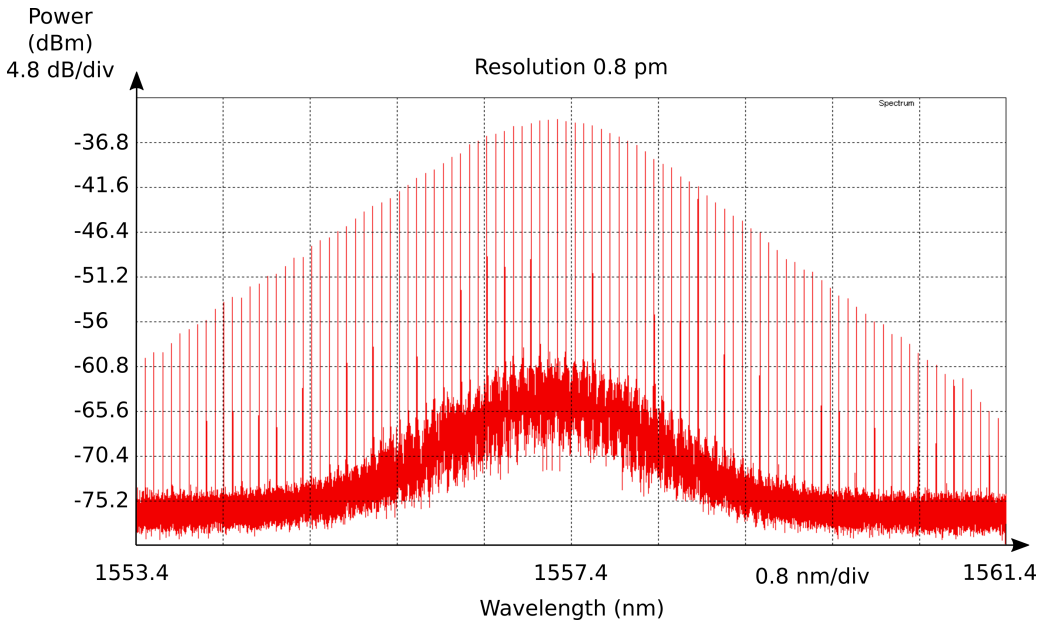

Figure 4.13: Optical spectrum of sampling signal produced by the OPC for the Modulation architecture.

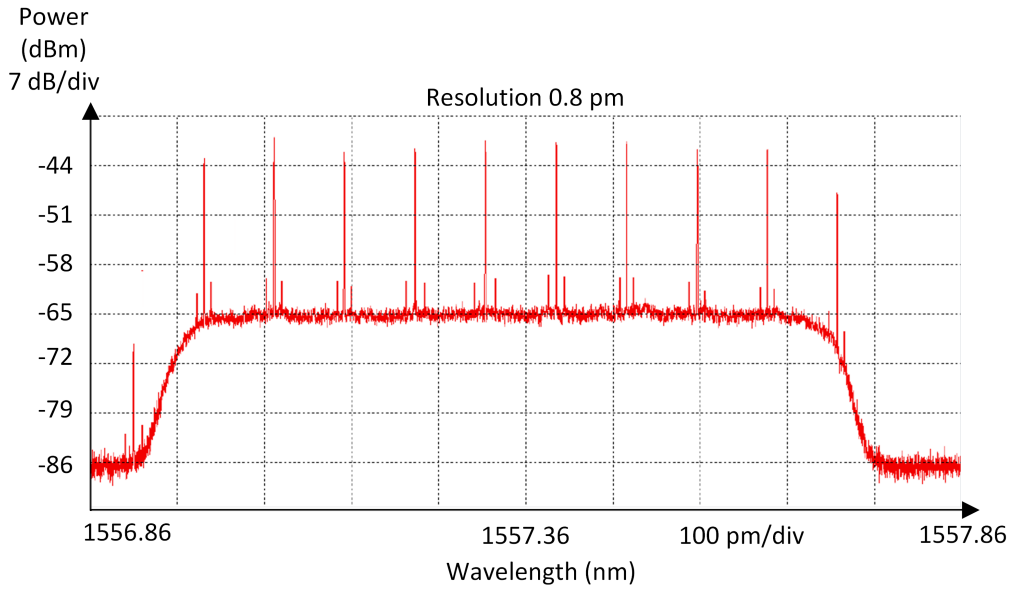

Figure 4.14: Optical spectrum of the filtered sampled signal at the 10% output port of the 10-90 output coupler for the Modulation architecture. Reproduced from [1] (© 2020 IEEE).

In Figure 4.15 the measured CG is displayed for various modulation index values of the sinusoidal signal to be sampled. Moreover, in dash-dot lines the theoretically predicted CG

derived using (4.23) and (4.24) is shown and the involved parameters values are listed in Table B.1 in Appendix B. For the Modulation architecture the only parameter that changes in (4.24) between the different up-converted signals is the power of the sampling signal harmonics, $p_{cki,m}$.

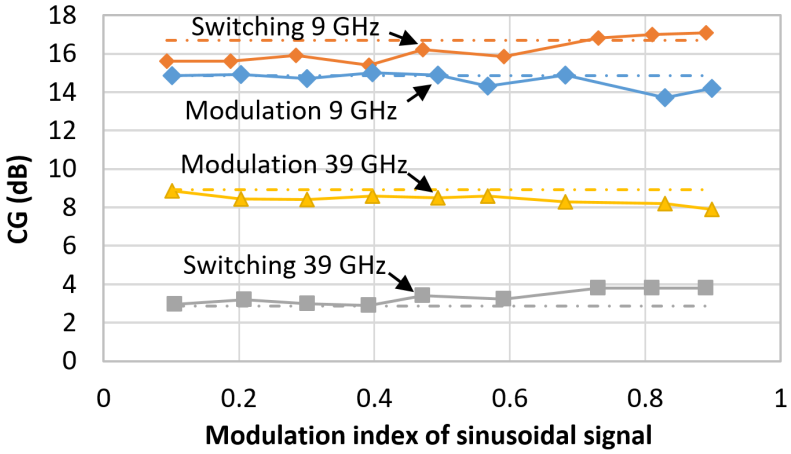

Figure 4.15: Comparison between CG of the Switching and Modulation architectures: Measured (solid lines) and theoretically calculated (dash-dot lines) CG values for frequency up-conversion at 9 GHz and 39 GHz as a function of the modulation index of P_{dat}. Reproduced from [1] (© 2020 IEEE).

There are two reasons behind the CG difference between the two architectures. The first reason is that the operating point is different between the Switching and Modulation architectures as $\overline{P}_A$ is -9.5 dBm for the former and -14 dBm for the latter. The second reason stems from the fact that since the sinusoidal signal to be sampled has been interchanged with the mode-locked sampling signal at the input of the SOA-MZI, the frequency components that participate in the $f_{dat} = 1$ GHz to $f_{ck1-dat} = 9$ GHz frequency conversion are lightly filtered by the SOA-MZI for the Switching architecture as f_{ck} at 10 GHz lies outside the XPM bandwidth ($f_{cut} = 6$ GHz, given in the Appendix B), whereas they are not filtered for the Modulation architecture as f_{dat} at 1 GHz lies inside the XPM bandwidth. However, this advantage of Modulation compared to the Switching architecture disappeared due to the use of different operating points by the two architectures and finally CG_{9GHz} turns out to be somewhat higher for Switching than for the Modulation architecture. At $f_{ck4-dat} = 39$ GHz the frequency components that participate in the $f_{dat} = 1$ GHz to $f_{ck4-dat} = 39$ GHz frequency conversion are strongly filtered by the SOA-MZI for the Switching architecture as $4f_{ck}$ at 40 GHz lies outside the XPM bandwidth, whereas they are not filtered for the Modulation architecture as $f_{dat} = 1$ GHz lies inside the XPM bandwidth. Unlike for CG_{9GHz}, for CG_{39GHz}, the more advantageous operating point of Switching architecture is not enough to compensate for the superiority of Modulation architecture caused by the overwhelming difference in filtering of the aforementioned frequency components. This

explains the increased robustness of the Modulation scheme against the Switching scheme with respect to CG as the up-conversion frequency increases.

Figure 4.15 shows a good agreement between measured and theoretically calculated GC curves, which confirms the validity and accuracy of the theoretical approach and of its outcomes. Furthermore, it highlights the usability of (4.23) and (4.24) in the design, characterization and optimization of the SOA-MZI photonic mixer. The difference in CG between the frequency conversion to 9 GHz and 39 GHz is smaller for the Modulation architecture than for the Switching one. Therefore, although CG is higher for the frequency conversion to 9 GHz when employing the Switching architecture, it is more advantageous to employ the Modulation architecture for the frequency conversion to 39 GHz. Moreover, the CG attained by the SOA-MZI photonic mixer does not change significantly with the modulation index variation. Equations (4.23) and (4.23) support this fact as CG is not a function of $p_{dat,\alpha}$, which in turn is proportional to the modulation index, i.e. $p_{dat,a} = m_{dat,\alpha}\ \overline{P}_{dat,\alpha}$, where $m_{dat,\alpha}$ is the modulation index of the sinusoidal signal.

4.2.3 Conversion Gain analysis using small signal equations

Since the small signal analysis is validated, it can be used to make a theoretical analysis which comprises predictions of the CG for the frequency conversions from $f_{dat} = 1$ GHz to a multitude of frequencies at $f_{cki} - f_{dat}$, as well as investigate the influence of the SOAs critical parameters on the CG.

In this framework, CG is calculated for frequency up-conversions from a signal at $f_{dat} = 1$ GHz to signals at frequencies up to 81 GHz in Figure 4.16. For the CG calculation the values of $p_{cki,\alpha}$ are based on measurements for $p_{cki,\alpha}$ with $i \in \{1, 2, 3, 4\}$ while they are approximated for $p_{cki,\alpha}$ with $i \in \{5, 6, 7, 8\}$, supposing a constant attenuation for the 5th, 6th, 7th and 8th OPC harmonics equal to the average of the attenuation between the first 4 OPC harmonics. The outline of the points, where an approximated value is used, is dashed and in red color. All involved parameters values are listed in Table B.1 in Appendix B.

We observe in Figure 4.16 that the Modulation architecture provides higher CG values compared to the Switching architecture for all frequency conversions except for the one to 9 GHz. Also, the CG difference between the Modulation and Switching architectures increases from -1.77 dB to 6.82 dB as the frequency of up-converted signal increases from 9 GHz to 69 GHz while it rests approximately constant and equal to 6.6 dB for the frequency up-conversion to 79 GHz. Moreover, the CG of Modulation architecture is positive for all frequency conversions except for the one at 79 GHz where it is slightly negative (-0.42 dB).

Furthermore, with respect to the SOA-MZI parameters influence on CG, from Equation (4.23), Equation (4.24) and Equation (4.21), the electrical CG is observed to be inversely proportional to the square of the saturation power, P_{sat}, and to the spontaneous carrier lifetime

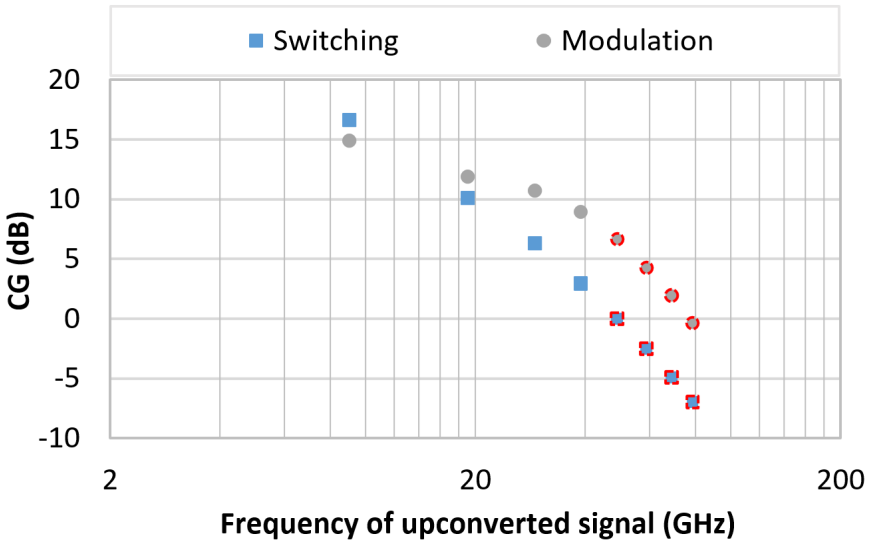

Figure 4.16: Comparison between theoretically calculated CG values of the Switching and Modulation architectures for frequency Up-conversions from $f_{dat} = 1$ GHz to $f_{cki} - f_{dat}$ with $i \in \{1, 2, 3, 4, 5, 6, 7, 8\}$. The outline of the points, where an approximated value of $p_{cki,\alpha}$ is used, is dashed and in red color.

τ_{ASE}, both of which depend on the SOA physical properties [6]. Additionally, it should be remarked, considering the other parameters constant (including the ratio $\frac{\overline{G}_{1,\alpha}}{\overline{G}_{2,\alpha}}$), that CG is proportional to the 4th power of $\overline{G}_{1,a}$, meaning that an increase of the $\overline{G}_{1,a}$ by 1 dB causes a 4 dB CG increase. In the same framework, an increase of $p_{cki,\alpha}$ or K_α by 1 dB produces a 2 dB CG increase. Moreover, varying α_H between 1 and 10 while keeping the SOAs average gains, SOAs average phases, P_{sat}, τ_{ASE}, τ_d constant i.e. keeping the operating point and the rest of key parameters constant, we obtain Figure 4.17. In this, we observe that there is an interest in using SOAs with high α_H values since the higher the α_H value, the more efficient the frequency conversion in terms of CG. The CG improvement is almost equal between the Switching and Modulation architectures. In addition, varying τ_d between 1 ps and 100 ps while keeping the SOAs average gains, phases, the rest of the key parameters as well as the ratio τ_d/τ constant, we obtain Figure 4.18. In this, we observe that using SOAs with lower τ_d values causes an increase of CG for the Switching architecture, while its influence is almost zero for the Modulation architecture. This is explained by the fact that for Modulation architecture the signal at $f_{dat} = 1$ GHz that contributes to the frequency conversions is not significantly filtered by XPM, so that an increase of τ_d and thus of XPM bandwidth provides no benefit in terms of CG. On the other hand, the frequency components of OPC that contribute to the frequency conversions i.e., f_{ck1} and f_{ck4} are filtered heavily by XPM, so that an increase of τ_d and thus of XPM bandwidth provides a serious benefit in terms of CG.

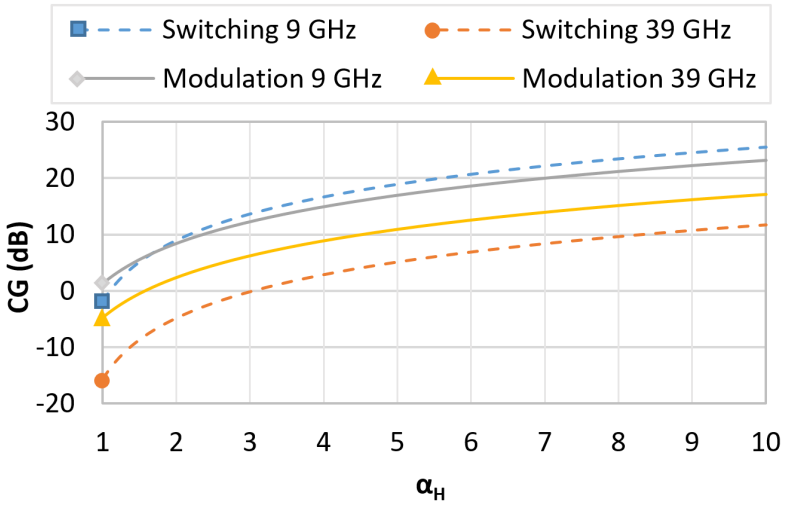

Figure 4.17: Comparison between theoretically calculated CG values of the Switching and Modulation frequency up-conversion at 9 GHz and 39 GHz as a function of α_H.

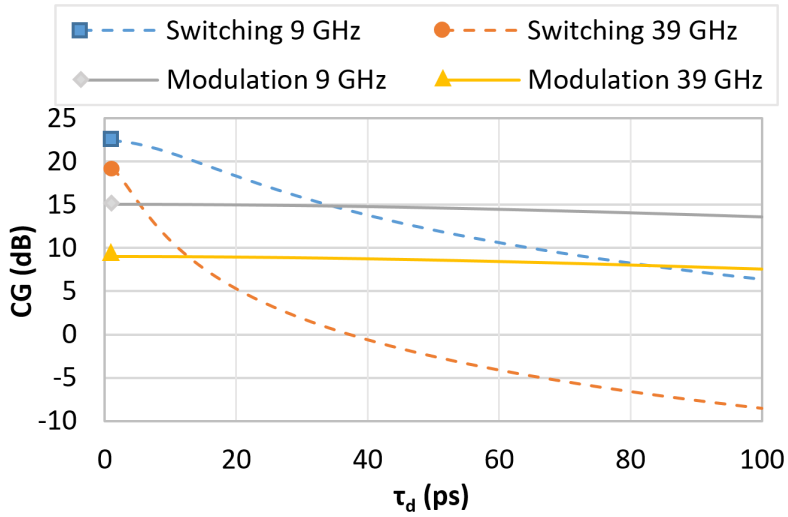

Figure 4.18: Comparison between theoretically calculated CG values of the Switching and Modulation frequency up-conversion at 9 GHz and 39 GHz as a function of τ_d.

The above analysis of the influence of critical SOA parameters on the CG is a simplified approach and although it is useful to show the most significant parameters effect on CG, the amount of CG variation that a specific parameter's change would produce in a real SOA-MZI, is a rough estimate. In a real SOA-MZI, $\overline{G}_{1,\alpha}$, τ_d, K_α, $p_{cki,\alpha}$, P_{sat} and τ_{ASE} are interdependent and associated to the SOA-MZI operating condition. Therefore the effect of each critical SOA-MZI parameter depends in any case on the exact operating point of the SOA-MZI.

4.3 Up-conversion of complex-modulated data

4.3.1 QPSK and 16-QAM modulation formats

QPSK (Quadratic Phase Shift Keying) and 16-QAM (Quadratic Amplitude Modulation) modulation formats are used for the purpose of evaluating the quality of frequency up-conversion in terms of Error Vector Magnitude (EVM).

QPSK is a form of Phase Shift Keying with 4 states (4-PSK). The constellation diagram of QPSK with Grey coding is shown in Figure 4.19 [9]. A QPSK modulation uses 4 symbols of the same amplitude A. Every symbol in the constellation diagram conveys 2 bits of information. A QPSK signal can be written by:

$$s_i(t) = A\cos(2\pi f_{dat} + \phi_i) \tag{4.25}$$

where A is the symbols' amplitude, f_{dat} is the carrier frequency, $\phi_i = (2i+1)\frac{\pi}{4}$, $i \in \{0,1,2,3\}$ is the i^{th} symbol phase.

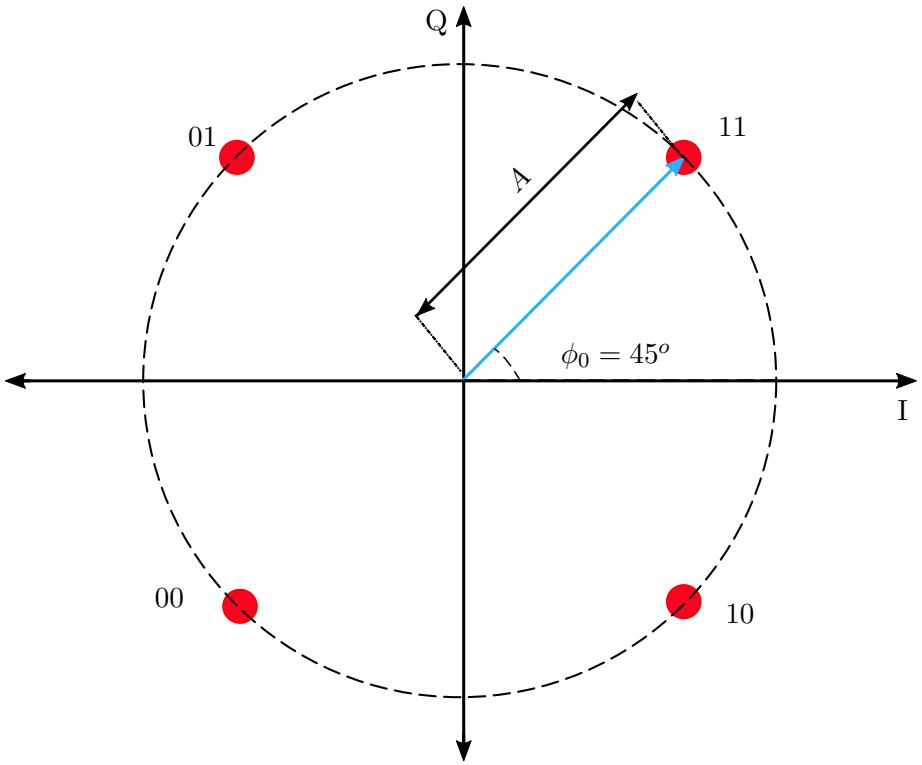

Figure 4.19: Constellation diagram of QPSK modulation format with Gray coding

QAM is a modulation format that combines amplitude and phase variations of the carrier. The constellation diagram of a QAM modulation format of 16 states (square 16-QAM) with Grey coding is shown in Figure 4.20 [9]. A 16-QAM modulation uses 16 symbols. Every symbol

in the constellation diagram conveys 4 bits of information. A 16-QAM signal is the sum of two carriers of same frequency, f_{dat}, with a phase difference between them equal to $\pi/2$. One is customarily referred to as the in-phase component, denoted by $I(t)$, and the other is referred as the quadrature component, denoted by $Q(t)$.

$$s_i(t) = I_i(t)\sin(2\pi f_{dat}t) + Q_i(t)\cos(2\pi f_{dat}t) \tag{4.26}$$

where $Q_i, I_i \in \{-3A, -A, A, 3A\}$

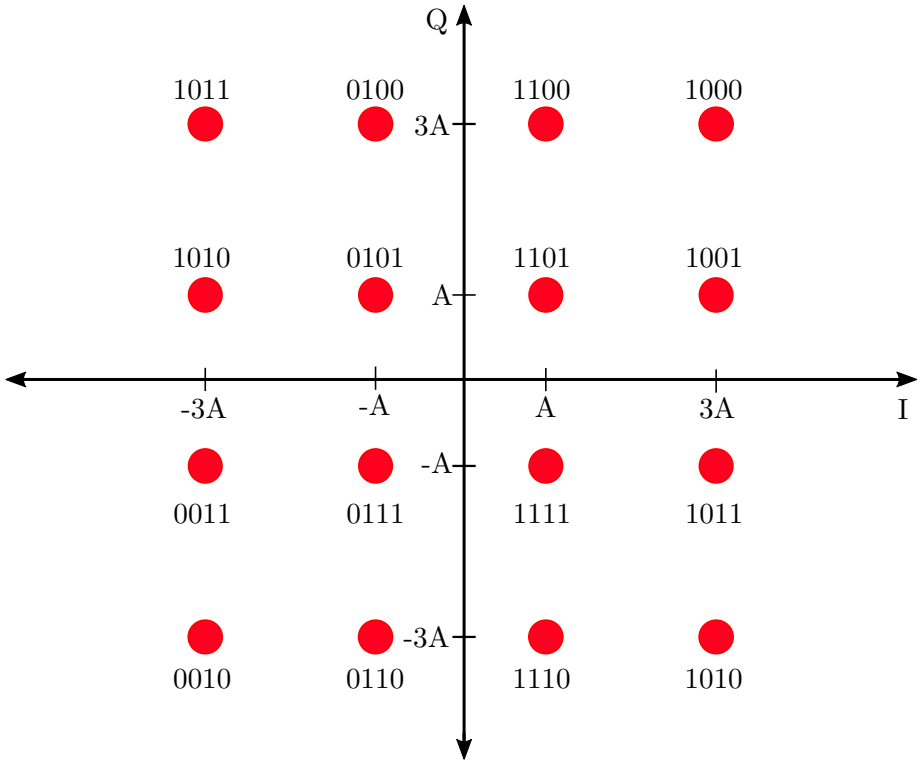

Figure 4.20: Constellation diagram of 16-QAM modulation format with Gray coding

Experimentally, the QPSK and 16-QAM modulated signals are filtered by a root raised cosine filter (RRC). In this case, the bandwidth, BW, of the modulated signal in the pass-band is defined as the frequency range of the non-zero portion of its spectrum, and with respect to the symbol rate (SR) is given by:

$$BW = (1 + \alpha)SR \tag{4.27}$$

where α is roll-off coefficient and SR is half of the bit rate (BR) for QPSK and a quarter of the bit rate for 16-QAM.

4.3.2 Error Vector Magnitude

EVM is a metric that is used to quantify the performance of a digital radio transmitter or receiver. EVM is related to the error vector which is the vector difference in the I-Q plane between the reference signal and the measured signal as shown in Figure 4.21 The definition of

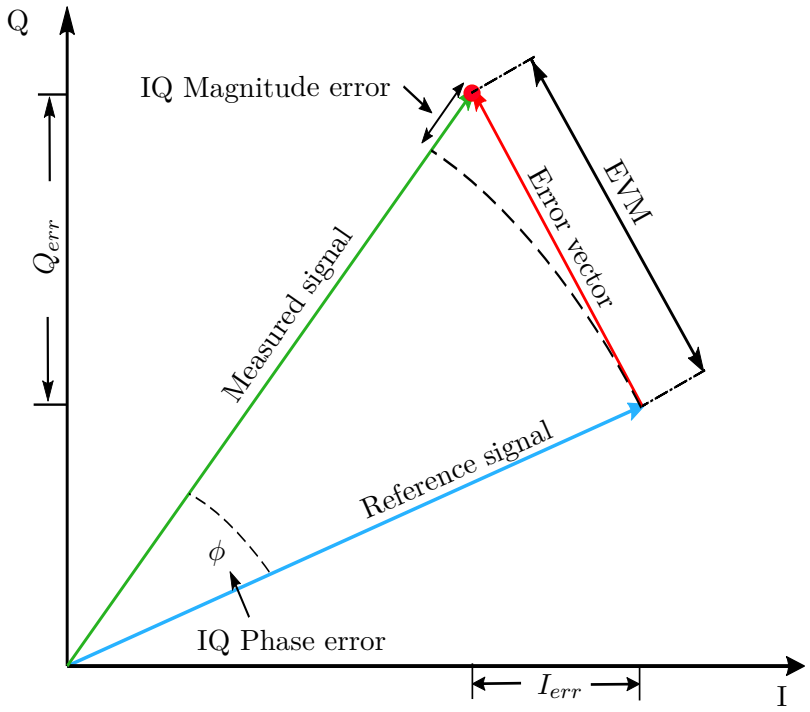

Figure 4.21: Definition of error vector and its coordinates in the IQ plane, I_{err} and Q_{err}.

EVM in percentage used in this thesis is given by the following expression [10]:

$$EVM = \frac{\sqrt{\frac{1}{N}\sum_{n=0}^{N-1}(I_{err}^2[n] + Q_{err}^2[n])}}{A_{max}} \cdot 100\% \tag{4.28}$$

where $[n]$ is the symbol index, N is the number of symbols and A_{max} is the maximum constellation amplitude of the reference signals or symbols.

It should be noted that in this definition of EVM, the maximum constellation magnitude of the reference signals is used for EVM normalization and not the average power of all reference signals of the constellation used sometimes in other works.

EVM can be estimated from the SNR, in the case where the errors are mainly due to white

noise, through the following equation [11]:

$$EVM \approx \frac{1}{k\sqrt{10^{\frac{SNR}{10}}}} \tag{4.29}$$

where the value of factor k depends on the modulation format and is equal to 1 for QPSK and equal to $3/\sqrt{5}$ for 16-QAM. SNR is in logarithmic scale (dB).

EVM is related to the Bit Error Ratio (BER) through the following expression [11]:

$$BER \approx \frac{1 - L^{-1}}{log_2 L} \cdot erfc\left[\sqrt{\frac{3log_2 L}{L^2 - 1} \cdot \frac{\sqrt{2}}{k^2 EVM^2 log_2 M}}\right] \tag{4.30}$$

where $erfc[.]$ is the Gaussian complementary error function, L is the number of signal levels identical within each dimension of the quadratic constellation and $log_2 M$ is the number of bits encoded into each symbol. L is equal to 4 for QPSK and equal to 12 for 16-QAM. $log_2 M$ is equal to 2 for QPSK and equal to 4 for 16-QAM.

4.3.3 Experimental results

The experimental setup of the SOA-MZI photonic frequency up-converter using complex modulation formats is shown in Figure 4.22 for the Switching architecture and in Figure 4.23 for the Modulation architecture. QPSK and 16-QAM signals are generated for different symbol rates by Keysight M8190A Arbitrary Waveform Generator (AWG) at a carrier frequency $f_{dat} = 0.750$ GHz. The sampling rate of the AWG is 12 GSa/s. Internally of AWG the I-Q signal is filtered by a root raised cosine (RRC) filter with a roll-off coefficient $\alpha = 0.35$. The number of symbols used for every EVM calculation is 1000. The electrical signal from the AWG, amplified by the driver module, modulates an optical carrier, via an MZM, which is injected at the SOA-MZI. The quadrature point is selected as the operating point of the MZM with $V_{bias} = 2.9$ V.

In the same way as in the *CG* experimental setups, the sampled output signal at ports I and J is filtered by the OBPF, photodetected and amplified by AMP 1.

Due to the Digital Sampling Oscilloscope (DSO) limited bandwidth (about 1.5 GHz), the up-converted RF signals at 9.25 GHz and 39.25 GHz at the SOA-MZI output are down-converted to IF signals at 550 MHz by an electrical mixer. The electrical power of the local oscillator signal at f_{RF2} is 13 dBm. The electrical mixer is characterized by a 10 dB conversion loss. Before the DSO, the up-converted signal is filtered by a 1 GHz electrical filter and amplified by a 40 dB electrical amplifier (AMP 2). After the signal digitization by the real-time DSO, a Vector Signal Analyzer (VSA) software demodulates the complex-modulated data and it also assess the quality of the up-converted signals by calculating the EVM. During the EVM measurements, adaptive equalization was applied in VSA which removes linear errors from modulated signals by dynamically creating

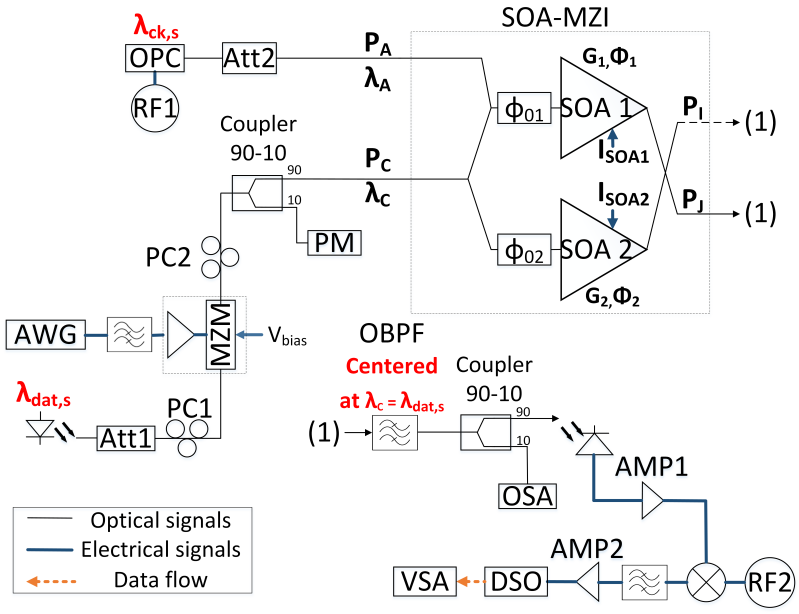

Figure 4.22: Complex modulation measurement setup for Switching architecture. AWG: Arbitrary Waveform Generator. DSO: Digital Sampling Oscilloscope. VSA: Vector Signal Analyzer. (1) denotes the direction of transmission from SOA-MZI output ports I and J alternatively to the VSA. Reproduced from [1] (© 2020 IEEE).

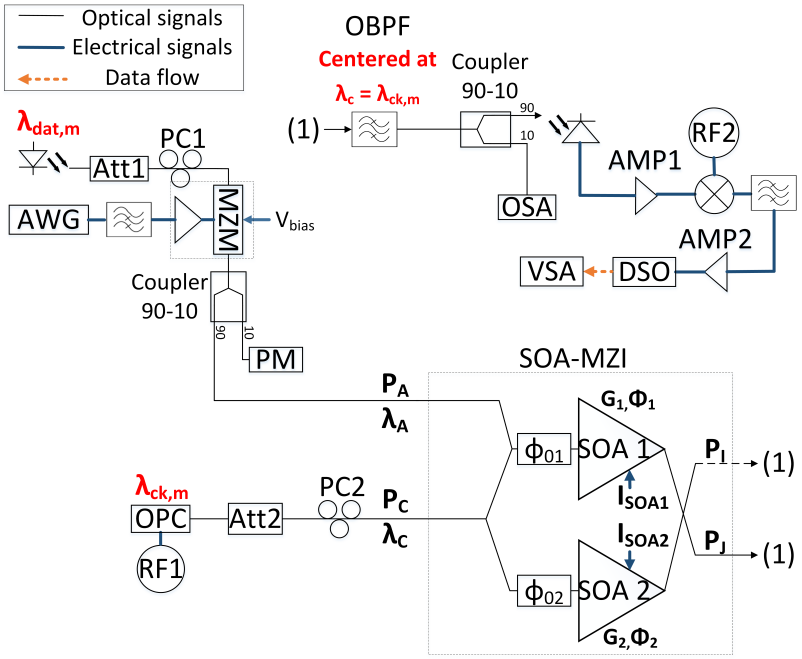

Figure 4.23: Complex modulation measurement setup for Modulation architecture. (1) denotes the direction of transmission from SOA-MZI output ports I and J alternatively to the DSO. Reproduced from [1] (© 2020 IEEE).

and applying a Finite Impulse Response (FIR) (feed-forward) compensating filter. The options used in this equalization filter are 21 for filter length and 10^{-7} for convergence limit. Before every measurement, adaptive is set to run, in order for the VSA to use the results to calculate the filter coefficients and after some seconds when EVM is quasi-constant, adaptive is set to hold, and the measurement is taken.

The EVM measure is related to the BER with Equation 4.30, and the acceptable limit is defined as the value that provides an equivalent BER of $3.8 \cdot 10^{-3}$, which guarantees error-free performance after applying Forward Error Correction (FEC) techniques [12]. This limit is different for QPSK and 16-QAM modulation formats as indicated by a dashed line in Figures 4.24 and 4.25. These figures show that the up-converted signals at 9.25 GHz and 39.25 GHz using the Modulation architecture have very similar quality in terms of EVM, in contrast to significant differences observed when using the Switching architecture. This is explained by the small-signal equation analysis presented in 4.1 and stems from the different principle of operation of the two architectures. Using the Modulation architecture, we can perform up-conversion even at high harmonics without significant degradation of the up-converted signal quality.

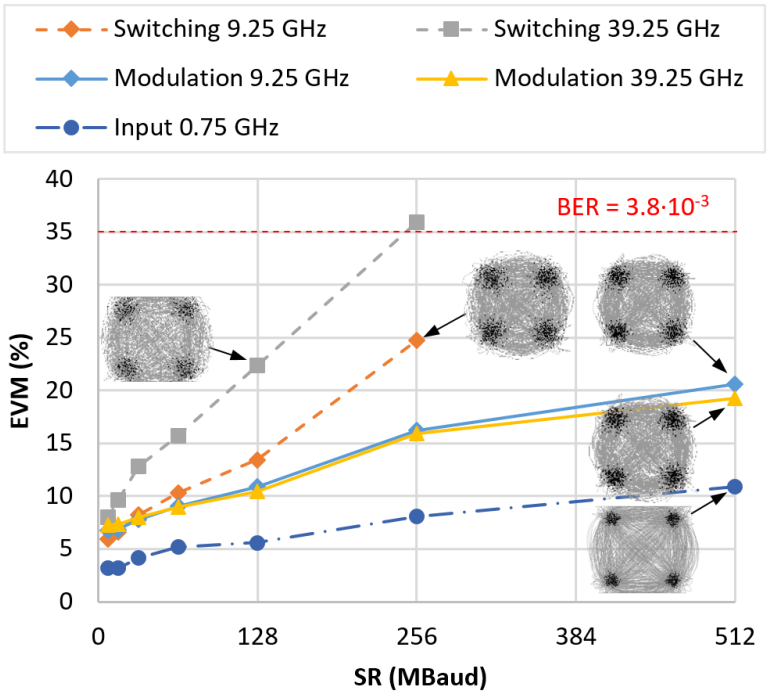

Figure 4.24: EVM vs. SR comparison between Switching and Modulation architectures for frequency up-conversion of QPSK-modulated data at 9.25 GHz and 39.25 GHz. The EVM of the input signal at 0.75 GHz to be up-converted is plotted as a reference. The insets depict constellation diagrams at specific points. EVM acceptable limit is indicated by the horizontal dashed line. Reproduced from [1] (© 2020 IEEE).

In Figure 4.24, for QPSK-modulated data, an $SR = 512$ MBaud is achieved for frequency conversions from 0.75 GHz to 9.25 GHz and from 0.75 GHz to 39.25 GHz under the FEC limit of $3.8 \cdot 10^{-3}$ when employing the Modulation architecture. On the other hand, the Switching architecture performance deteriorates rapidly as the SR increases, reaching the limit of EVM $\approx$ 35% for the conversion towards 39.25 GHz and approximating EVM = 25% for the conversion towards 9.25 GHz at an $SR = 256$ MBaud. Measurements at a $SR = 512$ MBaud for the Switching architecture for the conversion to 39.25 GHz and even to 9.25 GHz have resulted in significantly distorted constellation diagrams and EVM values higher than 37%, and therefore they have not been included in Figure 4.24. Comparing the inset constellation diagrams in Figure 4.24 it can be deduced that the QPSK signal for the Switching architecture between 9.25 GHz and 39.25 GHz is significantly deteriorated even for a lower SR values, whereas comparing the inset constellation diagrams for the Modulation architecture it can be inferred that the QPSK signal for the Modulation architecture between 9.25 GHz and 39.25 GHz remains almost unchanged and clear. Furthermore, it is observed that the higher CG for the Switching architecture than for the Modulation architecture for the frequency conversion to 9 GHz in 4.2 does not translate to a better EVM for Switching architecture. This is due to the high distortion of the sampled signal that stems from the limited carrier lifetime in SOA1 as explained in detail in 3.1.1.1.

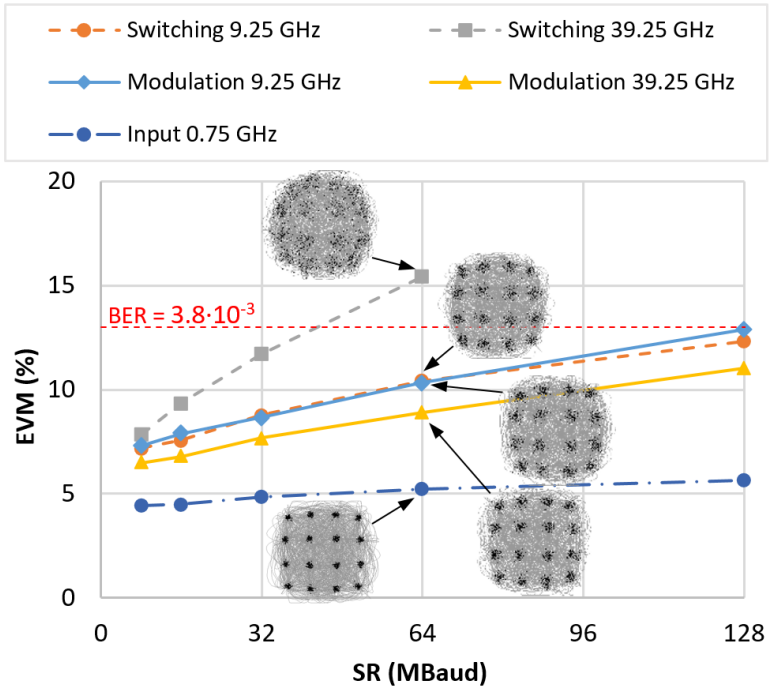

Figure 4.25: EVM vs. SR comparison between Switching and Modulation architectures for frequency up-conversion of 16-QAM modulated data at 9.25 GHz and 39.25 GHz. The EVM of the input signal at 0.75 GHz to be up-converted is plotted as a reference. The insets depict constellation diagrams at specific points. EVM acceptable limit is indicated by the horizontal dashed line. Reproduced from [1] (© 2020 IEEE).

In Figure 4.25, an $SR = 128$ Mbaud is achieved for 16-QAM modulated data with the Modulation architecture for frequency conversions from 0.75 GHz to 9.25 GHz and from 0.75 GHz to 39.25 GHz under the FEC limit of $3.8 \cdot 10^{-3}$. The same holds for the Switching architecture for frequency conversions from 0.75 GHz to 9.25 GHz. Conversely, for frequency conversions from 0.75 GHz to 39.25 GHz only an SR up to 32 Mbaud is acceptable. It is worth noting that if the 16-QAM constellation diagrams in Figure 4.25 are more closely observed, it is realized that their shape is not perfectly squared and that the demodulated symbols corresponding to the four diagonal outer points are misplaced towards the center, thus giving the impression that the constellation diagrams are compressed to the center of the constellation. This is a clear sign of amplitude distortion. On the contrary, no clear sign of phase distortion is observed.

16-QAM modulation is more demanding as the Euclidean distance between symbols in the constellation diagram is smaller [12]. Thus, the highest acceptable SR for QPSK is 512 MBaud (bit rate equal to 1 Gb/s), while it is 128 MBaud (bit rate equal to 512 Mb/s) for 16-QAM.

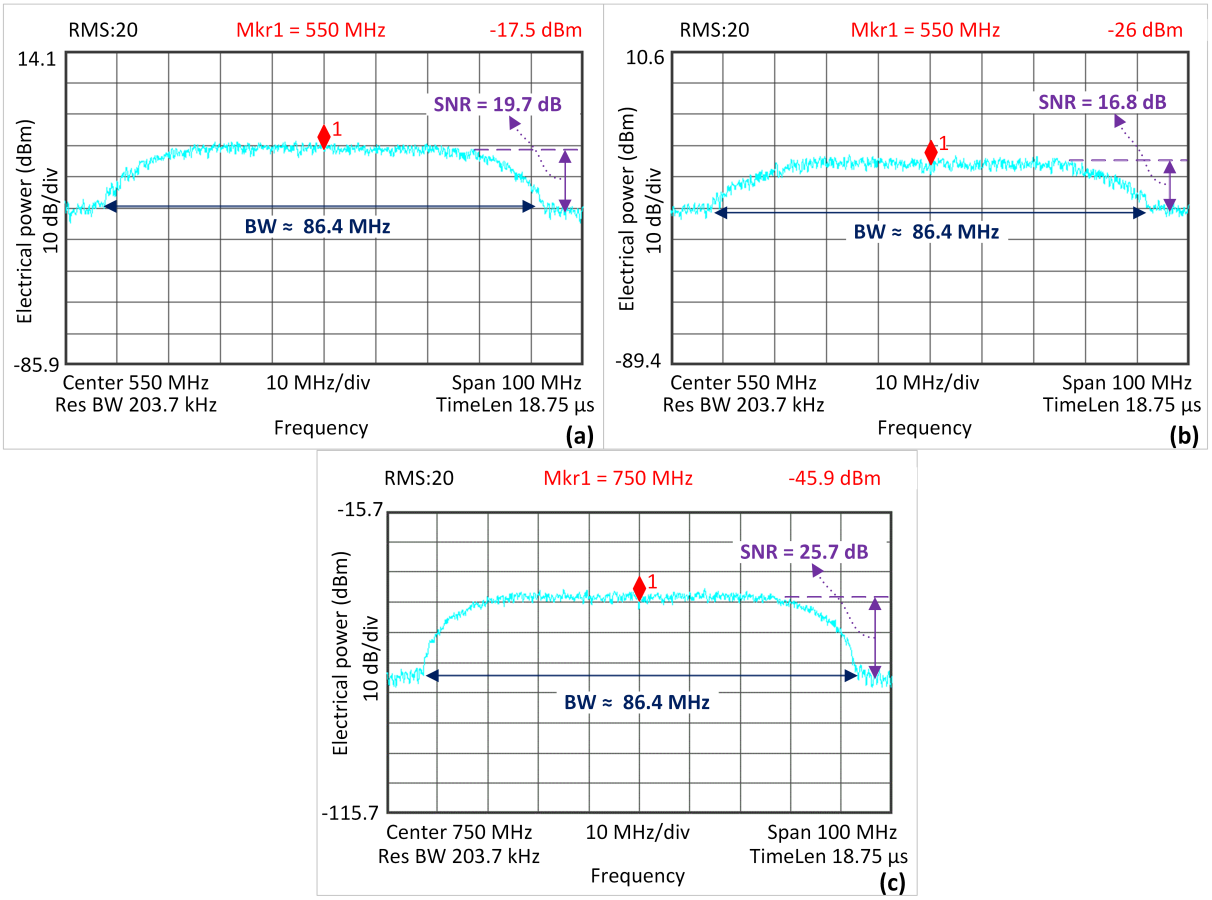

Figure 4.26: QPSK electrical spectra corresponding to the frequency conversions at 9.25 GHz (a) and at 39.25 GHz (b) for Switching architecture , as well as the electrical spectrum of the signal to be up-converted (c) with $SR = 64$ Mbaud. Reproduced from [1] (© 2020 IEEE).

Finally, the QPSK electrical spectra which correspond to the frequency conversions at 9.25 GHz and at 39.25 GHz for the Switching architecture, as well as the electrical spectrum of the input signal to be up-converted with $SR = 64$ Mbaud is shown in Figure 4.26(a), (b) and (c), respectively. All three spectra are measured by the VSA. According to Equation (4.27), for $SR = 64$ Mbaud and for roll-off factor $\alpha = 0.35$, $BW = 86.4$ MHz, which is approximately the value observed in the electrical spectra. Furthermore, the SNR measured by the VSA is depicted in every spectrum. As expected, that the SNR values provided by the VSA are approximately the same with the ones observed in the electrical spectra. It is also worth noting that by replacing the SNR values in Equation (4.29), the corresponding EVM values of Figure 4.24 are retrieved, meaning that for the spectra of Figure 4.26 white noise is the main source of measurement error.

4.4 Conclusion

A theoretical and experimental analysis of the performance differences between Switching and Modulation architectures of a SOA-MZI photonic mixer used for frequency up-conversion purposes have been presented. In the theoretical part, a closed-form expression has been derived for the CG, which provides qualitative insight into this metric of the two architectures as higher harmonics of the sampling signal participate in the frequency conversion. In the experimental part, a CG equal to 16 dB is achieved for the 1 GHz to 9 GHz conversion when employing the Switching architecture, while a CG equal to 9 dB is achieved for the 1 GHz to 39 GHz conversion when employing the Modulation architecture. The matching between the experimental and theoretical results for the CG is very good. The conversion of complex-modulated data signals has also been realized by the photonic microwave mixer. A sufficiently low EVM for QPSK and 16-QAM modulations is obtained when employing the Modulation architecture for both 0.75 GHz to 9.25 GHz and 0.75 GHz to 39.25 GHz frequency conversion. This allows to support a data bit rate equal to 1 Gbps and 512 Mbps for QPSK and 16-QAM, respectively.

References

[1] D. Kastritsis, T. Rampone, K. E. Zoiros, and A. Sharaiha, "Modulation and Switching Architecture Performances for Frequency Up-Conversion of Complex-Modulated Data Signals Based on a SOA-MZI Photonic Sampling Mixer," *Journal of Lightwave Technology*, vol. 38, no. 19, pp. 5375–5385, Oct. 2020.

[2] D. A. O. Davies, "Small-signal analysis of wavelength conversion in semiconductor laser amplifiers via gain saturation," *IEEE Photonics Technology Letters*, vol. 7, no. 6, pp. 617–619, Jun. 1995.

[3] C. Bohémond, "Mélangeur de signaux hyperfréquences basé sur la modulation croisée du gain d'un amplificateur optique à semi-conducteurs," Ph.D. dissertation, École Nationale d'Ingénieurs de Brest, Brest, France, Jan. 2010.

[4] A. Sharaiha, "Harmonic and intermodulation distortion analysis by perturbation and harmonic balance methods for in-line photodetection in a semiconductor optical amplifier," *IEEE Photonics Technology Letters*, vol. 10, no. 3, pp. 421–423, Mar. 1998.

[5] M. Spyropoulou, N. Pleros, and A. Miliou, "Soa-mzi based nonlinear optical signal processing: A frequency domain transfer function for wavelength conversion, clock recovery, and packet envelope detection," *IEEE Journal of Quantum Electronics*, vol. 47, no. 1, pp. 40–49, Jan. 2011.

[6] C. Bohémond, T. Rampone, and A. Sharaiha, "Performances of a photonic microwave mixer based on cross-gain modulation in a semiconductor optical amplifier," *Journal of Lightwave Technology*, vol. 29, no. 16, pp. 2402–2409, Aug. 2011.

[7] H. Termos, "Study of up & down conversion technique by all-optical sampling based on SOA-MZI All-optical radiofrequency sampling mixer based on a Semiconductor Optical Amplifier Mach-Zehnder Interferometer using a standard and a differential configuration," Ph.D. dissertation, École Nationale d'Ingénieurs de Brest, Brest, France, Feb. 2017.

[8] D. Kastritsis, T. Rampone, K. Zoiros, and A. Sharaiha, "Comparison of two photonic sampling mixer architectures based on SOA-MZI for all-optical frequency up-conversion," in *Proc. 2018 IEEE International Topical Meeting on Microwave Photonics (MWP)*, Oct. 2018, pp. 1–4.

[9] H.-G. Yeh and V. R. Ramirez, "Implementation and performance of a m-ary psk and qam-ofdm system in a tms320vc5416 digital signal processor," in *2007 Second International Conference on Digital Telecommunications (ICDT'07)*, 2007, pp. 19–19.

[10] *Vector Signal Analysis Basics*, Keysight Technologies, USA, 2014.

[11] R. Schmogrow, B. Nebendahl, M. Winter, A. Josten, D. Hillerkuss, S. Koenig, J. Meyer, M. Dreschmann, M. Huebner, C. Koos, J. Becker, W. Freude, and J. Leuthold, "Error Vector Magnitude as a Performance Measure for Advanced Modulation Formats," *IEEE Photonics Technology Letters*, vol. 24, no. 1, pp. 61–63, Jan. 2012.

[12] M. Seimetz, *Performance Trends*. Berlin, Heidelberg: Springer Berlin Heidelberg, 2009, vol. 143, pp. 227–237.

Conclusions and perspectives

In summary, a photonic sampler was theoretically and experimentally studied. The module employed as sampler was based on a Mach-Zehnder interferometric structure bearing in both arms semiconductor optical amplifiers (SOA-MZI). This module was combined with a mode-locked laser (MLL), which was used to provide the sampling pulse sequence of short and very short pulses with Full Width at Half Maximum (FWHM) of 12.6 ps or 1.6 ps. The operation of SOA-MZI is purely photonic. This implementation with SOAs has the advantages of providing gain at the output and a high Extinction Ratio (ER). Additionally, the proposed module enjoys the benefit of low temporal jitter, high flexibility and adaptability while it has a direct compatibility as an all-optical one with the optical fibers without the need of slow opto-electronic conversions.

A key point during the thesis work was the conception and study of Modulation architecture for the SOA-MZI photonic sampler, in addition to the well known Switching architecture, by interchanging the input ports in which the sampling signal and the signal to be sampled are injected in the SOA-MZI. This seemingly insignificant change alters significantly the behavior of SOA-MZI sampler and each architecture presents different advantages and disadvantages. The major advantage of the Modulation architecture is that the frequency content of the sampling MLL signal is not limited by the Cross-Phase Modulation (XPM) as is the case for Switching architecture, potentially enabling the use of very high sampling rates up to 100 GHz or more.

In chapter 2, general information were provided and key parameters were specified regarding optical sampling and the SOA device. In addition, the principle of operation of more advanced systems were explained in detail, where the photonic sampler can be used as a building block, such as in an Analog to Digital Converter (ADC) or in a Radio over Fiber (RoF) system as a photonic sampler mixer. Furthermore, a detailed derivation of the SOA-MZI equations were presented. Moreover, a theoretical performance analysis of the static and dynamic characteristics of the SOA-MZI in general, as well as the experimental static and dynamic characteristics of the SOA-MZI used in this thesis were illustrated. Theoretically, analytical expressions of the ER were obtained at both SOA-MZI output ports. Experimentally, ER was evaluated and found equal to 19.3 dB and 9.73 dB at SOA-MZI ports J and I, respectively. Moreover, the XPM bandwidth of the SOA-MZI module were evaluated for different wavelength and power combinations and found for all cases examined between 5-5.9 GHz.

In chapter 3, the sampling process with the use of the SOA-MZI photonic sampler is investigated. In this context, the principle of operation of the two architectures of Switching and Modulation were demonstrated and their advantage and disadvantages were specified. Moreover,

the response of the SOA-MZI photonic sampler in the quasi-static i.e., sampling Continuous Wave (CW) signals for a range of powers from -40 dBm to +3.7 dBm and dynamic regime i.e., sampling sinusoidal signals with Modulation Indices (MI) equal to 20%, 40%, 60% and 80%, was investigated employing the Modulation architecture. The significant deterioration of the sampled signal's linearity in terms of THD made pertinent the need of a linearization method. Thus, a post-distortion linearization technique was developed theoretically and applied experimentally in order to improve its overall performance. The linearization model is based on the static regime equations of SOA, and thus it has the advantage of lower complexity compared to a model based on dynamic equation of SOA. This approach, however, is limited by the fact that the effectiveness of the method decreases as the frequency of the signal to be sampled increases. The potential improvement in terms of Total Harmonic Distortion (THD) using the linearization technique was estimated at 19.6 dB for sinusoidal signals with MI between 20% and 80%. Experimentally, this improvement was verified for a sinusoidal signal to be sampled at 250 MHz with $MI = 80\%$. Also, a significant improvement in terms of THD was observed experimentally for sinusoidal signals to be sampled, at 250 MHz and at 500 MHz with MI equal to 40%, 60% and 80%, and at 1 GHz and at 2 GHz with MI equal to 60%.

In chapter 4, the SOA-MZI photonic sampler used as a frequency mixer was theoretically examined by developing a small-signal analysis model, and experimentally evaluated and validated using Switching and Modulation architectures in terms of Conversion Gain (CG). In the theoretical part, an expression in closed-form was derived for the CG, which provides qualitative insight into this metric of the two architectures as higher harmonics of the sampling signal participate in the frequency conversion. In the experimental part, frequency up-conversion of a sinusoidal signal from 1 GHz to 9 GHz and to 39 GHz were evaluated in terms of CG. A CG equal to 16 dB was achieved for the 1 GHz to 9 GHz conversion when employing the Switching architecture, while a CG equal to 9 dB was achieved for the 1 GHz to 39 GHz conversion when employing the Modulation architecture. Furthermore, complex-modulated data with Quadrature Phase Shift Keying (QPSK) and Quadrature Amplitude Modulation with 16 states (16-QAM) of different Symbol Rates (SR) were up-converted from 0.75 GHz to 9.25 GHz and to 39.25 GHz and the quality of the up-conversion provided by the SOA-MZI photonic sampler was evaluated in terms of Error Vector Magnitude (EVM). A sufficiently low EVM for QPSK and 16-QAM modulations was obtained when employing the Modulation architecture for both 0.75 GHz to 9.25 GHz and 0.75 GHz to 39.25 GHz frequency conversion. The maximum bit rate that meets the limit for error-free communication via Forward Error Correction (FEC) was achieved using the Modulation architecture and is 1 Gbps and 512 Mbps for the QPSK and 16-QAM architecture, respectively.

Although interesting results have been demonstrated in this work, we suggest some points to be addressed that would be a possible extension of this Ph.D work listed in the following.

Regarding the SOA-MZI sampler in general:

- Utilization of the SOA-MZI photonic sampler as a constituent part in a complete photonic ADC design with time-division, with regular time-to-wavelength mapping and with modified time-to-wavelength mapping employing time-stretching (TS), similar to the ones presented in chapter 1. Integration of the SOA-MZI sampler in such a system would permit to exploit the full potential of an optically sampled and electronically quantized ADC.
- Utilization of the SOA-MZI photonic sampler as a frequency mixer component in a complete RoF design, similar to the one presented in chapter 1.
- Study of the influence of real data in the application of linearization method.
- Application of different methods of linearization and comparison with the post-distortion method developed during this thesis work.

Also, regarding the application of frequency mixer:

- Up-conversion to over 100 GHz using the Modulation architecture.
- Thorough study of the influence of SOA Gain, differential carrier lifetime and saturation power variation in CG using the small-signal analysis model.

List of Publications

Scientific Journals

Publications Related to PhD Thesis

[1] **D. Kastritsis**, T. Rampone, K. E. Zoiros, and A. Sharaiha, "Modulation and Switching Architecture Performances for Frequency Up-Conversion of Complex-Modulated Data Signals Based on a SOA-MZI Photonic Sampling Mixer," *Journal of Lightwave Technology*, vol. 38, no. 19, pp. 5375–5385, Oct. 2020.

[2] **D. Kastritsis**, T. Rampone, M. Franco, K. E. Zoiros, and A. Sharaiha, "SOA-MZI photonic sampler with a post-distortion linearization technique," *Optics Express*, vol. 29, no. 15, pp.23 736–23 751, Jul. 2021.

Other Publications

[3] K. E. Zoiros, **D. Kastritsis**, T. Rampone, and A. Sharaiha, "Reflective semiconductor optical amplifier pattern effect compensation with birefringent fiber loop," *Optical and Quantum Electronics*, vol. 52, no. 8, p. 366, Aug. 2020.

Conferences

International Conferences

[4] **D. Kastritsis**, T. Rampone, K. E. Zoiros, and A. Sharaiha, "Comparison of two photonic sampling mixer architectures based on SOA-MZI for all-optical frequency up-conversion," in *Proc. 2018 IEEE International Topical Meeting on Microwave Photonics (MWP)*. Toulouse, France, Oct. 2018. (Presented in the form of poster).

[5] **D. Kastritsis**, K. E. Zoiros, T. Rampone, and A. Sharaiha, "SOA-MZI All-Optical RoF Signal Mixing," in *Proc. IEEE International Conference on Transparent Optical Networks (ICTON)*. Angers, France, Jul. 2019. (Presented in the form of oral presentation).

[6] N. Hamdash, **D. Kastritsis**, T. Rampone, A. Sharaiha, K. E. Zoiros, D. L. Berre, N. Martin, and C. Quendo, "Optical functions for microwave signal processing using SOA and SOA-MZI," presented at the *XXI Simpósio de Aplicações Operacionais em Áreas de Defesa (XXI SIGE)*, São José dos Campos, São Paulo, Brazil, Sep. 2019. (Presented by Prof. Ammar Sharaiha).

French National Conferences

[7] **D. Kastritsis**, T. Rampone, K. E. Zoiros, and A. Sharaiha, "Échantillonnage par modulation tout-optique d'un train d'impulsions courtes dans un SOA-MZI appliqué à la transposition de fréquence," presented at the *Journée du Club Optique-Microondes (JCOM 2018)*, Toulouse, France, Jul. 2018. (Presented in the form of poster).

[8] **D. Kastritsis**, T. Rampone, K. E. Zoiros, and A. Sharaiha, "Technique de linéarisation pour un SOA-MZI dans un contexte d'échantillonnage tout-optique," presented at the *Journée du Club Optique-Microondes (JCOM 2019)*, Brest, France, Jun. 2019. (Presented in the form of oral presentation and of poster).

ΕΚΤΕΝΗΣ ΠΕΡΙΛΗΨΗ ΣΤΑ ΕΛΛΗΝΙΚΑ

Τίτλος διατριβής στα Ελληνικά:

Οπτική δειγματοληψία βασισμένη σε συμβολόμετρο Mach-Zehnder με οπτικούς ενισχυτές ημιαγωγού (SOA-MZI) για αναλογικές εφαρμογές.

1 Κίνητρα και Σκοπός Έρευνας

Τις τελευταίες δεκαετίες, η ερευνητική περιοχή της φωτονικής μικροκυμάτων (Microwave Photonics - MWP) έχει προσελκύσει μεγάλο ενδιαφέρον και έχει εξελιχθεί σε σημαντικό βαθμό. Η MWP ορίζεται ως το διεπιστημονικό πεδίο που συνδυάζει από τις ηλεκτροπτικές και αμιγώς οπτικές συσκευές, μονάδες και συστήματα με την τεχνολογία μικροκυμάτων. Λόγω της διπλής φύσης της, επιτρέπει την εκτέλεση ορισμένων λειτουργιών είτε στο ηλεκτρικό είτε στο οπτικό επίπεδο. Η επιλογή μεταξύ των δύο επιπέδων εξαρτάται από την αξιολόγηση των πλεονεκτημάτων και των περιορισμών της συγκεκριμένης ηλεκτρονικής ή οπτικής μονάδας που είναι διαθέσιμη για το σκοπό αυτό. Το κίνητρο για τη χρήση οπτικών μονάδων σε συστήματα μικροκυμάτων που αντικαθιστούν τις αντίστοιχες ηλεκτρονικές είναι ότι οι οπτικές μονάδες μπορούν να επωφεληθούν άμεσα από το μεγάλο εύρος ζώνης, τις χαμηλές απώλειες και την υψηλή ανοσία στις ηλεκτρομαγνητικές παρεμβολές (Electromagnetic Interference - EMI) των οπτικών ινών. Τα τελευταία χρόνια, έχει γίνει μια εντατική προσπάθεια για την έρευνα νέων τεχνικών φωτονικής μικροκυμάτων για διαφορετικές εφαρμογές. Σε γενικές γραμμές, τα θέματα που καλύπτονται από την φωτονική μικροκυμάτων περιλαμβάνουν φωτονική παραγωγή μικροκυματικών και χιλιοστομετρικών σημάτων (mm-wave), μετατροπή συχνοτήτων σε υψηλότερες (ανόρθωση συχνότητας) ή σε χαμηλότερες συχνότητες (υποβιβασμός συχνότητας), οπτικά ελεγχόμενες κεραίες συστοιχίας φάσεων (optically controlled phased array antennas), μετάδοση ραδιοκυμάτων πάνω από οπτικές ίνες (Radio over Fiber - RoF) και φωτονικούς μετατροπείς από αναλογικό σε ψηφιακό (Photonic Analog to Digital Converter - PADC) [1–3]. Η MWP μπορεί να χρησιμοποιηθεί για εφαρμογές σε ευρυζωνικά δίκτυα ασύρματης πρόσβασης, σε δίκτυα αισθητήρων, στις δορυφορικές επικοινωνιών, σε παλμογράφους πολύ υψηλού εύρους ζώνης, σε συστήματα 5G, σε ραντάρ, στο διαδίκτυο των πραγμάτων (Internet of Things - IoT) καθώς και σε συστήματα ηλεκτρονικού πολέμου [4–8].

Ένα βασικό μπλοκ διάγραμμα ενός συστήματος φωτονικής μικροκυμάτων απεικονίζεται στο Σχήμα 1. Ένα σήμα εισόδου στο πεδίο των ραδιοσυχνοτήτων (Radio Frequencies - RF), το οποίο ρυθμίζεται σωστά από ένα ηλεκτρικό κύκλωμα οδήγησης, μετατρέπεται στον οπτικό επίπεδο από έναν ηλεκτρο-οπτικό διαμορφωτή (Electro-optic Modulator - EOM). Στην συνέχεια το σήμα μεταδίδεται μέσω μιας οπτικής ίνας και ακολούθως υποβάλλεται σε επεξεργασία από φωτονικές συσκευές. Το επεξεργασμένο σήμα μεταδίδεται και πάλι μέσω μιας οπτικής ίνας και μετατρέπεται ξανά στον ηλεκτρικό επίπεδο από έναν φωτο-δέκτη. Το τελικό RF σήμα εξόδου λαμβάνεται μετά απο κατάλληλη επεξεργασία στο ηλεκτρικό επίπεδο. Το σήμα εισόδου ή το σήμα εξόδου ή και τα δύο θα μπορούσαν να ληφθούν ή να μεταδοθούν από μια κεραία, όπως συμβαίνει συνήθως στα συστήματα RoF.

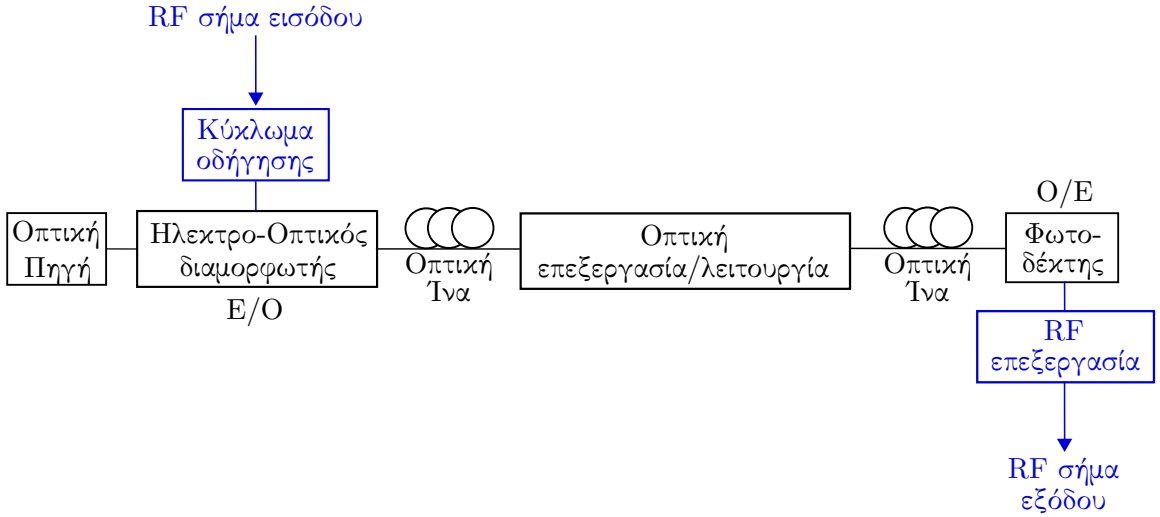

Σχήμα 1: Βασικό μπλοκ διάγραμμα ενός συστήματος φωτονικής μικροκυμάτων. Η ηλεκτρική καλωδίωση και το περίγραμμα των ηλεκτρικών συσκευών είναι με μπλε χρώμα, ενώ οι συνδέσεις οπτικών ινών και το περίγραμμα των φωτονικών συσκευών και μονάδων είναι σε μαύρο χρώμα. Επίσης, τα περιγράμματα του Ηλεκτροπτικού διαμορφωτή (EOM) που μετατρέπει το σήμα από το ηλεκτρικό σε οπτικό στρώμα (E/O) και του φωτοδέκτη που εκτελεί το αντίστροφο (O/E) είναι σε μαύρο χρώμα.

Σε αυτό το πλαίσιο, και προκειμένου να επεκταθεί η δυνατότητα και η ευελιξία ενός συστήματος MWP, η ανάπτυξη ενός υποσυστήματος στο οπτικό επίπεδο για την εκτέλεση της διαδικασίας της δειγματοληψίας είναι ζωτικής σημασίας.

2 Οπτική δειγματοληψία

Η οπτική δειγματοληψία αναφέρεται σε μια κατηγορία τεχνικών όπου τα οπτικά σήματα, συνήθως με τη μορφή πολύ σύντομων παλμών, χρησιμοποιούνται για τη δειγματοληψία ηλεκτρικών ή οπτικών σημάτων. Αρχικά, η διαδικασία δειγματοληψίας επιτελούνταν στο ηλεκτρικό επίπεδο, γεγονός

που εμπόδιζε την αύξηση της αποδοτικότητας της εξαιτίας του περιορισμένου εύρους ζώνης των ηλεκτρικών κυματοδηγών και της αυξημένης διακύμανσης χρονισμού (jitter) των ηλεκτρονικών ταλαντωτών [1, 2]. Ωστόσο, τελευταία, η δειγματοληψία στο οπτικό επίπεδο έχει καταστεί μια ελκυστική τεχνολογική εναλλακτική λόγω της ικανότητάς της να συνδυάζει τα πλεονεκτήματα των οπτικών ινών (χαμηλή εξασθένηση, μεγάλο εύρος ζώνης κλπ.) με τη δυνατότητα χρήσης ενός χαμηλής διακύμανσης χρονισμού λέιζερ εγκλείδωσης τρόπων (Mode-Locked Laser - MLL [9, 10] για την παραγωγή του σήματος δειγματοληψίας [11–13].

Η λειτουργία της δειγματοληψίας είναι θεμελιώδης και χρησιμοποιείται σε μεγάλο αριθμό εφαρμογών. Μερικές τυπικές εφαρμογές της οπτικής δειγματοληψίας είναι:

1. Μετατροπείς από αναλογικό σε ψηφιακό με ρυθμούς δειγματοληψίας δεκάδες Gigahertz. Εφαρμογές σε ραντάρ ευρείας ζώνης, σε επικοινωνίες οπτικών ινών και σε παλμογράφους.

2. Χαρακτηρισμός παλμοσειρών με πολύ μικρό εύρος παλμών της τάξης των ps με εξαιρετικά υψηλούς ρυθμούς επανάληψης, όπως συμβαίνει π.χ. σε συστήματα επικοινωνίας οπτικών ινών με χρονική πολυπλεξία.

3. Δημιουργία μικροκυματικών ή χιλιοστομετρικών σημάτων.

Πολλές λειτουργίες έχουν αναπτυχθεί τα τελευταία χρόνια για εφαρμογές φωτονικής μικροκυμάτων χρησιμοποιώντας οπτικούς ενισχυτές ημιαγωγού (Semiconductor Optical Amplifiers - SOA) είτε μεμονωμένα είτε ενσωματωμένους στη συμβολομετρική δομή Mach-Zehnder (Semiconductor Optical Amplifier – Mach-Zehnder Interferometer - SOA-MZI). Αυτές οι πολυλειτουργικές συσκευές παρουσιάζουν τεράστιο φασματικό εύρος λειτουργίας και υψηλή μη γραμμική συμπεριφορά. Επιπλέον, έχουν το πλεονέκτημα του μικρού μεγέθους και μπορούν να ενσωματωθούν είτε μονολιθικά είτε υβριδικά με άλλα ηλεκτρικά εξαρτήματα και διατάξεις ραδιοσυχνοτήτων [14, 15].

Το θέμα της διατριβής εστιάζει στην διάταξη του SOA-MZI, ενός αμιγώς φωτονικού δομοστοιχείου, που χρησιμοποιείται για τους σκοπούς της φωτονικής δειγματοληψίας (Σχήμα 2). Αυτή η διατριβή αποσκοπεί να καλύψει το κενό της χρήσης της μονάδας SOA-MZI ως φωτονικού δειγματολήπτη στη θέση άλλων ηλεκτροπτικών δειγματοληπτών όπως π.χ. ο ηλεκτροπτικός διαμορφωτής Mach-Zehnder (Mach-Zehnder Modulator - MZM) που είναι η πιο συχνή επιλογή. Με αυτόν τον τρόπο, κερδίζουμε το πρόσθετο πλεονέκτημα του να καταστήσουμε το φωτονικό δειγματολήπτη μια πλήρως οπτική μονάδα, δύνοντας την δυνατότητα να αποφύγουμε τις επιπλέον ηλεκτροπτικές μετατροπές υψηλού κόστους.

Το οπτικό σήμα δειγματοληψίας (sampling signal) που χρησιμοποιείται παράγεται από ένα ενεργό laser εγκλείδωσης τρόπων active MLL). Δύο αρχιτεκτονικές είναι δυνατές με το φωτονικό δειγματολήπτη SOA-MZI, οι αρχιτεκτονικές Switching και Modulation. Η πρώτη αρχιτεκτονική είναι καλά εδραιωμένη για τον SOA-MZI, ενώ η δεύτερη είναι νέα και χρησιμοποιείται για πρώτη φορά κατά την διάρκεια αυτής της διατριβής. Επίσης, σε αντίθεση με τις περισσότερες σχετικές έρευνες,

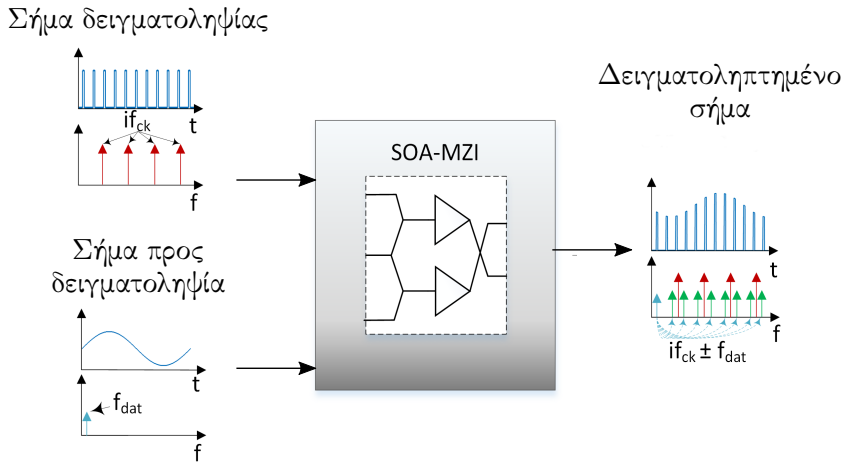

Σχήμα 2: Σχηματικό διάγραμμα φωτονικού δειγματολήπτη SOA-MZI.

αναλύονται εκτενώς τα πειραματικά αποτελέσματα της δειγματοληψίας στο πεδίο του χρόνου. Επιπλέον, μια μέθοδος γραμμικοποίησης της απόκρισης του φωτονικού δειγματολήπτη SOA-MZI με μετεπεξεργασία (post-processing) διατυπώνεται θεωρητικά και εφαρμόζεται πειραματικά για πρώτη φορά.

Ο φωτονικός δειγματολήπτης SOA-MZI μπορεί τελικά να ενσωματωθεί ως μονάδα σε πιο σύνθετα συστήματα. Ο φωτονικός δειγματολήπτης SOA-MZI μπορεί να χρησιμοποιηθεί για την εκτέλεση της διαδικασίας δειγματοληψίας σε ένα PADC είτε με πολυπλεξία διαίρεσης χρόνου είτε με πολυπλεξία με αντιστοίχιση χρόνου σε μήκος κύματος (time-to-wavelength mapping) παρόμοια με αυτή στην αναφορά [11]. Επιπλέον, ο φωτονικός δειγματολήπτης SOA-MZI μπορεί να χρησιμοποιηθεί ως μίκτης συχνοτήτων είτε για ανόρθωση είτε για υποβιβασμό συχνότητας υποστηρίζοντας προσθέτως την δυνατότητα μετατροπής από μια συχνότητα σε πολλαπλές συχνότητες σε μια πλήρη εφαρμογή RoF παρόμοια με αυτήν του Σχήματος 3. Στις προαναφερθείσες εφαρμογές, το προτεινόμενο σύστημα απολαμβάνει το πλεονέκτημα του χαμηλού jitter, ενώ μετατρέπει τα αντίστοιχα ηλεκτροπτικά συστήματα σε πλήρως οπτικά.

Οι κυριότεροι στόχοι της προτεινόμενη έρευνας ήταν:

1. Αξιολόγηση απόδοσης της διαδικασίας δειγματοληψίας του φωτονικού δειγματολήπτη SOA-MZI, ακολουθούμενη από τεχνική γραμμικοποίησης post-processing προκειμένου να βελτιστοποιηθεί η λειτουργία του.

2. Αξιολόγηση απόδοσης διαφορετικών αρχιτεκτονικών με βάση τον φωτονικό δειγματολήπτη SOA-MZI για την εφαρμογή του μίκτη για ανόρθωση συχνότητας σε θεωρητικό και πειραματικό επίπεδο.

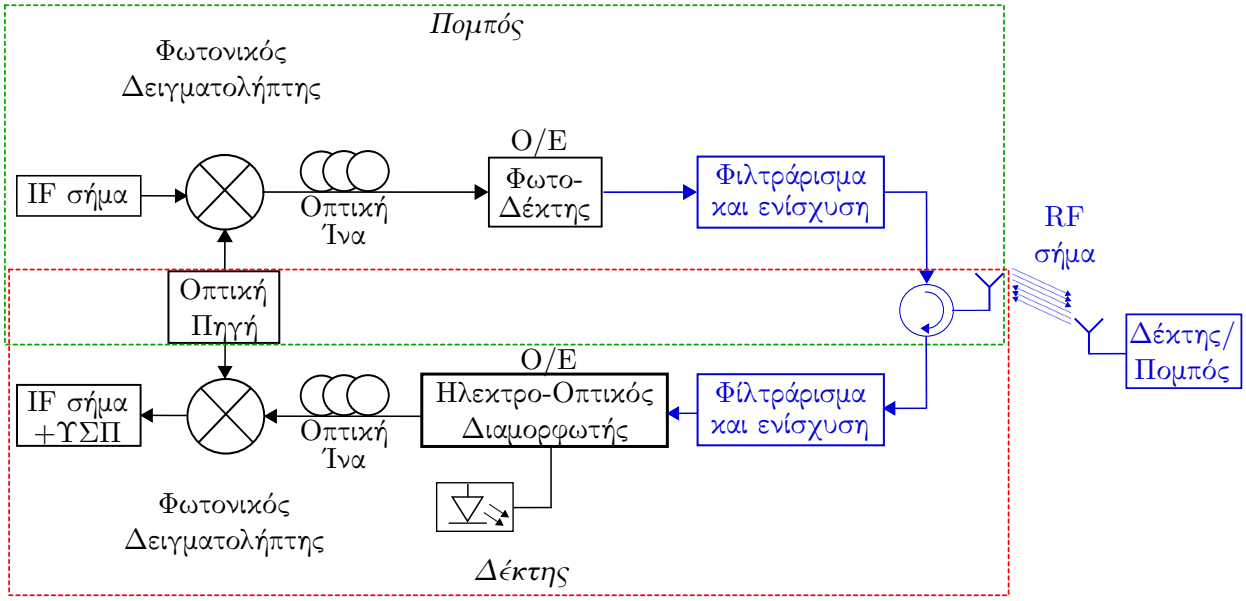

Σχήμα 3: Ενσωμάτωση του φωτονικού δειγματολήπτη ως μίκτη σε σύστημα ραδιοκυμάτων πάνω από οπτική ίνα (RoF). Οι ηλεκτρικές καλωδιώσεις και το περίγραμμα των ηλεκτρικών συσκευών είναι χρωματισμένες με μπλε χρώμα, ενώ οι συνδέσεις ινών και το περίγραμμα των φωτονικών συσκευών και μονάδων είναι χρωματισμένες με μαύρο χρώμα. Επίσης, το περίγραμμα του φωτοδέκτη που εκτελεί τη μετατροπή από τον οπτικό στον ηλεκτρικό τομέα (O/E) είναι χρωματισμένες με μαύρο χρώμα. ΥΣΠ: Υψηλότερο της IF Συχνοτικό Περιεχόμενο.

3 Πειραματικός χαρακτηρισμός του δειγματολήπτη SOA-MZI

Αρχικά διερευνάται η διαδικασία δειγματοληψίας με τη χρήση του φωτονικού δειγματολήπτη SOA-MZI. Στο πλαίσιο αυτό, καταδείκνύεται η αρχή λειτουργίας των δύο αρχιτεκτονικών Switching και Modulation και προσδιορίζονται τα πλεονεκτήματα και τα μειονεκτήματά τους [16]. Ένα βασικό σημείο κατά τη διάρκεια της διατριβής είναι η σύλληψη της ιδέας για υλοποίηση μιας αρχιτεκτονικής Modulation για τον φωτονικό δειγματολήπτη SOA-MZI επιπλέον της γνωστής αρχιτεκτονικής Switching με την εναλλαγή των θυρών εισόδου στις οποίες το σήμα δειγματοληψίας και το προς δειγματοληψία σήμα εισάγονται στον SOA-MZI. Αυτή η φαινομενικά ασήμαντη αλλαγή αλλάζει σημαντικά τη συμπεριφορά του δειγματολήπτη SOA-MZI και η κάθε αρχιτεκτονική παρουσιάζει διαφορετικά πλεονεκτήματα και μειονεκτήματα. Η αρχιτεκτονική Switching έχει το μειονέκτημα της υποβάθμισης της διαδικασίας δειγματοληψίας, καθώς ο ρυθμός δειγματοληψίας και άρα η συχνότητα επανάληψης του MLL αυξάνεται λόγω της πεπερασμένης διάρκειας ζωής των φορέων του SOA που αντανακλάται στο εύρος ζώνης XPM και περιορίζεται σε λίγα GHz. Από την άλλη μεριά, η αρχιτεκτονική Modulation επιτρέπει την χρήση πολύ υψηλών ρυθμών δειγματοληψίας της τάξης των 100 GHz ή και περισσότερο εφόσον η συχνότητα επανάληψης του MLL και γενικότερα το

συχνοτικό του περιεχόμενο δεν φιλτράρεται από το φαινόμενο της διασταυρούμενης διαμόρφωσης φάσης (Cross-Phase Modulation - XPM).

Στην συνέχεια, διευρευνάται η απόκριση του φωτονικού δειγματολήπτη SOA-MZI σε οιωνεί στατικό καθεστώς (quasi-static regime), δηλ. δειγματοληψία συνεχούς σήματος (Continuous Wave - CW) για ένα εύρος ισχύων από -40 dBm έως +3,7 dBm και δυναμικό καθεστώς, δηλ. δειγματοληψία ημιτονοειδών σημάτων με δείκτες διαμόρφωσης (Modulation Index - MI) ίσους με 20%, 40%, 60% και 80%, χρησιμοποιώντας την αρχιτεκτονική Modulation. Το εύρος ημίσειας ισχύος (FWHM) των παλμών του σήματος δειγματοληψίας που χρησιμοποιείται κατά την διάρκεια του πειράματος μετράται στα 12,6 ps και η συχνότητα επανάληψης του MLL ρυθμίζεται στα 10 GHz. Η σημαντική επιδείνωση της γραμμικότητας του δειγματοληπτούμενου σήματος ποσοτικοποιούμενη ως προς το μετρικό της ολικής αρμονικής παραμόρφωσης (Total Harmonic Distortion - THD) καθιστά αναγκαία την χρήση μιας μεθόδου γραμμικοποίησης. Έτσι μια τεχνική γραμμικοποίησης post-processing αναπτύσσεται θεωρητικά και εφαρμόζεται πειραματικά προκειμένου να βελτιώσει την συνολική της απόδοση. Το μοντέλο γραμμικοποίησης βασίζεται στις εξισώσεις στατικού καθεστώτος (static regime) του SOA και επομένως έχει το πλεονέκτημα της χαμηλότερης πολυπλοκότητας σε σύγκριση με άλλα μοντέλα που βασίζονται σε εξισώσεις δυναμικού καθεστώτος (dynamic regime) του SOA. Παρόλα αυτά, εξαιτίας αυτής της προσέγγισης, η αποτελεσματικότητα της μεθόδου μειώνεται καθώς αυξάνεται η συχνότητα του προς δειγματοληψία σήματος. Η μέγιστη προσδοκώμενη βελτίωση βελτίωση του μετρικού THD με χρήση της τεχνικής γραμμικοποίησης υπολογίζεται στα 19,6 dB για ημιτονοειδή σήματα με MI μεταξύ 20% και 80%. Πειραματικά, αυτή η βελτίωση επαληθεύεται για δειγματοληψία ημιτονοειδούς σήματος στα 250 MHz με $MI = 80\%$. Επίσης, σημαντική βελτίωση ως προς το THD παρατηρείται πειραματικά για ημιτονοειδή σήματα προς δειγματοληψία, στα 250 MHz και στα 500 MHz με MI ίσο με 40%, 60% και 80%, και στο 1 GHz με MI ίσο με 60%. Εκτενές κομμάτι αυτής της ερευνητικής εργασίας δημοσιεύτηκε στο περιοδικό Optics Express [17].

4 Θεωρητικός και πειραματικός χαρακτηρισμός του δειγματολήπτη SOA-MZI ως μίκτη

Ο φωτονικός δειγματολήπτης SOA-MZI επιτελώντας της διαδικασία της μίξης συχνότητας εξετάζεται θεωρητικά αναπτύσσοντας ένα μοντέλο ανάλυσης μικρού σήματος το οποίο και αξιολογείται πειραματικά και επικυρώνεται χρησιμοποιώντας τις αρχιτεκτονικές Switching και Modulation ως προς το μετρικό του κέρδους μετατροπής (CG). Στο θεωρητικό μέρος, προκύπτει μια έκφραση σε κλειστή μορφή για το CG, η οποία παρέχει ποιοτική εικόνα στο CG των δύο αρχιτεκτονικών καθώς υψηλότερες αρμονικές του σήματος δειγματοληψίας συμμετέχουν στη μετατροπή συχνότητας. Χρησιμοποιώντας αυτήν την έκφραση κλειστής μορφής μπορούμε να προβλέψουμε την απόδοση σε CG για ένα γνωστό σύνολο παραμέτρων του SOA και οπτικών ισχύων στις εισόδους του SOA-MZI, κα-

θώς και αντίστροφα μπορούμε να επιλέξουμε τις κρίσιμες παραμέτρους του σχήματος προκειμένου να βελτιστοποιήσουμε την απόδοση του μετατροπέα συχνότητας. Στο πειραματικό μέρος, το εύρος ημίσειας ισχύος (FWHM) των παλμών του σήματος δειγματοληψίας είναι 1,6 ps και η συχνότητα επανάληψης του MLL ήταν 10 GHz. Η ανόρθωση συχνότητας ενός ημιτονοειδούς σήματος από 1 GHz σε 9 GHz και σε 39 GHz αξιολογείται ως προς το CG. CG ίσο με 16 dB επιτυγχάνεται για τη μετατροπή από 1 GHz σε 9 GHz κατά τη χρήση της αρχιτεκτονικής Switching, ενώ CG ίσο με 9 dB επιτυγχάνεται για τη μετατροπή από 1 GHz σε 39 GHz κατά τη χρήση της αρχιτεκτονικής Modulation. Επιπλέον, διαμορφωμένο φέρον με διαμόρφωση μετατόπισης φάσης με τετραγωνισμό (Quadrature Phase Shift Keying - QPSK) και συνδυασμένη διαμόρφωση πλάτους-φάσης 16 καταστάσεων (16-Quadrature Amplitude Modulation - 16-QAM) διαφορετικών ρυθμών συμβόλων (Symbol Rate - SR) μετατρέπεται από 0,75 GHz σε 9,25 GHz και σε 39,25 GHz. Η ποιότητα της μετατροπής προς τα πάνω που παρέχεται από το φωτονικό δειγματολήπτη SOA-MZI αξιολογείται με βάση το μέγεθος του διανύσματος σφάλματος (Error Vector Magnitude - EVM). Όταν χρησιμοποιείται η αρχιτεκτονική Modulation ένα αρκετά χαμηλό EVM επιτυγχάνεται για τις διαμορφώσεις QPSK και 16-QAM κατά την μετατροπή της συχνότητας του φορέα του από 0,75 GHz σε 9,25 GHz και από 0,75 GHz σε 39,25 GHz. Ο μέγιστος ρυθμός δεδομένων που επιτυγχάνεται με EVM, που να εμπίπτει στο όριο για επικοινωνία χωρίς σφάλματα μετά την εφαρμογή τεχνικών Forward Error Correction (FEC), είναι ίσος με 1 Gbps και 512 Mbps για QPSK και 16-QAM διαμορφωμένα σήματα, αντίστοιχα. Εκτενή κομμάτια αυτής της ερευνητικής εργασίας δημοσιεύτηκαν σε δύο διεθνή συνέδρια με πρακτικά και στο επιστημονικό περιοδικό Journal of Lightwave Technology [16, 18, 19].

5 Βασικοί άξονες και επιτεύγματα της διατριβής

Συνοπτικά, οι βασικοί άξονες της διατριβής και τα επιτεύγματα σε κάθε άξονα είναι:

1. Γενικές πληροφορίες παρουσιάζονται και βασικές παράμετροι καθορίζονται σχετικά με την οπτική δειγματοληψία και τη συσκευή SOA. Επιπλέον, επεξηγείται λεπτομερώς η αρχή της λειτουργίας πιο σύνθετων συστημάτων, όπου ο φωτονικός δειγματολήπτης μπορεί να χρησιμοποιηθεί ως δομικό στοιχείο, όπως σε έναν μετατροπέα αναλογικού σε ψηφιακό (ADC) ή σε ένα σύστημα RoF ως φωτονικός μίκτης δειγματοληψίας. Ακόμη, παρουσιάζεται μια λεπτομερής εξαγωγή των εξισώσεων του SOA-MZI. Επιπλέον, παρουσιάζεται μια θεωρητική ανάλυση την απόδοσης των στατικών και δυναμικών χαρακτηριστικών του SOA-MZI, όπως και των πειραματικών στατικών και δυναμικών χαρακτηριστικών του SOA-MZI που χρησιμοποιείται σε αυτή τη διατριβή. Θεωρητικά, αναλυτικες εκφράσεις εξάγονται για το μετρικό Extinction ratio - ER στις δύο θύρες εξόδου του SOA-MZI. Πειραματικά, το ER βρέθηκε ίσο με 19,3 dB και 9,73 dB στις θύρες J και I, αντίστοιχα, για τον SOA-MZI που χρησιμοποιείται σε αυτή τη διατριβή. Επιπλέον, το εύρος ζώνης XPM του δομοστοιχείου SOA-MZI αξιολογε-

ίται για διαφορετικούς συνδυασμούς μήκους κύματος και ισχύος και βρίσκεται για όλες τις περιπτώσεις που εξετάστηκαν μεταξύ 5-5,9 GHz. Τα σχετικά αποτελέσματα παρουσιαζονται αναλυτικά στο κεφάλαιο 2 της διατριβής.

2. Η ποιότητα της παρεχόμενης δειγματοληψίας από τον φωτονική μονάδα SOA-MZI αξιολογείται πειραματικά με βάση αποτελέσματα στο πεδίο του χρόνου και της συχνότητας κάνοντας χρήση της νέας και αρκετά υποσχόμενης αρχιτεκτονικής Modulation. Τα σχετικά αποτελέσματα παρουσιαζονται αναλυτικά στο κεφάλαιο 3 της διατριβής.

3. Τεχνική γραμμικοποίησης με μετεπεξεργασία αναπτύσσεται και τίθεται σε εφαρμογή πειραματικά βελτιώνοντας σημαντικά την απόδοση του δειγματολήπτη ως προς την THD για εύρος συχνοτήτων δειγματοληπτούμενου σήματος από 250 MHz – 2 GHz. Τα σχετικά αποτελέσματα παρουσιαζονται αναλυτικά στο κεφάλαιο 3 της διατριβής.

4. Η απόδοση της αρχιτεκτονικής Switching και Modulation με βάση τον φωτονικό δειγματολήπτη SOA-MZI αξιολογείται ως προς το CG για την εφαρμογή του μίκτη και για ανόρθωση συχνότητας ημιτονοειδούς σήματος από 1 GHz σε 9 GHz και από 1 GHz σε 39 GHz. Τα σχετικά αποτελέσματα παρουσιαζονται αναλυτικά στο κεφάλαιο 4 της διατριβής.

5. Θεωρητικό μοντέλο μικρού σήματος (small signal) αναπτύσσεται και επικυρώνεται με βάση πειραματικά αποτελέσματα το οποίο μπορεί να προβλέπει την απόδοση σε CG με βάση κρίσιμες παραμέτρους των SOA που είναι ενσωματωμένοι στον SOA-MZI καθώς και των ισχύων εισόδου του SOA-MZI. Αντίστροφα, οι παράμετροι του SOA μπορούν να επιλεχθούν κατάλληλα για να βελτιστοποιηθεί η απόδοση του δειγματολήπτη ως μίκτη. Τα σχετικά αποτελέσματα παρουσιαζονται αναλυτικά στο κεφάλαιο 4 της διατριβής.

6. Η απόδοση της αρχιτεκτονικής Switching και Modulation με βάση τον φωτονικό δειγματολήπτη SOA-MZI αξιολογείται ως προς το EVM για την εφαρμογή του μίκτη και για ανόρθωση συχνότητας φέροντος διαμορφωμένου με QPSK και 16-QAM από 0,75 GHz σε 9,25 GHz και από 0,75 GHz σε 39,25 GHz. Ο μέγιστος ρυθμός δεδομένων για επικοινωνία χωρίς σφάλματα μέσω χρήσης FEC, επιτυγχάνεται χρησιμοποιώντας την αρχιτεκτονική Modulation και είναι ίσος με 1 Gbps και 512 Mbps για QPSK και 16-QAM διαμορφωμένα σήματα, αντίστοιχα. Τα σχετικά αποτελέσματα παρουσιαζονται αναλυτικά στο κεφάλαιο 4 της διατριβής.

6 Προοπτικές της διατριβής

Αν και έχουν επιδειχθεί ενδιαφέροντα αποτελέσματα σε αυτή την διατριβή, προτείνουμε ορισμένα σημεία που πρέπει να εξεταστούν, τα οποία και θα αποτελούσαν μια πιθανή επέκταση αυτής και παρατίθενται παρακάτω. Σχετικά με τον δειγματολήπτη SOA-MZI γενικά:

- Χρήση του φωτονικού δειγματολήπτη SOA-MZI ως συστατικό στοιχείο σε ένα πλήρες PADC είτε με πολυπλεξία διαίρεσης χρόνου, είτε με τιμε-το-ωαελενγτη μαππινγ συνδιασμένη με διάταση χρόνου (Time Stretching - TS). Η ενσωμάτωση του δειγματολήπτη SOA-MZI σε ένα τέτοιο σύστημα θα επέτρεπε την πλήρη αξιοποίηση των δυνατοτήτων ενός PADC με φωτονική δειγματοληψία και ηλεκτρονικό κβαντισμό.
- Μελέτη της επίδρασης πραγματικών δεδομένων στην εφαρμογή της μεθόδου γραμμικοποίησης.
- Εφαρμογή διαφορετικών μεθόδων γραμμικοποίησης και σύγκρισης τους με τη μέθοδο post-processing που αναπτύχθηκε κατά τη διάρκεια αυτής της διατριβής.

Επίσης, σχετικά με την εφαρμογή του δειγματολήπτη SOA-MZI ως μείκτη συχνοτήτων:

- Χρήση του φωτονικού δειγματολήπτη SOA-MZI σε μια πλήρη σχεδίαση RoF.
- Μετατροπή συχνότητας προς τα πάνω σε συχνότητες μεγαλύτερες των 100 GHz χρησιμοποιώντας την αρχιτεκτονική Modulation.
- Διεξοδική μελέτη της επιρροής του κέρδους του SOA, της δυναμικής διάρκειας ζωής των φορέων (dynamic carrier lifetime) και της επιρροής της διακύμανσης ισχύος κορεσμού στο CG χρησιμοποιώντας το μοντέλο ανάλυσης μικρού σήματος.

References

[1] J. Capmany and D. Novak, "Microwave photonics combines two worlds," *Nature Photonics*, vol. 1, no. 6, pp. 319–330, Jun. 2007.

[2] J. Capmany, J. Mora, I. Gasulla, J. Sancho, J. Lloret, and S. Sales, "Microwave Photonic Signal Processing," *Journal of Lightwave Technology*, vol. 31, no. 4, pp. 571–586, Feb. 2013, publisher: IEEE. [Online]. Available: https://www.osapublishing.org/jlt/abstract.cfm?uri=jlt-31-4-571

[3] Z. Tang, Y. Li, J. Yao, and S. Pan, "Photonics-Based Microwave Frequency Mixing: Methodology and Applications," *Laser & Photonics Reviews*, vol. 14, no. 1, p. 1800350, 2020. [Online]. Available: https://onlinelibrary.wiley.com/doi/abs/10.1002/lpor.201800350

[4] P. Ghelfi, F. Laghezza, F. Scotti, G. Serafino, S. Pinna, D. Onori, E. Lazzeri, and A. Bogoni, "Photonics in Radar Systems: RF Integration for State-of-the-Art Functionality," *IEEE Microwave Magazine*, vol. 16, no. 8, pp. 74–83, Sep. 2015.

[5] P. Ghelfi, F. Scotti, D. Onori, and A. Bogoni, "Photonics for Ultrawideband RF Spectral Analysis in Electronic Warfare Applications," *IEEE Journal of Selected Topics in Quantum Electronics*, vol. 25, no. 4, pp. 1–9, Jul. 2019.

[6] C. Vagionas, E. Ruggeri, A. Tsakyridis, G. Kalfas, Y. Leiba, A. Miliou, and N. Pleros, "Linearity Measurements on a 5G mmWave Fiber Wireless IFoF Fronthaul Link With Analog RF Beamforming and 120° Degrees Steering," *IEEE Communications Letters*, vol. 24, no. 12, pp. 2839–2843, Dec. 2020.

[7] S. Weber, E. H. Waller, C. Kaiser, and G. v. Freymann, "Time-stretched real-time measurement technique for ultrafast absorption variations with TS/s sampling-rate," *Optics Express*, vol. 25, no. 13, pp. 14 125–14 133, Jun. 2017, publisher: Optical Society of America. [Online]. Available: https://www.osapublishing.org/oe/abstract.cfm?uri=oe-25-13-14125

[8] D. Novak, R. B. Waterhouse, A. Nirmalathas, C. Lim, P. A. Gamage, T. R. Clark, M. L. Dennis, and J. A. Nanzer, "Radio-Over-Fiber Technologies for Emerging Wireless Systems," *IEEE Journal of Quantum Electronics*, vol. 52, no. 1, pp. 1–11, Jan. 2016.

[9] A. Ly, V. Auroux, R. Khayatzadeh, N. Gutierrez, A. Fernandez, and O. Llopis, "Highly Spectrally Pure 90-GHz Signal Synthesis Using a Coupled Optoelectronic Oscillator," *IEEE Photonics Technology Letters*, vol. 30, no. 14, pp. 1313–1316, Jul. 2018.

[10] V. Billault, V. Crozatier, G. Baili, L. Morvan, D. Dolfi, N. Kanagaraj, and H. G. d. Chatellus, "Phase Noise of Optical Pulse Trains Generated by Talbot Effect in Frequency Shifting Loops," *Journal of Lightwave Technology*, vol. 39, no. 8, pp. 2336–2347, Apr. 2021.

[11] A. Khilo, S. J. Spector, M. E. Grein, A. H. Nejadmalayeri, C. W. Holzwarth, M. Y. Sander, M. S. Dahlem, M. Y. Peng, M. W. Geis, N. A. DiLello, J. U. Yoon, A. Motamedi, J. S. Orcutt, J. P. Wang, C. M. Sorace-Agaskar, M. A. Popović, J. Sun, G.-R. Zhou, H. Byun, J. Chen, J. L. Hoyt, H. I. Smith, R. J. Ram, M. Perrott, T. M. Lyszczarz, E. P. Ippen, and F. X. Kärtner, "Photonic ADC: overcoming the bottleneck of electronic jitter," *Optics Express*, vol. 20, no. 4, pp. 4454–4469, Feb. 2012. [Online]. Available: https://www.osapublishing.org/oe/abstract.cfm?uri=oe-20-4-4454

[12] B. C. Pile and G. W. Taylor, "Performance of Subsampled Analog Optical Links," *Journal of Lightwave Technology*, vol. 30, no. 9, pp. 1299–1305, May 2012, conference Name: Journal of Lightwave Technology.

[13] P. W. Juodawlkis, J. C. Twichell, G. E. Betts, J. J. Hargreaves, R. D. Younger, J. L. Wasserman, F. J. O'Donnell, K. G. Ray, and R. C. Williamson, "Optically sampled analog-to-digital converters," *IEEE Transactions on Microwave Theory and Techniques*, vol. 49, no. 10, pp. 1840–1853, Oct. 2001.

[14] M. J. Connelly, *Semiconductor Optical Amplifiers*. Boston: Kluwer Academic Publishers, 2004. [Online]. Available: http://link.springer.com/10.1007/b101817

[15] S. Nakamura, Y. Ueno, K. Tajima, J. Sasaki, T. Sugimoto, T. Kato, T. Shimoda, M. Itoh, H. Hatakeyama, T. Tamanuki, and T. Sasaki, "Demultiplexing of 168-Gb/s data pulses with a hybrid-integrated symmetric Mach-Zehnder all-optical switch," *IEEE Photonics Technology Letters*, vol. 12, no. 4, pp. 425–427, Apr. 2000, conference Name: IEEE Photonics Technology Letters.

[16] D. Kastritsis, T. Rampone, K. Zoiros, and A. Sharaiha, "Comparison of two photonic sampling mixer architectures based on SOA-MZI for all-optical frequency up-conversion," in *2018 International Topical Meeting on Microwave Photonics (MWP)*, Oct. 2018, pp. 1–4.

[17] D. Kastritsis, D. Kastritsis, T. Rampone, M. Franco, K. E. Zoiros, and A. Sharaiha, "SOA-MZI photonic sampler with a post-distortion linearization technique," *Optics Express*, vol. 29, no. 15, pp. 23 736–23 751, Jul. 2021. [Online]. Available: https://www.osapublishing.org/oe/abstract.cfm?uri=oe-29-15-23736

[18] D. Kastritsis, K. E. Zoiros, T. Rampone, and A. Sharaiha, "SOA-MZI All-Optical RoF Signal Mixing," in *2019 21st International Conference on Transparent Optical Networks (ICTON)*, Jul. 2019, pp. 1–4, iSSN: 2161-2064.

[19] D. Kastritsis, T. Rampone, K. E. Zoiros, and A. Sharaiha, "Modulation and Switching Architecture Performances for Frequency Up-Conversion of Complex-Modulated Data Signals Based on a SOA-MZI Photonic Sampling Mixer," *Journal of Lightwave Technology*, vol. 38, no. 19, pp. 5375–5385, Oct. 2020.

APPENDICES

Appendix A

Pritel UOC-E-05-20 active mode locked laser

A.1 Principle of operation

Pritel UOC-E-05-20 mode-locked fiber ring laser system is shown in Figure A.1. The gain of the fiber laser is provided by an PM-EDFA. The cavity length is such that produces a ring mode spacing of about 8 MHz. The ring modes produced are grouped into a series of supermodes. For a mode-locked laser to be stable only a single supermode should be amplified in the cavity while all the other supermodes are attenuated. For this purpose inside this mode-locked laser, a lithium niobate Mach-Zehnder modulator and a Tunable Filter are employed. The Mach Zehnder modulator allows only the pulses that are synchronized with the Ext. Clock to be amplified as shown in Figure A.1, so that the pulse repetition frequency is equal to Ext.Clock frequency. Moreover, the tunable filter makes sure that the only supermode that rests or lases is the one whose frequencies match the peaks of the angle-tuned etalon while the cavity length remains constant. Nevertheless, small temperature fluctuations of the device can cause slight cavity length changes which by their turn make reappear a second supermode. In order to keep the cavity length constant the mode locked laser is situated inside a temperature controlled chamber and additionally a phased-locked loop is employed, not shown in Figure A.1, which adjusts appropriately a microproccessor-control micrometer as well as the Piezoelectric transducer (PZT).

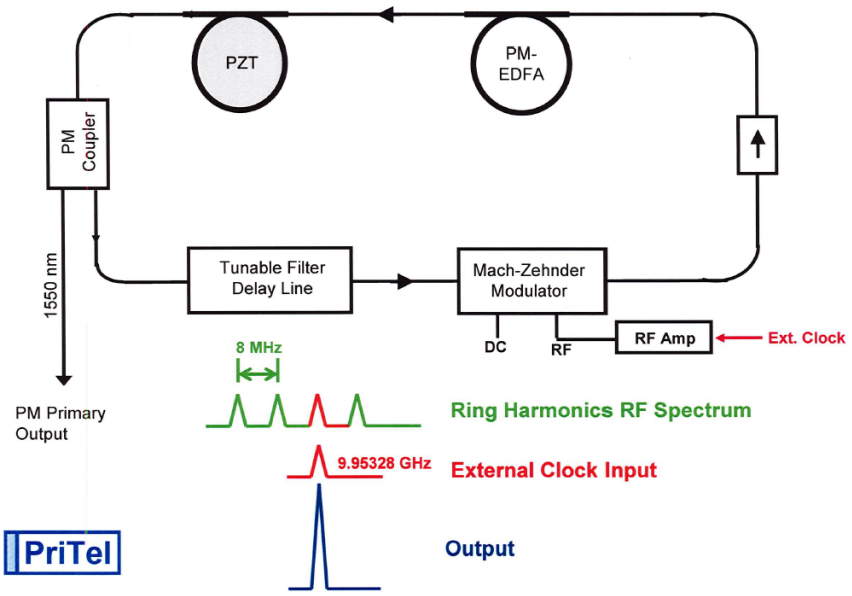

Figure A.1: Ultra-fast optical pulse source schematic diagram. PM-EDFA: Polarization Maintaining-Erbium Doped Fiber Amplifier. PZT: Piezoelectric Transducer [1]

Appendix B

SOA-MZI PHOTONIC SAMPLER MIXER

B.1 Carrier Density Variation

The partial derivative of the gain of SOAk with respect to the carrier density is given by the following equation:

$$\frac{\partial G_k}{\partial N_k} = \Gamma \alpha L \overline{G}_k \tag{B.1}$$

The partial derivative of phase shift, induced by SOAk, with respect to the carrier density is given by:

$$\frac{\partial \Phi_k}{\partial N_k} = -\frac{\alpha_H}{2} \Gamma \alpha L \tag{B.2}$$

Taking into account (2.31) and assuming identical α_H and α_{int} values for both SOAs, the differential phase shift between the two arms of the SOA-MZI equals:

$$\overline{\Phi}_{1,\alpha} - \overline{\Phi}_{2,\alpha} = -\frac{\alpha_H}{2} \ln \left(\frac{\overline{G}_{1,\alpha}}{\overline{G}_{2,\alpha}} \right) \tag{B.3}$$

Assuming for simplicity that the differential carrier lifetime τ_d is approximately the same for SOA1 between Switching and Modulation architectures, the first-order variation imposed on the carrier density is given by [2]:

$$n_{1,\omega_{cki},\alpha} = -\frac{p_{cki,\alpha} \frac{\partial R_{1,cki,\alpha}}{\partial P_{1,cki,\alpha}}}{\eta_\alpha (1 + j\omega_{cki}\tau_d)} \tag{B.4}$$

$$n^*_{1,\omega_{dat},\alpha} = -\frac{p^*_{dat,\alpha} \frac{\partial R_{1,dat,\alpha}}{\partial P_{1,dat,\alpha}}}{\kappa_\alpha (1 - j\omega_{dat}\tau_d)} \tag{B.5}$$

where η_α and κ_α are the attenuation coefficients of $p_{cki,\alpha}$ and $p^*_{dat,a}$ because of the intermediate couplers between the SOA-MZI input ports and SOA1 input according to Figure 4.1.

The second-order density variation of the carrier density is given by [2]:

$$n_{1,\omega_{cki-dat},\alpha} = -\left(n_{1,\omega_{cki},\alpha} \frac{p^*_{dat,\alpha}}{\kappa_\alpha} \frac{\partial^2 R_{1,dat,\alpha}}{\partial N_1 \partial P_{1,dat,\alpha}} + n^*_{1,\omega_{dat},\alpha} \frac{p_{cki,\alpha}}{\eta_\alpha} \frac{\partial^2 R_{1,cki,\alpha}}{\partial N_1 \partial P_{1,cki,\alpha}} \right) \cdot \cdot \frac{\tau_d}{2[1 + j(\omega_{cki} - \omega_{dat})\tau_d]} \quad \text{(B.6)}$$

$R_{1,cki,\alpha}$ and $R_{1,dat,\alpha}$ are the recombination rates due to the amplification of the optical carriers at angular frequencies ω_{cki} and ω_{dat}, respectively, and are given by the following equations [2]:

$$R_{1,cki,\alpha} = \frac{P_{1,cki,\alpha}\lambda_{cki,\alpha}}{hc} \frac{\Gamma g_{m1,\alpha}}{g_{n1,\alpha}} \frac{\overline{G}_{1,\alpha} - 1}{wdL} \quad \text{(B.7)}$$

$$R_{1,dat,\alpha} = \frac{P_{1,dat,\alpha}\lambda_{dat,\alpha}}{hc} \frac{\Gamma g_{m1,\alpha}}{g_{n1,\alpha}} \frac{\overline{G}_{1,\alpha} - 1}{wdL} \quad \text{(B.8)}$$

where h is Plank's constant, c is the speed of light in vacuum, $g_{m1,\alpha}$ and $g_{n1,\alpha}$ are the SOA 1 material gain and net gain at architecture α and, w and d are the SOAs width and height of the active area, respectively.

Using the approximations $\Gamma g_{m1,\alpha} \approx g_{n1,\alpha}$, $G_{1,\alpha} - 1 \approx G_{1,\alpha}$ and $\lambda \approx \lambda_{ck,s} \approx \lambda_{dat,s}$ as in [2], we obtain:

$$\frac{\partial R_{1,cki,\alpha}}{\partial P_{1,cki,\alpha}} = \frac{\partial R_{1,dat,\alpha}}{\partial P_{1,dat,\alpha}} = \frac{\lambda}{hc \cdot wdL} \overline{G}_{1,\alpha} \quad \text{(B.9)}$$

Applying (B.9) to (B.7) and (B.8), we obtain:

$$n_{1,\omega_{cki},\alpha} = -\frac{p_{cki,\alpha} \frac{\lambda}{hc \cdot wdL} \overline{G}_{1,\alpha}\tau_d}{\eta_\alpha(1 + j\omega_{cki}\tau_d)} \quad \text{(B.10)}$$

$$n^*_{1,\omega_{dat},\alpha} = -\frac{p^*_{dat,\alpha} \frac{\lambda}{hc \cdot wdL} \overline{G}_{1,\alpha}\tau_d}{\kappa_\alpha(1 - j\omega_{dat}\tau_d)} \quad \text{(B.11)}$$

B.2 K_α

K_α is a constant defined by:

$$K_\alpha = \frac{\lambda}{hc \cdot wdL} \frac{C_{OP_\alpha}}{32} \quad \text{(B.12)}$$

Applying Equations (4.16) of C_{OP_α}, (B.1) of $\frac{\partial \Phi_k}{\partial N_k}$, (B.3) of $\overline{\Phi}_{1,\alpha} - \overline{\Phi}_{2,\alpha}$ and (3.13) of P_{sat} to Equation (4.21) we obtain:

$$K_\alpha = \frac{\overline{G}_{1,\alpha}}{32P_{sat}\tau_{ASE}} \left[1 - \sqrt{\frac{\overline{G}_{2,\alpha}}{\overline{G}_{1,\alpha}}} \left[\cos\left(-\frac{\alpha_H}{2} \ln \frac{\overline{G}_{1,\alpha}}{\overline{G}_{2,\alpha}} \right) + \alpha_H \sin\left(-\frac{\alpha_H}{2} \ln \frac{\overline{G}_{1,\alpha}}{\overline{G}_{2,\alpha}} \right) \right] \right] \quad \text{(B.13)}$$

B.3 SOA-MZI model parameters

The differential carrier lifetime τ_d can be approximated by the SOA-MZI bandwidth using a pump-probe technique as in 2.4.4.2. Taking the cut-off frequency f_{cut} equal to 6 GHz, then the τ_d equals $1/2\pi f_{cut}$ [3, 4].

The optical power, $p_{cki,\alpha}$, required for the small-signal analysis calculations is derived from RF spectra for the Switching and Modulation architectures. These spectra were taken after photodetection and amplification of the OPC signal at the average power and center wavelength specified in Subsection 4.2.1. We know that the photodetected current is defined as:

$$I_{ph} = p_{cki,\alpha} r \tag{B.14}$$

where $r = 0.71$ A/W is the responsitivity of the PIN photodiode. The electrical power for harmonic 'i' measured at the ESA is equal to:

$$p_{eli,\alpha} = G_{amp} I_{rms}^2 Z = G_{amp} \frac{I_{ph}^2}{2} Z \tag{B.15}$$

where G_{amp} (33 dB) is the gain of the RF amplifier, I_{rms} is the root mean square value of the photodetected current and $Z = 50\ \Omega$ is the load resistance of the photodetector. Therefore, applying (B.14) to (B.15) and solving for the optical power $p_{cki,\alpha}$ we obtain:

$$p_{cki,\alpha} = \frac{1}{r} \sqrt{\frac{2 p_{eli,\alpha}}{G_{amp} Z}} \tag{B.16}$$

Table B.1 lists the parameter values of SOA-MZI small-signal model used for the CG calculation.

Table B.1: Parameter values for SOA-MZI small-signal model. Copyright © 2020, IEEE

Symbol	Parameter	Value	Unit
α_H	Linewidth enhancement factor	4	
τ_d	Differential carrier lifetime	26.5	ps
τ_{ASE}	Spontaneous carrier lifetime	70	ps
P_{sat}	SOA1 saturation power (Both architectures)	15	dBm
$\overline{G}_{1,s}$	SOA1 Gain (Switching)	24.8	dB
$\overline{G}_{1,m}$	SOA1 Gain (Modulation)	26.1	dB
$\overline{G}_{2,\alpha}$	SOA1 Gain (Both architectures)	28	dB

Continued on next page

Table B.1 – *Continued from previous page*

Symbol	Parameter	Value	Unit
$p_{el1,s}$	Electrical power at 10 GHz (Switching)	-8	dBm
$p_{el2,s}$	Electrical power at 20 GHz (Switching)	-9.5	dBm
$p_{el3,s}$	Electrical power at 30 GHz (Switching)	-10	dBm
$p_{el4,s}$	Electrical power at 40 GHz (Switching)	-11	dBm
$p_{el5,s}$	Electrical power at 50 GHz (Switching)	-12	dBm
$p_{el6,s}$	Electrical power at 60 GHz (Switching)	-13	dBm
$p_{el7,s}$	Electrical power at 70 GHz (Switching)	-14	dBm
$p_{el8,s}$	Electrical power at 80 GHz (Switching)	-15	dBm
$p_{el1,m}$	Electrical power at 10 GHz (Modulation)	-18	dBm
$p_{el2,m}$	Electrical power at 20 GHz (Modulation)	-21	dBm
$p_{el3,m}$	Electrical power at 30 GHz (Modulation)	-22.2	dBm
$p_{el4,m}$	Electrical power at 40 GHz (Modulation)	-24	dBm
$p_{el5,m}$	Electrical power at 50 GHz (Modulation)	-26.3	dBm
$p_{el6,m}$	Electrical power at 60 GHz (Modulation)	-28.66	dBm
$p_{el7,m}$	Electrical power at 70 GHz (Modulation)	-31	dBm
$p_{el8,m}$	Electrical power at 80 GHz (Modulation)	-33.3	dBm
$p_{ck1,s}$	OPC OMP power at 10 GHz (Switching)	-11	dBm
$p_{ck2,s}$	OPC OMP power at 20 GHz (Switching)	-11.75	dBm
$p_{ck3,s}$	OPC OMP power at 30 GHz (Switching)	-12	dBm
$p_{ck4,s}$	OPC OMP power at 40 GHz (Switching)	-12.5	dBm
$p_{ck5,s}$	OPC OMP power at 50 GHz (Switching)	-13	dBm
$p_{ck6,s}$	OPC OMP power at 60 GHz (Switching)	-13.5	dBm
$p_{ck7,s}$	OPC OMP power at 70 GHz (Switching)	-14	dBm
$p_{ck8,s}$	OPC OMP power at 80 GHz (Switching)	-14.5	dBm
$p_{ck1,m}$	OPC OMP power at 10 GHz (Modulation)	-16	dBm
$p_{ck2,m}$	OPC OMP power at 20 GHz (Modulation)	-17.5	dBm
$p_{ck3,m}$	OPC OMP power at 30 GHz (Modulation)	-18.1	dBm
$p_{ck4,m}$	OPC OMP power at 40 GHz (Modulation)	-19	dBm
$p_{ck5,m}$	OPC OMP power at 50 GHz (Modulation)	-20.2	dBm
$p_{ck6,m}$	OPC OMP power at 60 GHz (Modulation)	-21.3	dBm
$p_{ck7,m}$	OPC OMP power at 70 GHz (Modulation)	-22.5	dBm
$p_{ck8,m}$	OPC OMP power at 80 GHz (Modulation)	-23.7	dBm
η_s	Attenuation coefficient of $p_{cki,s}$	2	

Continued on next page

Table B.1 – *Continued from previous page*

Symbol	Parameter	Value	Unit
η_m	Attenuation coefficient of $p_{cki,m}$	4	
κ_s	Attenuation coefficient of $p_{dat,s}$	4	
κ_m	Attenuation coefficient of $p_{dat,m}$	2	

B.4 Optical Modulation Power

The Optical Modulation Power (OMP), mentioned in subsection 4.2.1, is the optical equivalent of the electrical power at 10 GHz at the SOA-MZI output port J. This OMP is derived similarly to the case of $p_{cki,\alpha}$ in section B.3 from the RF spectrum measured by an ESA after photodetection and amplification. Thus, following the same analysis, the OMP power at 10 GHz, P_{op}, is given by:

$$P_{op} = \frac{1}{r}\sqrt{\frac{2P_{el}}{G_{amp}Z}} \tag{B.17}$$

where P_{el} is the electrical power at 10 GHz measured by the ESA.

Appendix C

Equipment List

The equipment used for the measurements presented and discussed in this thesis is listed in the following Table together with the chapter(s) it refers to.

Table C.1: List of equipment used in measurements

Chapter	**Apparatus**	**Type**
All	Optical Pulse Clock (OPC)	Pritel UOC-E-05-20
All	SOA-MZI	CIP twin 2R Optical Regenerator
All	CW Laser Sources	Emcore TTX1194
All	Optical Signal Analyzer (OSA)	Agilent 86142B
All	Mach-Zehnder Modulator	iXblue MXAN-LN-40 with DR-AN-40-MO driver module
All	Photodiode	U2T XPDV3120R
All	Electronic Spectrum Analyzer (ESA)	Rohde& Schwarz FSEK 20
All	Radio Frequency Generator (RF1)	HP 83731B
All	Optical Bandpass Filter (OBPF)	Yenista XTM-50
All	Optical Attenuator (Att)	Anritsu MN9610B
All	Optical Attenuator (Att)	HP8156A
All	Optical Power Meter (PM)	Anritsu Optical Power Meter ML9001A
2	Vector Network Analyzer (VNA)	Anritsu MS4644B with O/E MN4665B
2, 4	Electric low noise Amplifier (AMP1)	Centelax UAOL65VM
3	DCA Oscilloscope	Keysight N1000A Digital Communication Analyzer
4	Radio Frequency Generator (RF1)	Anritsu 69167B
4	Electric Amplifier (AMP2)	SCD20.40.1R
4	Electric Frequency Mixer	Mini circuits ZX05-24MH+
4	Electric Frequency Mixer	Marki Microwave M9-0765
4	Electric AWG Filter	Agilent M8190A-806
4	Electric Filter	mini circuits SLP-1000+
4	Arbitrary Waveform Generator (AWG)	Agilent M8190A
4	Vector Signal Analyzer (VSA)	Keysight 89600A
4	Digital Signal Oscilloscope (DSO)	Agilent DSO-X 4154A
4	Optical Spectrum Analyzer (OSA)	APEX 2683A

References

[1] *Test Data & Operation Manual of Ultrafast Optical Clock, Model : UOC-E-05-20, Serial No: 1807-14-049*, Pritel, Naperville, IL, USA, 2014.

[2] C. Bohémond, T. Rampone, and A. Sharaiha, "Performances of a Photonic Microwave Mixer Based on Cross-Gain Modulation in a Semiconductor Optical Amplifier," *Journal of Lightwave Technology*, vol. 29, no. 16, pp. 2402–2409, Aug. 2011.

[3] C. Bohémond, "Mélangeur de signaux hyperfréquences basé sur la modulation croisée du gain d'un amplificateur optique à semi-conducteurs," Ph.D. dissertation, École Nationale d'Ingénieurs de Brest, Brest, France, Jan. 2010.

[4] H. Termos, "Study of up & down conversion technique by all-optical sampling based on SOA-MZI All-optical radiofrequency sampling mixer based on a Semiconductor Optical Amplifier Mach-Zehnder Interferometer using a standard and a differential configuration," Ph.D. dissertation, École Nationale d'Ingénieurs de Brest, Brest, France, Feb. 2017.

Τίτλος: Οπτική δειγματοληψία βασισμένη σε συμβολόμετρο Mach-Zehnder με οπτικούς ενισχυτές ημιαγωγού (SOA-MZI) για αναλογικές εφαρμογές.

Λέξεις Κλειδιά: Φωτονική δειγματοληψία, Συμβολόμετρο Mach-Zehnder με οπτικούς ενισχυτές ημιαγωγού (SOA-MZI), Φωτονική μικροκυμάτων (MWP), Τεχνική γραμμικοποίησης με μετεπεξεργασία.

Περίληψη: Η φωτονική δειγματοληψία είναι μια διαδικασία που χρησιμοποιείται σε διάφορα συστήματα τελευταίας τεχνολογίας, καθώς επιτρέπει έναν μοναδικό συνδυασμό πλεονεκτημάτων, όπως την χαμηλή διακύμανση χρονισμού, την μικρή εξασθένηση, το υψηλό εύρος ζώνης και την ανοσία σε ηλεκτρομαγνητικές παρεμβολές. Η παρούσα διατριβή στοχεύει στη διερεύνηση και την επίδειξη της σκοπιμότητας χρήσης του SOA-MZI, ενός αμιγώς φωτονικού δομοστοιχείου, ως φωτονικού δειγματολήπτη στη θέση άλλων ηλεκτροοπτικών λύσεων, παρακάμπτοντας την ανάγκη για πρόσθετες αργές και δαπανηρές ηλεκτροοπτικές μετατροπές. Οι αρχιτεκτονικές Switching και Modulation είναι δυνατές με τον φωτονικό δειγματολήπτη SOA-MZI. Το κύριο πλεονέκτημα της αρχιτεκτονικής Modulation είναι ότι επιτρέπει τη χρήση πολύ υψηλών ρυθμών δειγματοληψίας. Χρησιμοποιώντας την αρχιτεκτονική Modulation, μια μέθοδος γραμμικοποίησης με μετεπεξεργασία αναπτύσσεται και επικυρώνεται. Πειραματικά, παρατηρείται σημαντική βελτίωση της Ολικής Αρμονικής Παραμόρφωσης (THD) μεταξύ 7 dB και 23 dB για ημιτονοειδή σήματα προς δειγματοληψία με συχνότητες μεταξύ 0,25 GHz και 2 GHz. Ο φωτονικός δειγματολήπτης SOA-MZI, χρησιμοποιούμενος ως φωτονικός μίκτης συχνότητας, εξετάζεται θεωρητικά αναπτύσσοντας ένα μοντέλο ανάλυσης μικρού σήματος και επικυρώνεται πειραματικά για τις αρχιτεκτονικές Switching και Modulation για το μετρικό του Κέρδους Μετατροπής (CG). CG ίσο με 16 dB επιτυγχάνεται για τη μετατροπή από 1 GHz σε 9 GHz, ενώ CG ίσο με 9 dB για τη μετατροπή από 1 GHz σε 39 GHz. Ρυθμός δεδομένων έως και 1 Gbps επιτυγχάνεται για δεδομένα διαμορφωμένα με σύνθετες μεθόδους διαμόρφωσης που έχουν μετατραπεί σε υψηλότερες συχνότητες.

Titre : Échantillonnage optique à base d'un interféromètre de Mach-Zehnder à base d'amplificateurs optiques à semi-conducteurs (SOA-MZI) pour applications analogiques.

Mot clés : Échantillonnage optique, Amplificateur optique à semi-conducteurs - Interféromètre de Mach-Zehnder (SOA-MZI), Photonique micro-ondes (MWP), Technique de linéarisation par post-distorsion.

Résumé : L'échantillonnage optique est une fonction utilisée dans divers systèmes de pointe, car il permet une combinaison unique d'avantages tels que la faible gigue temporelle, les faibles pertes, une bande passante élevée et l'immunité aux interférences électromagnétiques (EMI). Cette thèse vise à étudier et à montrer la viabilité d'utiliser un SOA-MZI, un dispositif purement photonique, comme échantillonneur photonique au lieu d'autres solutions électro-optiques, en évitant les lentes et coûteuses conversions électro-optiques supplémentaires. Les architectures de commutation et de modulation sont possibles avec l'échantillonneur SOA-MZI. L'avantage majeur de l'architecture de modulation est qu'elle permet d'utiliser un taux d'échantillonnage très élevé. Utilisant l'architecture de modulation, une méthode de linéarisation par post-distorsion est formulée et validée. Expérimentalement, une amélioration significative de la distorsion harmonique totale (THD) entre 7 dB et 23 dB est observée pour des signaux sinusoïdaux à échantillonner à des fréquences entre 0,25 GHz et 2 GHz. L'échantillonneur SOA-MZI, utilisé comme convertisseur photonique de fréquence, est examiné théoriquement en développant un modèle d'analyse de petits signaux et validé expérimentalement à l'aide des architectures de commutation et de modulation, en termes de gain de conversion (CG). Un CG égal à 16 dB est obtenu pour la conversion de 1 GHz à 9 GHz, tandis qu'un CG égal à 9 dB pour la conversion de 1 GHz à 39 GHz. Un débit binaire jusqu'à 1 Gbps est atteint pour des données en formats de modulation complexes converties.

Title: Optical sampling based on Mach-Zehnder Interferometer with Semiconductor Optical Amplifiers (SOA-MZI) for analog applications.

Keywords: Optical Sampling, Semiconductor Optical Amplifier - Mach-Zender Interferometer (SOA-MZI), Microwave Photonics (MWP), Post-Distortion Linearization Technique.

Abstract: Photonic sampling is a process employed in various state-of-the-art systems, since it permits a unique combination of advantages such as the low temporal jitter, the low-loss, high bandwidth and immunity to electromagnetic interference (EMI). This thesis aims at investigating and showing the feasibility of using the SOA-MZI module, a purely photonic device, as a photonic sampler in place of other electro-optic solutions, circumventing the need for additional slow and costly electro-optic conversions. The Switching and Modulation architectures are possible with the SOA-MZI photonic sampler. The major advantage of the Modulation architecture is that it enables the use of very high sampling rates. Employing the Modulation architecture, a post-distortion linearization method is formulated and validated. Experimentally, significant Total Harmonic Distortion (THD) improvement between 7 dB and 23 dB is observed for sinusoidal signals to be sampled at frequencies between 0.25 GHz and 2 GHz. The SOA-MZI photonic sampler, employed as a photonic up-converter, is theoretically examined by developing a small-signal analysis model, and experimentally validated using Switching and Modulation architectures in terms of Conversion Gain (CG). A CG equal to 16 dB is achieved for the 1 GHz to 9 GHz conversion, while a CG equal to 9 dB for the 1 GHz to 39 GHz conversion. A bit rate up to 1 Gbps is reached for up-converted data of complex modulation formats.